

Next Generation Anodes for Lithium-Ion Batteries

II.B.1 Next Generation Anodes for Lithium-Ion Batteries: Research Facilities Support (ANL, LBNL, ORNL, SNL, NREL))

Jack Vaughey, Point-of-Contact

Dennis Dees

Argonne National Laboratory
9700 South Cass Avenue
Argonne, IL 60439
Phone: (630) 252-8885
E-mail: vaughey@anl.gov

Brian Cunningham, DOE-EERE-VTO Program Manager

Hybrid Electric Systems, Battery R&D

Phone: (202) 287-5686
E-mail: brian.cunningham@ee.doe.gov

Table of Contents

Project Introduction (page 2)

Objectives (page 4)

Approach (page 4)

1. Results: Active Silicon-based Materials
 - Baseline Silicon (ANL) (page 5)
 - Silicon Scale-Up (ANL) (page 9)
 - Silicon-Tin Composites (LBNL) (page 10)
 - Conclusions: Active Silicon-based Materials (page 12)
2. Results: Silicon-based Electrodes
 - Electrode Processing of Silicon Containing Anodes (ORNL) (page 13)
 - Electrode Characterization: Raman Spectroscopy (ORNL, ANL) (page 19)
 - Charged Silicon Electrode Reactivity (ANL) (page 23)
 - Silicon Electrode Electrochemistry (ANL) (page 28)
 - Conclusions: Silicon-based Electrodes (Page 33)
3. Results: Silicon Surface Modifications
 - Silane-based Surface Modifications – Synthesis (ANL) (page 34)
 - Silane-based Surface Modifications – Characterization (NREL) (page 39)
 - Silicon Oxide and Lithium Silicate based Surface Passivation (ANL) (page 44)
 - Conclusions Silicon Surface Modifications (page 47)
4. Results: Electrode Construction
 - Binder Development (LBNL, ANL) (page 48)
 - Lithium Inventory (ANL) (page 61)
 - Conclusions: Electrode Construction (page 66)
5. Key Publications (page 67)
6. References (page 68)

Project Introduction

Silicon has received significant attention as an alternative to graphitic carbon negative electrode in a lithium-ion battery due to its high capacity and availability [1]. Compared to graphitic carbons, elemental silicon has nearly an order of magnitude higher capacity (~3600 mAh/g Silicon vs 372 mAh/g Graphite), however, several problems have been identified that limit its utility including a large crystallographic expansion (~320%) upon lithiation, slow lithium diffusion, and high reactivity at high states of charge. Together these physical properties can result in particle cracking, particle isolation, electrolyte reactivity, and electrode delamination issues. These chemical reactivity and volume changes are manifested in SEI stability and cycling efficiency issues for the cell. The large number of studies focused on silicon based electrodes is a testament to the opportunity it presents but also the size of the challenge and innovation it inspires on multiple fronts.

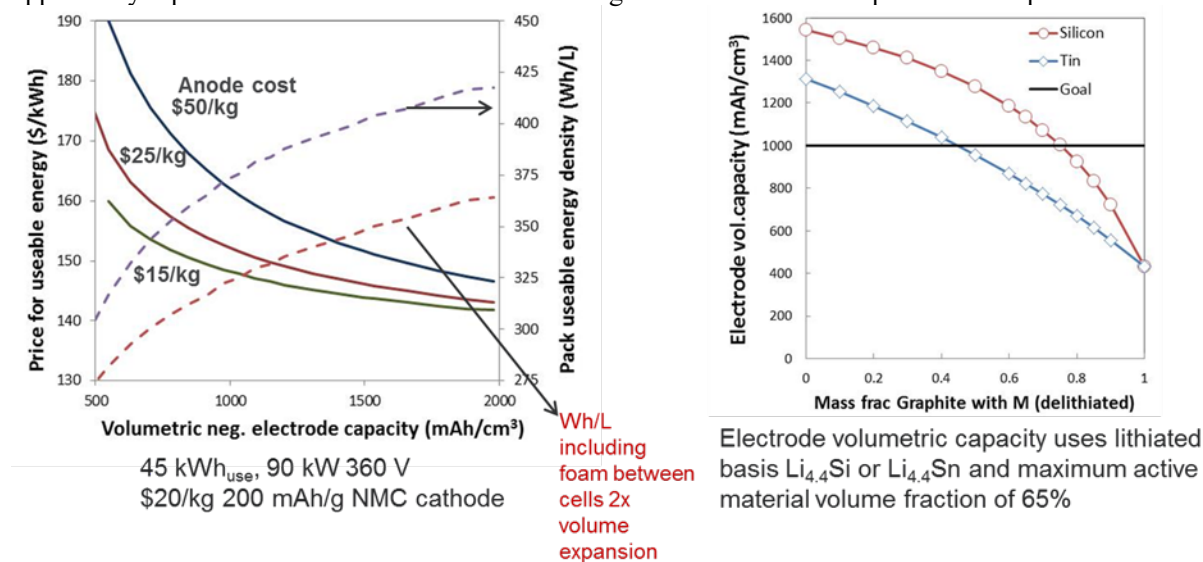


Figure 1. Battery Performance and Cost (BatPaC) model utilized to establish relevance by connecting pack to anode targets.

BatPaC [2], a techno-economic program designed to model lithium-ion battery performance and cost, was utilized to establish program relevance by connecting DOE/USABC pack performance targets to anode targets. To set goals for the program, BatPac was used to (see Figure 1, left frame), show that anode volumetric capacities greater than 1000 mAh/cm³ generally minimizes battery cost when coupled to an advanced NMC cathode. Note that higher capacities result in diminishing savings in cost. The analysis (right frame) also predicts that silicon-graphite electrodes with less than 75 wt% graphite can achieve the 1000 mAh/cm³ target.

Next Generation Anodes for Lithium-Ion Batteries, also referred to as the Silicon Deep Dive Program, is a consortium of five National Laboratories assembled to tackle the barriers associated with development of an advanced lithium-ion negative electrode based upon silicon as the active material. This research program has several goals including baselining promising silicon materials that can be either developed by a team member or obtained in quantities sufficient for electrode preparation by the consortiums facilities, developing a composite Si-Gr electrode that meets BatPac specifications, and executing full cell development strategies that leverage DOE-EERE-VTO investments in electrode materials and characterization. The primary objective of this program is to understand and eliminate the barriers to implementation of a silicon based anode in a lithium-ion cell. The five National Laboratories involved are focused on a single program with continuous interaction, clear protocols for analysis, and targets for developing both an understanding and a cell chemistry associated with advance negative electrodes for lithium-ion cells. This undertaking is a full electrode/full cell chemistry project leveraging baseline electrodes prepared at the consortium facilities. All efforts are directed to understanding and developing the chemistry needed for advancing silicon-based anodes operating in full cells. Materials development efforts include active material development, binder synthesis, coatings, safety, and

electrolyte additives. Efforts include diagnostic research from all partners, which span a wide range of electrochemical, chemical and structural characterization of the system across length- and time-scales. Specialized characterization techniques developed with DOE-EERE-VTO funding, include neutrons, MAS-NMR, optical, and X-ray techniques being employed to understand operation and failure mechanisms in silicon-based anodes. In addition, several strategies to mitigate lithium loss are being assessed. The project is managed as a single team effort spanning the Labs, with consensus decisions driving research directions and toward development of high-energy density lithium-ion batteries. A detailed list of participants is given in Figure 2.



Figure 2. Program participants including Laboratories, research facilities, and individual contributors.

Objectives

- Understand and overcome the science and technology barriers to the use of silicon-based anodes in high-energy density lithium-ion batteries for transportation applications.
 - Stabilize the SEI
 - Stabilize the electrode
- Demonstrate functional prototype lithium-ion cell chemistries which meet the DOE/USABC performance targets.

Approach

Sandia National Laboratories (SNL), Oak Ridge National Laboratory (ORNL), National Renewable Energy Laboratory (NREL), Lawrence Berkeley National Laboratory (LBNL), and Argonne National Laboratory (ANL) have teamed together to form an integrated program dedicated to identifying, developing an understanding, and proposing solutions to the problems associated with the commercialization of silicon as an

active component of a lithium-ion electrochemical cell. Technical targets have been developed and regular communications have been established across the team. Throughout the program, there is a planned focus on understanding, insights into, and advancement of silicon-based materials, electrodes, and cells. All anode advancements will be verified based on life and performance of full cells. Toward that end, baseline silicon-based materials, electrodes, and cells have been adopted, along with uniform full cell testing protocols.

In examining improvements, changes to the baseline cell technology will be minimal but will be updated to reflect advances, new suppliers, and treatments. Studies of the present baseline systems have adopted a testing protocol from the literature [3] that has worked well for lithium-ion cells with silicon containing anodes. The test starts with three slow (C/20) formation cycles, an HPPC cycle, and then the C/3 aging cycles. The test ends with another HPPC cycle and three more slow (C/20) cycles. All constant current cycling is symmetric between charge and discharge rates. The tests are run at 30°C. If there is little or no aging in the first 100 cycles, the protocol can be repeated. This protocol effectively examines capacity, impedance, and aging effects in about a month's worth of testing. The present baseline silicon was developed and produced by Paraclete Energy (Chelsea, MI) and has been made available to all participants. The cathode is a commercial 532 NMC Cathode available from CAMP, and the electrolyte is 1.2M LiPF₆ in a 3:7 ratio of EC/EMC by weight (Gen2) plus 10 wt% FEC. Scale-up of materials, incorporation of materials advancements into electrodes, prototype cells, characterization, safety evaluation, abuse tolerance and testing of cells, are part of a wide range of integrated studies supported by battery research facilities at the National Labs working closely with the program. These research facilities include the Battery Abuse Testing Laboratory (BATLab), the Battery Manufacturing Facility (BMF), the Cell Analysis, Modeling, and Prototyping (CAMP), the Materials Engineering Research Facility (MERF), and the Post-Test Facility (PTF).

The fundamental understanding of silicon-based electrode active materials is based on extensive electrochemical and analytical diagnostic studies on components, electrodes, and cells conducted within the program. This effort contains in-situ and ex-situ studies on full and specialty cells, including reference electrode cells. Overall, the diagnostic studies are intended to help establish structure-composition-property relationships, including lithium-rich surface compounds, bulk transport, and kinetic phenomena. Together they form the basis for accurately assessing component and electrode failure modes and sets a path for advancements. Supported by the diagnostic studies, materials development on silicon-based materials, electrodes, and cells has been focused on enhancement of interfacial stability, accommodation of volume changes on lithiation, improvements in overall performance and life. A key avenue of research for this goal is the development and testing of surface coatings and electrolyte additives designed to modify and stabilize the dynamic silicon-electrolyte interface. In addition, functional polymer binders designed to accommodate volume changes, increase conductivity, and improve adherence are being developed and analyzed. Finally, the program is exploring active material development including silicon composites, compounds, and the advantages of adding additional lithium inventory into the cell are being developed.

Communication of programmatic progress to battery community is critical. This will generally be accomplished through publications, presentations, reports, and reviews. Further, the program is open to industrial participation and/or collaboration that does not limit program innovation or the free flow of information. Finally, this program is highly integrated with the SEISta program, a sister program focused on stabilization of the silicon SEI layer. Generally, SEISta is focused on the development and characterization of model systems, surface analysis, well-defined active area thin film electrodes, lithium transport, and interfacial silicate phases and phenomena.

1. Results: Active Silicon-based Materials

Baseline Silicon

In 2017 U.S. silicon supplier, Paraclete Energy (PE), provided multiple samples to the CAMP Facility for evaluation as a prospective baseline material. The powders were found to have an average particle size of 150

nm and are described as a Si core with a thin SiO₂ shell (termed “SiO_x”). The particle size analysis (MERF) and SEM images (ANL) demonstrated Paraclete’s control of particle size (Table-1). Electrochemical performance evaluations of the 100g “initial sample” showed performance consistent with previous silicon powders. A scaled-up 500 gram (“initial scale-up”) sample of the original was received and the amount of silica was assessed using MAS- NMR (ANL). The MAS-NMR results of the “initial scale-up” sample showed measurable organic carbon, remnants of the companies scale-up processing method. After evaluation and data assessment multiple samples (labeled *Samples A, B, C, and D*) were procured. Based on the observations from the previous batches, these *Sample A, B, C, D* samples were processed by Paraclete Energy with slight

Table-1: (Left) Experimental silicon samples from Paraclete Energy with particle size and SEM image information. (Right) Brief sample descriptions.

Sample	Description	D50 (um)	SEM Images of powder at various level of magnification	ID	Description
K16-013-MC	Initial 100g	0.96		Initial sample	Initial Scoping Sample
C17-301-LS	“Initial Scale up”	0.12		Initial Scale-up	Scale-up of initial sample
C17-001-LS	Sample A	0.1		Sample A	Scale-up of initial sample with improved drying
C17-016-LS	Sample B	0.09		Sample B	Different silicon feed stock with improved drying
C17-022-LS	Sample C	0.1		Sample C	Initial sample silicon feed stock manufactured using alternative method
C17-021-LS	Sample D	0.11		Sample D	Initial sample silicon feed stock, but oxidized in a different manner

processing variations and analyzed by Argonne. After electrochemical testing *Paraclete D* was selected for additional scale-up and the new baseline was made available for the Silicon Deep Dive effort to replace older NanoAmor (70-130 nm), Paraclete *initial scale-up* (500g), Alfa-Aesar “50nm nanoscale silicon”, and HydroQuebec SiO_x materials. Multiple electrodes based on *Paraclete D* were fabricated using the aqueous slurry processing and coating strategies standardized by the CAMP Facility. The 15 wt.% silicon / 85% graphite electrodes were fabricated using the powders found in Table 1 at the ~2 mAh/cm² to match to the Electrode Library that the CAMP Facility maintains. The electrodes were made available to the team for evaluation and research.

Table-2: Half-cell coin-cell formation testing results of experimental silicon samples from Paraclete Energy. The capacity values are normalized to the total weight of the silicon, graphite, and carbon black present in the electrode.

Half Cell Performance Summary

Sample	1 st Cycle Discharge Capacity (mAh/g)	Irreversible Loss (mAh/g)	Reversible Cycle Charge Capacity (mAh/g)	1 st Cycle Efficiency (%)
Original Sample	831	151	679	92.4
Sample A	750	61	684	90.6
Sample B	618	108	592	88.3
Sample C	743	87	656	89.3
Sample D	747	93	653	90.9

Voltage Window: 0.05 – 1.5 (V)

Half-cell coin-cell data of 15 wt.% silicon / 85% graphite experimental electrodes are shown in Table-2. The formation data shows the 1st discharge (lithiation) capacity, irreversible capacity loss, reversible charge (delithiation) capacity at a C/10 rate, and 1st cycle coulombic efficiency. Silicon-containing electrodes generally have lower cycling coulombic efficiencies throughout cycling compared to graphite-only electrodes, so determining a true reversible cycle capacity can be arbitrary. All of the testing was performed using 4 coin cells (CR2032) for each electrode using electrolyte with the composition 90 wt.% (1.2 M LiPF₆ in EC:EMC 3:7 by wt. %) + 10 wt.% (FEC) using the cycling window of 0.05 to 1.5 V vs. Li metal. The results suggest comparable initial capacities between the samples.

Full-cell coin-cells were then fabricated using the various ~2 mAh/cm² (0.05 to 1.5 V vs. Li metal) silicon-containing (PE) electrodes versus a standard 90 wt.% NMC532, 5 wt.% Timcal C45 carbon black, and 5 wt.% PVDF made for the Electrode Library at the CAMP Facility [A-C013A]. The approximate n:p capacity ratios for the electrode couples are between 1.1 and 1.3 for a voltage window of 3.0 to 4.1 V in a full cell.

The Silicon Deep Dive cycling protocol was used to evaluate these materials and for comparison purposes. Figure 3 shows the resulting full cell testing on the Paraclete Energy silicon samples. *Samples A and D* showed the best performance of the 4 samples provided by PE and are similar to the previous baseline electrode performance (50-70 nm Si NanoAmor, [A-A006A]). Sample D performed slightly better than *Sample A* in the final 3 cycles, thus “*Sample D*” was selected to be scaled-up to a 500 g sample “*Scale-up of Sample D*” for purposes of becoming the new silicon material for the future baseline electrodes. Early indications from initial coatings show improved coating quality and integrity with the “*Scale-up Sample D*” for both low and high (>3.0 mAh/cm²) coating loadings after calendaring. Henceforth, in this section the “*Scale-up Sample D*” powder was used as the silicon components of the electrodes fabricated.

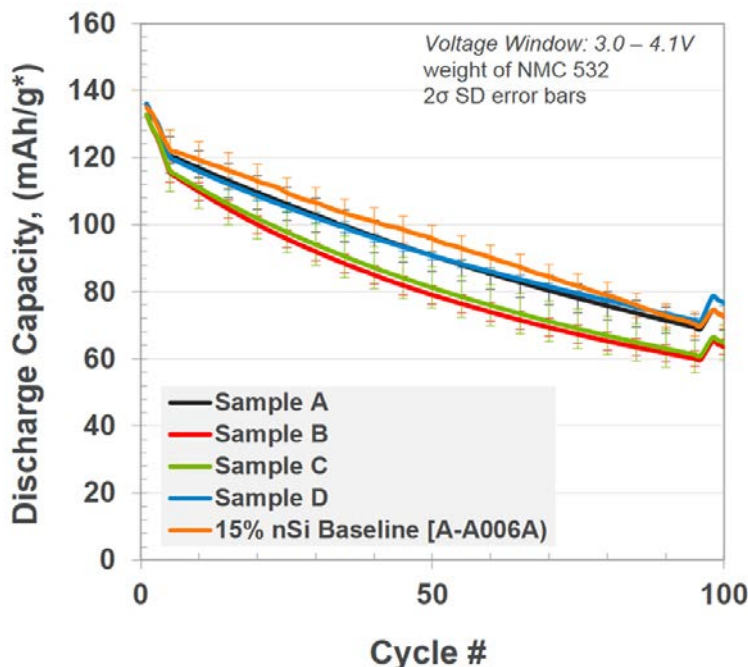


Figure 3. Full-cell coin-cell results showing average discharge capacity vs. cycle number. The Silicon Deep Dive full cell cycling protocol was used for evaluating the experimental silicon electrodes compared to the original silicon-containing baseline electrode [A-A006A]. The cycling protocol consists of three slow (C/20) formation cycles, an HPPC cycle, and then C/3 aging cycles, followed by a 2nd HPPC cycle, and finally three more slow (C/20) cycles. The capacity values are normalized to the weight of NMC532.

Table-3: CAMP Silicon Deep Dive silicon-containing electrodes utilizing Paraclete Energy silicon powder. (Left) baseline electrode A-A012 and (Right) baseline electrode A-A013 fabricated at slightly different coating loadings. The powder was provided in a scaled-up process matching the Sample D processing.

Anode: A-A012	Anode: A-A013
73 wt.% Hitachi MagE3 graphite	73 wt.% Hitachi MagE3 graphite
15 wt.% Paraclete Energy Silicon	15 wt.% Paraclete Energy Silicon
2 wt.% Timcal C45 carbon	2 wt.% Timcal C45 carbon
10 wt.% LiPAA (H ₂ O), LiOH titrated	10 wt.% LiPAA (H ₂ O), LiOH titrated
<i>Paraclete Prod: nSiO [F17 005 LS] "Scale-up Sample D",</i>	<i>Paraclete Prod: nSiO [F17 005 LS] "Scale-up Sample D",</i>
<i>"SS" = single sided, target is for Electrode Library -></i>	<i>"SS" = single sided, target is for Electrode Library -></i>
<i>Electrode ID: LN3107-86-6</i>	<i>Electrode ID: LN3107-92-3</i>
Cu Foil: 10 microns	Cu Foil: 10 microns
Total Electrode Thickness: 42 μm (SS)	Total Electrode Thickness: 37 μm (SS)
Coating Thickness: 32 μm (SS)	Coating Thickness: 27 μm (SS)
Porosity: 44.4 %	Porosity: 45.6 %
Total SS Coating Loading: 3.63 mg/cm ²	Total SS Coating Loading: 3.00 mg/cm ²
Total SS Coating Density: 1.13 g/cm ³	Total SS Coating Density: 1.11 g/cm ³

The initial baseline electrodes [A-A012] (Table-3) using the new silicon source (PE) for this project was coated with an expected mAh/cm² of ~2 in half-cell testing (Table-4). The 2nd baseline electrode [A-A013] with the same materials and composition but at a 16% lower loading and was made to lower the n:p ratio closer to 1.1 (Table-3). Full cells were then made using these baseline materials paired against the same

Table-4: Half-cell coin cell formation testing results of new baseline 15wt.% silicon-containing electrodes. The silicon powders used are “Sample D” and “Scaled-up Sample D” from Paraclete Energy. The capacity values are normalized to the total weight of the silicon, graphite, and carbon black present in the electrode.

Half Cell Performance Summary

Sample	Total Coating Loading (mg/cm ²)	1 st Cycle Discharge Capacity (mAh/g)	1 st Cycle Efficiency (%)	Reversible Cycle Charge Capacity (mAh/g)	Reversible Cycle Charge Areal Capacity (mAh/cm ²)
Sample D	3.88	747	90.9	653	2.39
A-A012	3.63	803	91.0	723	2.56
A-A013	3.00	842	89.3	716	2.07

Voltage Window: 0.05– 1.5 (V), 30°C

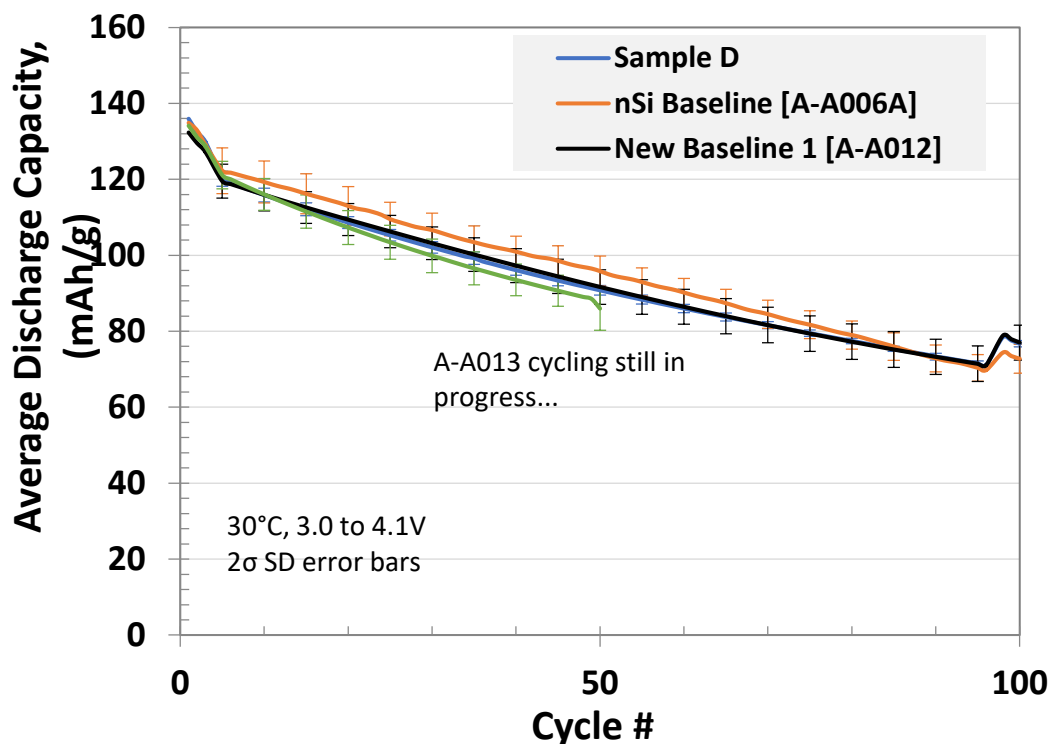


Figure 4. Full-cell coin-cell results showing average discharge capacity vs. cycle number for the Silicon Deep Dive baseline electrodes vs. NMC532 [A-C013A]. Data shows the average values based on 4 coin cells for each electrode pair. The capacity values are normalized to the weight of NMC532.

cathode [A-C013A] using the Silicon Deep Dive Protocol to evaluate the cycling performance. Figure 4 shows the full cell cycling performance comparison of the original baseline material [A-A006A], *Sample D*, and the baseline electrodes [A-A012] and [A-A013] being tested under the Silicon Deep Dive full cell cycling protocol. The protocol reveals that similarities of the performance for the 4 electrodes suggesting that the “*Scale-up Sample D*” powder is adequate to replace the previous baseline electrode and the two n:p ratios chosen retain a similar capacity retention (Figure 4).

Silicon Scale-up

In addition to the commercial Paraclete silicon samples we obtained, there is programmatic interest in securing an internal supplier for evaluation, testing, and modification that is controlled by the Laboratories. One alternative is development of an advanced bench-scale hydrothermal or solvothermal-based synthesis system to produce engineered silicon nanoparticles and composites. This method needs to be validated and materials characterized for surface passivation, purity, and scalability. The synthetic capability to be developed would be based on the design and construction of a turnkey hydrothermal or solvothermal-based synthesis reactor system capable of batch production of 10 to 50 g of nanoparticles per run.

Initial development centered on design and installation of a four liter hydrothermal or solvothermal-based system. Seen in Figure 5 (a), the high-temperature, high-pressure system was installed with significant safety devices in a walk-in hood. System stability and performance of the installed equipment were confirmed by adding 15 grams of NanoAmor Si particles (CAMP - Lot # 0142-071510, 130 nm) were injected into the reactor using water as a solvent, and heating to anticipated temperatures and pressures. The reaction mixture was allowed to stand for 1 hour at a reaction temperature of 392 °C, a reaction pressure of 3500 psi and a stirring speed of 500 rpm. After cooling, the water and hydrothermally treated 15 grams of NanoAmor Si particles were evaluated and characterized.

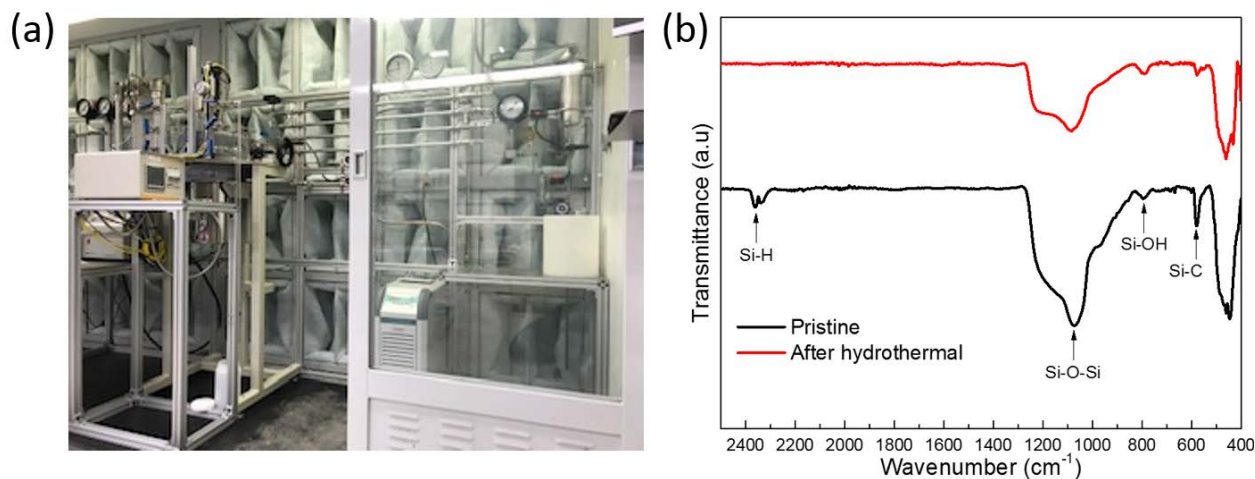


Figure 5. Installed 4 L hydro/solvothermal reaction system (a) and FT-IR result comparison of pristine NanoAmor Si particles and their hydrothermally treated product

FTIR analysis of the Si particles before and after exposure to the high temperature high pressure water process showed little change in the Si-C (600 cm^{-1}) and Si-H (2350 cm^{-1}) peaks. Previous MAS-NMR studies had shown that while these NanoAmor samples are approximately 50% SiO_2 by weight, due to their small size and high surface area, the silica surface appears stable to the treatment.

Additional reaction studies, new solvents, alternative precursors, and detailed analysis of product stream are underway. This test has confirmed stable operation of the installed four liter hydrothermal or solvothermal-based synthesis system, stability of a passivated version of our desired product

Silicon-Tin Composites

The Dahn group (Dalhousie University, Halifax, NS) has identified amorphous Si-Sn films with Sn content lower than 40 mol% as a series of compositions that show acceptable reversible capacities while demonstrating low irreversible capacity. For example the composition $\text{Si}_{0.64}\text{Sn}_{0.36}$ was shown to demonstrate a capacity of ~ 1900 mAh/g with a low irreversible capacity of ~ 100 mAh/g during the 1st cycle.[3] Ahn *et al.* later confirmed amorphous Si-Sn nanocomposite electrodes produced by magnetron co-sputtering method also demonstrated improved cycling when compared to an amorphous Si film at a similar thickness.[4] In general the advantage of the Si-Sn composite anode system arise from combining the large gravimetric capacity of Si with the excellent electrical conductivity and good ductility of Sn. [5-6] Experiments to understand the lithiation / delithiation process and interplay between the two lithiated species in more detail have been initiated driven by the nanoscale interactions between the immiscible crystalline Si and Sn metals. Initial efforts have focused on thin film studies to assess non-homogeneous phases, stability, and electrochemical performance before developing a splat quenching method to produce bulk phases.

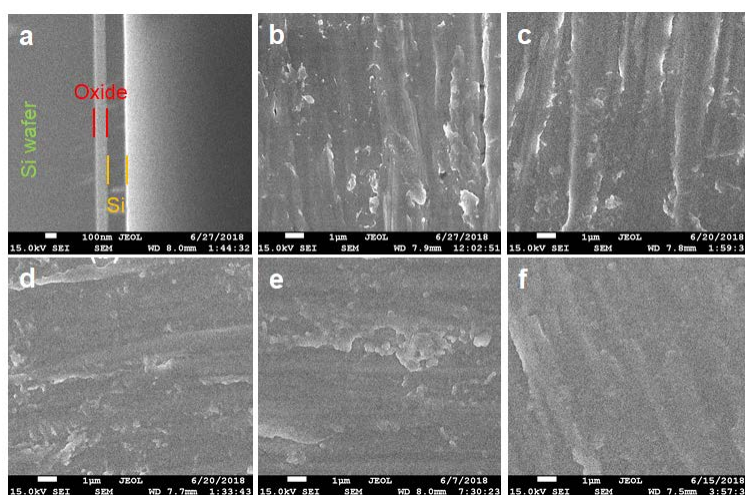


Figure 6. (a) Cross sectional SEM image of Si wafer with 100 nm surface oxide after Si deposition for 20 min, SEM image of (b) Cu foil substrate, (c) Si-5, (d) Si-10, (e) Si-20, and (f) Si-30 films.

Before the synthesis of Si-Sn thin films, we first optimized Si thin film deposition by a DC magnetron sputtering method. Physical and electrochemical properties of the as-produced Si films were investigated using X-ray diffraction (XRD), scanning electron microscopy (SEM), energy-dispersive X-ray spectroscopy (EDS), and electrochemical methods to identify the optimal synthesis condition. Coin cells were assembled directly using the as-produced Si films deposited on Cu foils (1.6 cm^2) as the working electrodes, Li metal foil as the counter electrode, and 1 M LiPF_6 in ethylene carbonate (EC)-diethyl carbonate (DEC) (50: 50 wt%) as the electrolyte without the use of fluoroethylene carbonate (FEC) additive. The cells were cycled between 1.5 and 0.01 V at C/20 based on the experimental capacity. Cyclic voltammetry (CV) was carried out between 2 and 0.01 V at a scan rate of 0.1 mV/s.

Figure 6a shows the cross sectional SEM image of the Si wafer after 20 min Si deposition. A layer of 100 nm oxide is present on the Si wafer before deposition (**Figure 6a**), meanwhile, a layer of Si appears on the top of the oxide layer after the deposition. The thickness of the deposited Si is ~ 160 nm. Varied deposition times yielded controllable sample thicknesses in the range 40 - 240 nm, respectively. SEM images of the Si thin films

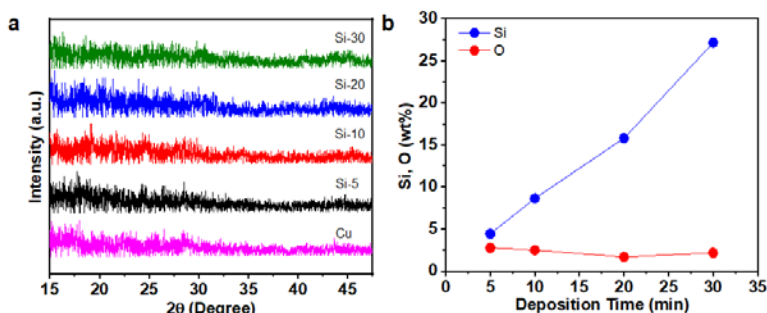


Figure 7. (a) XRD patterns of Si films along with Cu foil reference, and (b) content of Si and O detected by EDS for Si films.

(**Figure 6c-f**) display similar morphological features. It is believed that the surface roughness originates from the underlying Cu foil (**Figure 6b**). As shown in **Figure 7**, all the Si films appear amorphous to powder X-ray diffraction and have approximately the same O content. Investigations on the source of oxygen are inconclusive but probably include surface silica or copper oxide on the copper foil.

Figure 8 presents the CV curves of the as-produced Si films during the first two cycles. The small cathodic peaks at $\sim 0.7 - 0.8$ V are attributed to electrolyte decomposition and/or SEI formation during the 1st

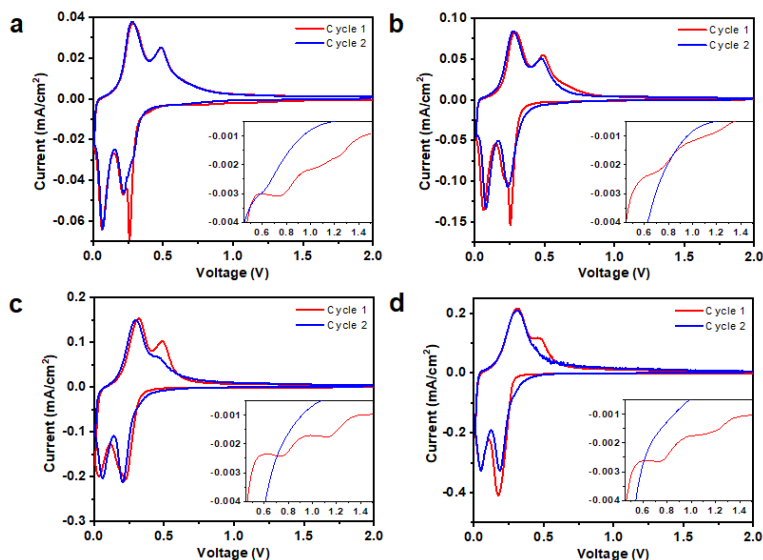


Figure 8. CV curves of (a) Si-5, (b) Si-10, (c) Si-20, and (d) Si-30 films during the first two cycles. Insets are enlarged CV curves between 0.45 and 1.5 V

cycle (insets in **Figure 8a-d**). All the films demonstrate typical lithiation of amorphous Si (a-Si), leading to the formation of amorphous Li_xSi (a- Li_xSi) at $\sim 0.2 - 0.3$ V, whereas all anodic curves show two broad peaks at ~ 0.3 and 0.5 V, corresponding to the extraction of Li from a- Li_xSi .

Based on the deposition method used to produce Si thin films, Si-Sn thin films were deposited on Cu foil. **Figure 9** shows the electrochemical performance of the as-produced Si-Sn film. From the cross-sectional SEM image, the thickness of Si-Sn film is ~ 140 nm. The voltage profiles and CV curves (**Figure 9a, b**) exhibit similar amorphous features to Si films, with an improved initial CE of $\sim 87\%$, compared to 82% for the earlier Si films. A close comparison of the CV curves for the 140 nm Si-Sn vs. 160 nm Si film reveals small differences near the SEI formation region around 0.75 V, perhaps implying the possible difference in the passivating behavior between Si and Sn. Overall the Si-Sn film exhibits much better cycling stability than the Si films of similar thickness with no obvious difference in CE, consistent with the earlier reports of Ahn, et al. These results

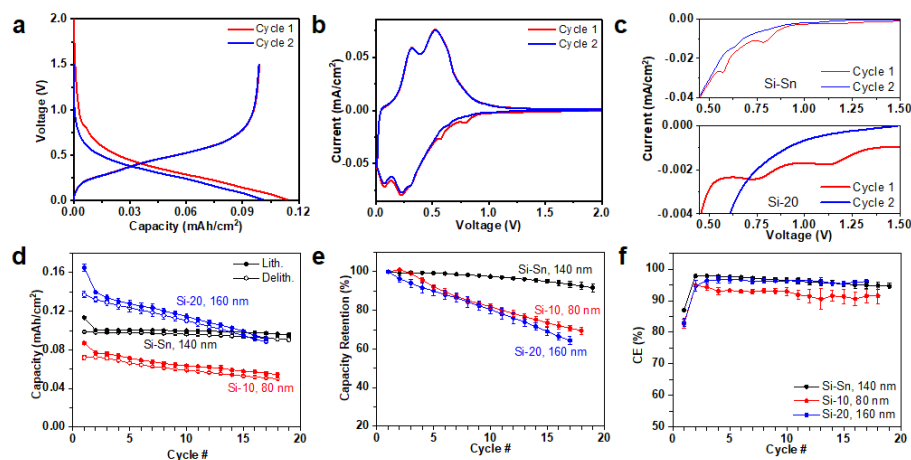


Figure 9. (a) Voltage profiles, (b) CV curves of Si-Sn film,, (c) enlarged CV curves at 0.14 -1.5 V, (d) capacity, (e) capacity retention, and (f) CE of Si-Sn and Si films of similar thickness.

highlight that the incorporation of tin (and lithiated tin) into the matrix improves the electrochemical performance of the active Si species. Further scale-up studies and studies to discern the role the interactions between the lithiated phases has on the increased stability are underway.

Conclusions - Active Silicon-based Materials

We developed a new baseline silicon electrode system using U.S. silicon supplier, Paraclete Energy, as a materials source. Paraclete provided multiple samples, including scale-up versions of the needed materials, for evaluation and screening. Paraclete Energy has demonstrated their ability to control particle size and customize processing steps to target surface chemistries. Electrochemical data is comparable to our best electrode performance and more importantly the silicon source provides a dependable and repeatable silicon powder from batch to batch.

A 4L hydrothermal / solvothermal-based synthesis system was installed and a preliminary performance evaluation of the reactor was successfully performed at 3500 psi, 392 °C, and 500 rpm. During the testing process, pristine NanoAmor SiO_x particles were hydrothermally treated. The system was able to maintain specifications while no obvious decomposition or modification of the silicon / silica surface was noted.

Silicon and silicon-tin composite films with the thickness ranging from a few tens to a few hundred nanometers were prepared by direct deposition on Cu foils. The DC sputtering method used generated films with low O content and stable cycling performance during early cycles. Silicon-tin composite films were prepared by extrapolation from Si film study. The as-produced Si-Sn exhibits improved 1st cycle CE and cycling stability, compared to similar silicon films. Future work will be focused on using splat cooling to scale up the materials

2. Results: Silicon-based Electrodes

Electrode Processing of Silicon Containing Anodes

Whereas as traditional graphite anodes are formulated in an *N*-methyl-2-pyrrolidone (NMP) based slurry with carbon black and polyvinylidene fluoride binder on Cu foil [7], industry has been moving towards using water based slurries to lower costs [8-9]. The dispersion of Si in water based graphite slurries has been assumed to fall directly from the graphitic carbon system, however most of the work in the literature was focused on small batches of materials whereas working at larger scale often introduces new challenges. Indeed, recent studies have observed H₂ gas formation during larger scale preparation (> 1 L) in water based Si slurries [10-11] with proposed deeper oxidation of the Si particles being the source of the gas,[10-11] producing a thick oxide layer that can decrease the materials theoretical capacity and cause additional first Coulombic losses.

This gassing during electrode processing likely goes unnoticed when working at laboratory scale but becomes problematic in a manufacturing setting. The occurrence of H₂ poses safety concerns, as current production methods involve mixing slurries in large sealed planetary mixers, allowing for pressurization of this flammable gas. Furthermore, slurries are not necessarily coated immediately after they are mixed. This allows for continued oxidation of the Si during slurry storage, which will lead to loss of material capacity as well as changes in weight loadings. The conversion of a 5 nm thick shell of Si to SiO₂, on a 110 nm Si particle, lends to a ~25% capacity decrease. Understanding these reactions and their impact on the properties of the silicon electrodes will lead to better and more consistent electrodes if water –based processing is to become the standard for silicon electrodes

Figure 10 demonstrates the negative impact of gassing on the storage of Si/graphite aqueous based slurry. Open storage, to prevent pressurization of the gassing slurry, resulted in ejection of the slurry over a 1-week period. These observations motivated this research to understand specifically what components of the slurry



Figure 10. 1 L of 15% Si-graphite aqueous based slurry after 1-week storage. Gassing from the slurry caused foaming and subsequent drying as the slurry “snaked” out of the open container.

sample	Si	CB	binder	solvent	Δ P	Δ P
--------	----	----	--------	---------	-----	-----

id	particle				100 h (atm)	20 h (atm)
N1	NA 70-130 ^b	Yes	No	NMP	-0.03	-0.01
W1	NA 70-130	No	No	water	-0.01	0
W2	NA 70-130	Yes	No	water	0.22	0.04
W3	NA 70-130	No	Yes	water	-0.01	-0.01
W4	NA 70-130	Yes	Yes	water	0.47	0
W5	AA 325 ^c	No	No	water	1.27	0.16

Table 5: Summary of Slurry Samples and Selected Results

aBased Scherrer analysis of Si (111) reflection (Fig. S3); bNA 70-130 = NanoAmor 70 – 130 nm; cAA 325 = Alfa Aesar 325 mesh.

manufacturing lead to gassing and how it could be minimized. To emulate high energy mixing needed for dispersing Si, the slurries were mixed on a roller mill with the zirconia media, in a custom pressure vessel, allowing in-situ pressure monitoring and post-processing gas analysis by mass spectroscopy. Because Si tends to easily agglomerate, high energy mixing methods, such as planetary ball milling, are often used to better disperse the Si amongst carbon additives and binder. This technique does not match the energy of planetary ball milling, likely leading to lower overall gassing reactions. A summary of the prepared slurries and selected results can be found in Table 5. Samples are identified utilizing designations given in this table. Conditions were selected to represent various mixing conditions and solvents.

Figure 11A displays the pressure change in the mixing vessel of various Si slurries up to 100 hours mixing time. This data shows the change in cell pressure with time as the reaction occurs. W5 caused the greatest pressure

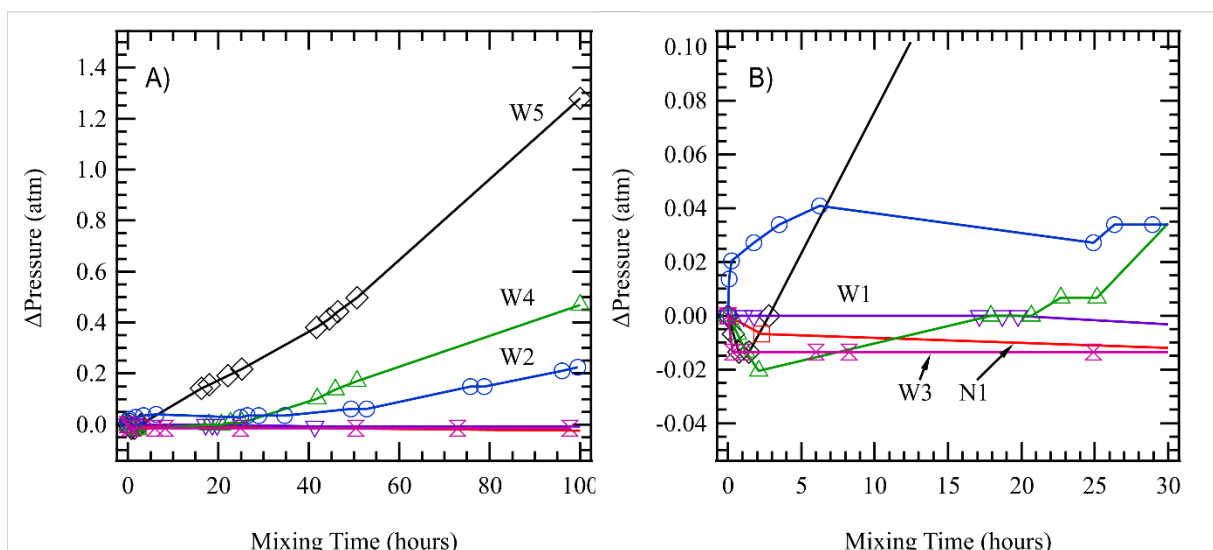


Figure 11A) The change in pressure vs time of W2 – water based nano Si/CB slurry (blue trace, circles), W5 – water based 325 mesh Si slurry (black trace, diamonds), W4 – water based Nano Si/CB/LiPAA slurry (green trace, triangles), W3 – water based nano Si/LiPAA slurry (fuchsia trace, hour glasses), W1 – water based Nano Si slurry (purple trace, upside-down triangles), and N1 – NMP based Nano Si/CB slurry (red trace, squares). B) Zoomed in plot of the first 30 hours of Fig. 2A

increase of ~1.27 atm, followed by the W4 and W2 at ~0.47 atm and ~0.22 atm, respectively. W1, W3, and N1 caused the pressure to decrease by 0.01, 0.01, and 0.03 atm, respectively. A closer examination of the first 30 hours of mixing, (Fig. 2B), shows that the W4 and W5 also caused a pressure decrease in the vessel before increasing to the above-mentioned pressures, indicating a competing reaction that absorbs gas(es). Unlike the other mixtures, W2 caused a pressure increase in the initial mixing time, with a slight pressure decrease of 0.01atm after 20 hours. In a separate experiment, even after the mixing was halted on a nano Si/CB water based slurry, pressure continued rising at a rate of 0.012 atm day⁻¹. This observation is important, as this reveals that the reaction does not stop when mixing is ceased.

The gases from the vessels were analyzed by mass spectroscopy to determine the cause of the pressure changes. Figure 12A shows the mass spectra collected from W2, W4, and N1. These were all normalized to the N₂ peak intensity of ambient air inside the vessel (the N₂ peak exceeds the y axis of Figure 12A). The gas collected from W2 and W4 show large spikes at 2 AMU, due to H₂ production (Fig 12B). No additional H₂ was present in the vessel of NMP based slurry, indicating the H₂ must come from H₂O, according to eq. 1:

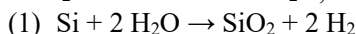
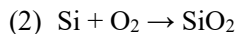


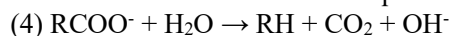
Figure 3C focuses on the O₂ signal at 32 AMU. Both the water based and NMP bases slurries resulted in a decrease in the O₂ concentration by 2% and 7%, respectively, relative to ambient air. Since this O₂ consumption occurs independent of solvent choice, it is must come from residual air inside vessel, according to eq. 2:



This finding is emphasized by the fact that the O₂ consumption aligns with the pressure decrease of the N1 and W4 (Fig. 11B). The same immediate pressure drop was not observed for sample W2, but the rapid H₂ production may have outweighed the O₂ consumption, resulting in an overall positive pressure trend, following eq. 3:



In addition to the generation of H₂ by W4, Figure 3D also indicates an increase of CO₂ not present in W2. The addition of LiPAA binder in W4 is likely the source of the CO₂, as this is not included in the gas composition of W2. Decarboxylation of polyacrylic acid has been demonstrated in aqueous solutions, according to eq 4: [13]



This reaction may not only lead to the decomposition of the binder, but also drives the pH of the slurry towards more basic conditions.

XPS data (Fig. 13) were collected on dried powders to determine the change in oxidation of the NA 70-130 Si after mixing. All plots were normalized to SiO₂ 2p peak at 103.6 eV. The variations in the intensities of peaks at 99.3 eV were caused by changes in the Si⁰. The spectra can be fitted to a 3 peak model coordinating with Si, SiO₂, and an oxygen deficient form of silica deemed SiO_x (~102 eV). The untreated Si comprised of Si, SiO₂, and SiO_x. After treatment in water, the Si⁰ signal decreased, signifying either the oxidation of Si or a buildup of products at the surface attenuating the Si⁰ signal. The untreated Si shows the greatest Si⁰ signal, followed by a decrease in W1 and N1 (which are largely overlapped in Figure 4). The fact that these spectra are so well overlapped lends towards the first scenario (Si oxidation), since N1 contains CB and there is no visible change in profile compared to W1, which contains only Si. If the CB was uniformly coating Si, it would be expected that the Si⁰ peak of N1 would be smaller. In addition, the XRD and NMR also support a thicker oxide (see below). The XPS data from W1 and N1 also show an increase in the shoulder at 102 eV when compared to other

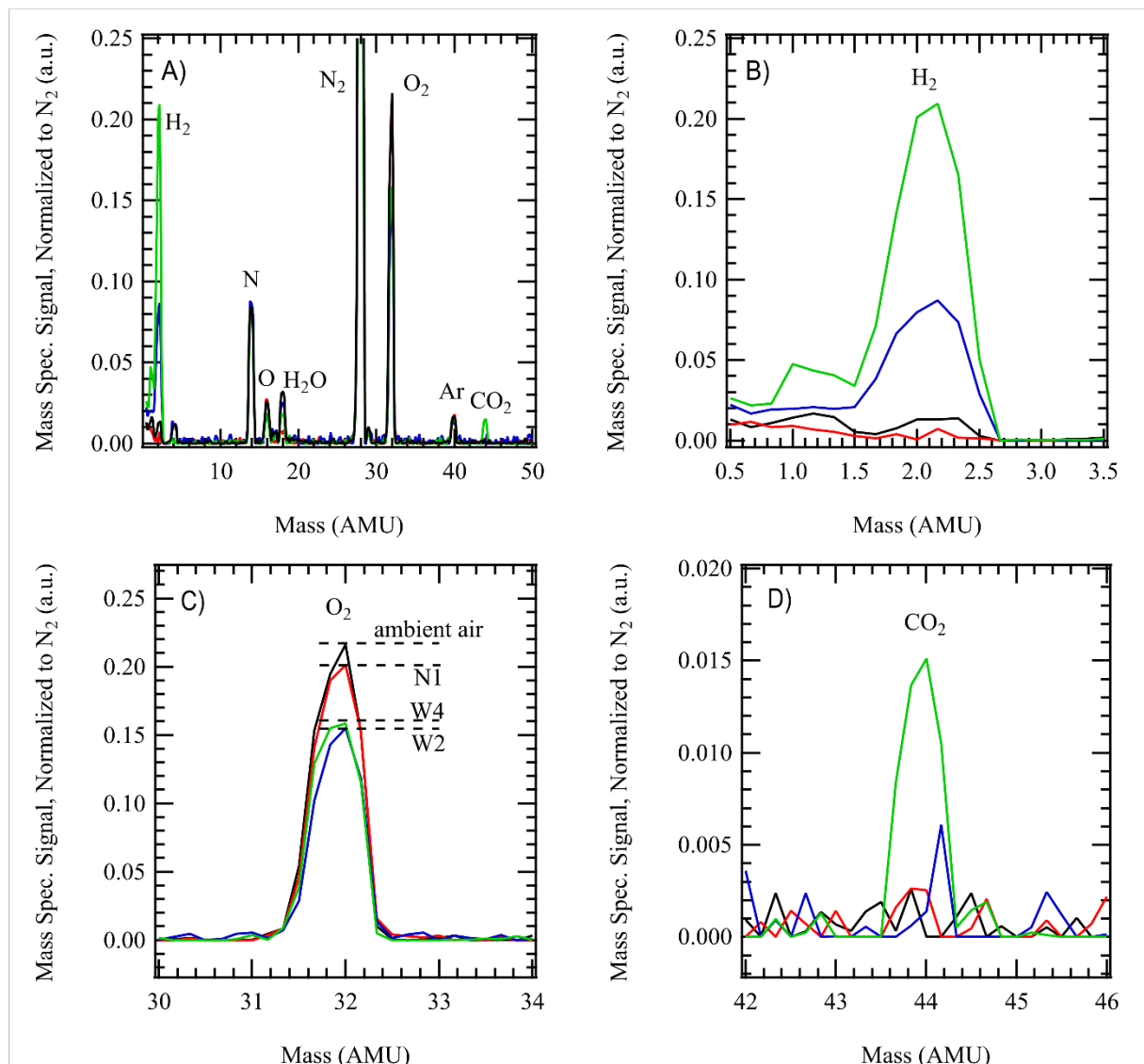


Figure 12A) Mass spectrum of gas collected from head space of mixing vessel for W2 (blue trace), W4 (green trace), and N1 (red trace), normalized to the N₂ signal of ambient air (black trace). B) Zoomed in plot of H₂ signal in mass spectrum from 2A. C) Zoomed in plot of O₂ signal in mass spectrum from 2A. D) Zoomed in plot of CO₂ signal in mass spectrum from 2A.

samples, which implies that a greater extent of the oxide shell is converted to the less oxidized SiO_x phase. This means that the reaction leads to a different oxide composition depending on whether the oxidation occurs by O₂ consumption (eq. 1) or H₂O (eq. 2). W2 and W4 display even greater loss in the Si⁰ signal, meaning the oxidation by water results in an oxide shell that penetrates even further into the Si particle. It is also interesting to note that the addition of LiPAA in W4 has little effect on the Si⁰ signal. Like the CB, this implies that the binder is not uniformly coating the Si particles, which may have implications towards the cycle-ability of Si based anodes.[14]

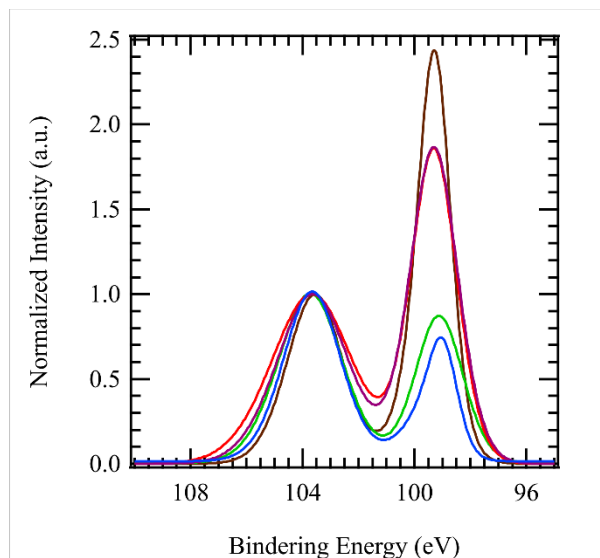


Figure 13 XPS of Si 2p orbitals, Normalized to Si⁴⁺ at 103.6 eV, of various dried Si samples (untreated nano Si – brown trace, N1 – red trace, W1 – purple trace (overlapping with N1), W4 – green trace, W2 – blue trace)

Knowing that processing Si in water, under certain conditions, causes a change in the oxide content and surface chemistry, we cycled Si based half cells with and without the 100 hours of mixing. NA 70 – 130 Si, with a much shorter processing time, was compared to W2 to identify differences in electrochemical performance. In the voltage profile, shown in Figure 5, the half cell containing the unprocessed Si has a 1st cycle delithiation capacity of 1392 mAh g⁻¹. The 2nd cycle delithiation capacity decreases to 1128 mAh g⁻¹. The half cell containing W2 has 1st and 2nd delithiation capacities of 566.9 and 417.4 mAh g⁻¹, respectively. While this slurry formulation was not optimized, accounting for the lower than theoretical capacity, it is immediately noticeable that the 1st cycle delithiation capacity of the short-processed Si is more than twice the capacity of W2. This could arise due to some portion of the Si particles becoming electrochemically inactive, due to a thick oxide shell, or because whole particles are electronically isolated because of poor mixing. The first circumstance seems more likely, because W2 was mixed for 100 h, compared to the short-processed sample which was only mixed for a few minutes. Moreover, there is a larger hysteresis between the lithiation and delithiation curves of the half cell containing W2. This also supports a thicker oxide shell on the Si particles that would decrease its electronic conductivity, leading to a larger IR drop. In addition to capacity, the 1st cycle coulombic efficiency of the half cell using the unprocessed Si is 64%, whereas W2 is 40%. This difference may result from the additional SiO_x in W2, which undergoes an electrochemical conversion to Li₂O, Li₂SiO₃, and Li₄SiO₄, or by the decomposition of more organic electrolyte.⁹ Overall the half cell containing W2 only lost 149.5 mAh g⁻¹ between the 1st and 2nd delithiation compared to 264.1 mAh g⁻¹ for the short-processed Si. This improved capacity retention between the 1st and 2nd cycle could result from better dispersion of W2, less electrochemically active Si overall in this electrode, elimination of reactive sites, or less SEI.

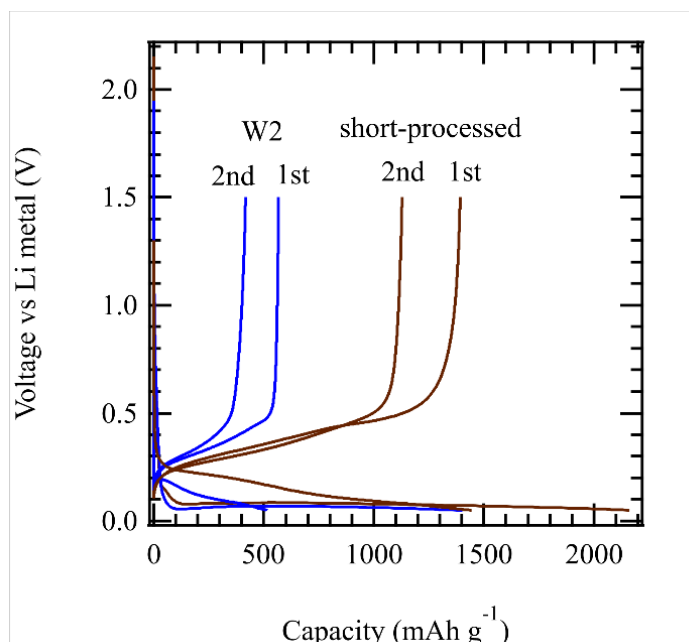
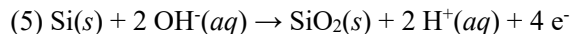
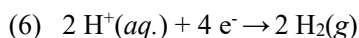


Figure 14 Voltage profile of Si-Li metal half cells comparing short-processed NA 70 – 130 Si (brown trace) and W2 (blue trace). Cycled at C/10 (0.25 A g⁻¹) from 1.5 to 0.05 V vs Li metal.

The generation and consumption of gas in these slurries is, for the most part, a direct result of Si oxidation during slurry preparation. Furthermore, solvent contribution alone is not the limiting factor (Table 1), rather the addition of CB played a role in promoting the oxidation of the Si particles. Based off gassing results of the NA 70 - 130 Si particles from the water slurries, the W2 and W4 (contained CB) suffered the greatest amount of oxidation while W1 and W3 (no CB) showed the least, confirming CB is a key reagent. Though W4 produced more gas than W2, W4 also produced CO₂, which cannot be decoupled from the pressure of H₂ in Figure 11. In fact, both W2 and W4 displayed similar oxidation based off XRD and XPS, meaning this difference gas production of 0.25 atm, after 100 h, could, in part, be caused by CO₂. We believe the CB acts as a high surface area catalytic site in which a proton coupled, charge transfer could take place,[16] following the scheme found in Figure 15. Both OH⁻ and H⁺ readily diffuse through amorphous SiO_x. [17-18] Despite the acidic environment, the natural dissociation of water provides sufficient OH⁻ ions, which could diffuse through the amorphous SiO_x and oxidize the Si⁰ core according to eq. 5:



This reaction is followed by the reverse diffusion of H⁺ opposed to molecular H₂, which alleviates the need for additional porosity to allow the escape of gas. The diffusion of 2 H⁺ out of the SiO_x occurs in tandem with a 4 e⁻ transfer to the local CB, providing a site for aqueous H⁺ reduction, eq. 6:



In this proposed scenario the CB lowers the activation energy needed to reduce the protons, which may not take place on the SiO_x surface alone.

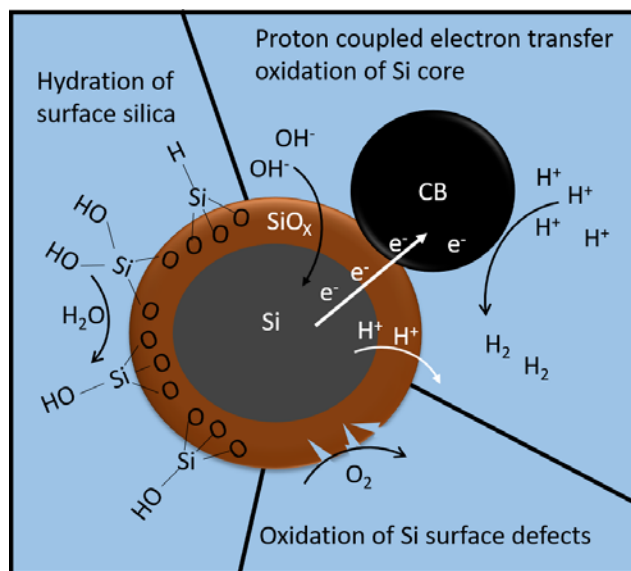


Figure 15. A representative schematic of several reactions that occur during processing of water based Si/CB slurry.

Electrode Characterization: Raman Spectroscopy

Raman spectroscopy has been used as a tool to characterize heterogeneity in silicon-graphite composite electrodes. Our Raman results clearly show evidence for phase segregation and non-uniform electrochemical cycling of the active silicon component, indicative of a greater need to understand how the slurry properties effect the formation of the final composite electrodes when materials with such different surface chemistries are used. Electrode heterogeneity and non-uniform lithiation is a primary driver of battery failure.

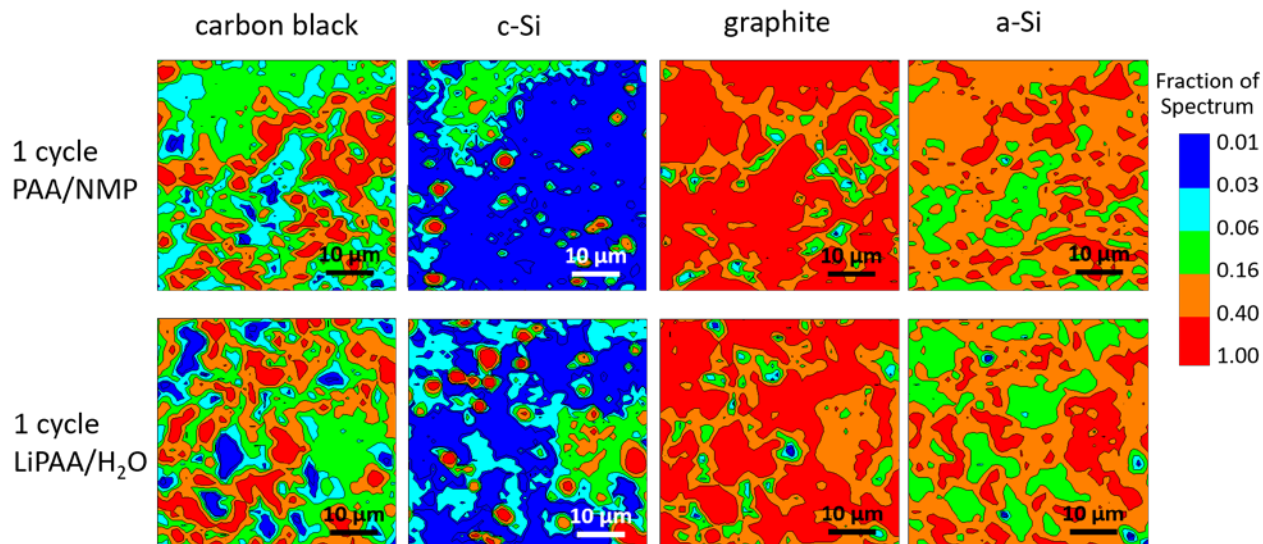


Figure 16 Raman maps of the distribution of carbon black, c-Si, graphite, and a-Si in Si-Gr composite anodes after 1 full cycle (lithiation and delithiation). The top row maps an anode made with PAA binder and the bottom row maps an anode made with LiPAA binder. Each map is 50 μm x 50 μm and comprises 2500 spectra. The color scale indicates the relative fraction of each component at each location across the map.

Binder: Processing the electrodes with PAA binder in NMP yielded a more uniform composite than water-based processing with LiPAA binder. The anodes processed from water showed higher levels of segregation for the silicon and graphite phases. In general, NMP-based processing resulted in better wetting and dispersion of silicon nanoparticles and carbon black in the slurry, which was reflected in the dried electrode. Despite differences in the quality of the pristine coatings, the first-cycle lithiation proceeded identically independent of the electrode binder (Figure 16). Both electrodes contained c-Si after one cycle, which indicates that some Si did not participate in the electrochemical reaction and convert to amorphous phases. Regions of electrochemically inactive Si were similar in size and extent in electrodes with PAA and LiPAA binder. Based on these data, the electrode uniformity and reactivity during the first cycle cannot explain the improvements in long-term performance of the LiPAA-based anodes compared to the PAA-based anodes and we believe factors such as residual moisture in the electrode appear to dominate. .

On cycling, we observed domains of crystalline Si in the cycled composite anodes (Figure 17), indicative that some fraction of the Si is electrochemically inactive (does not lithiate) and thus does not undergo a crystalline

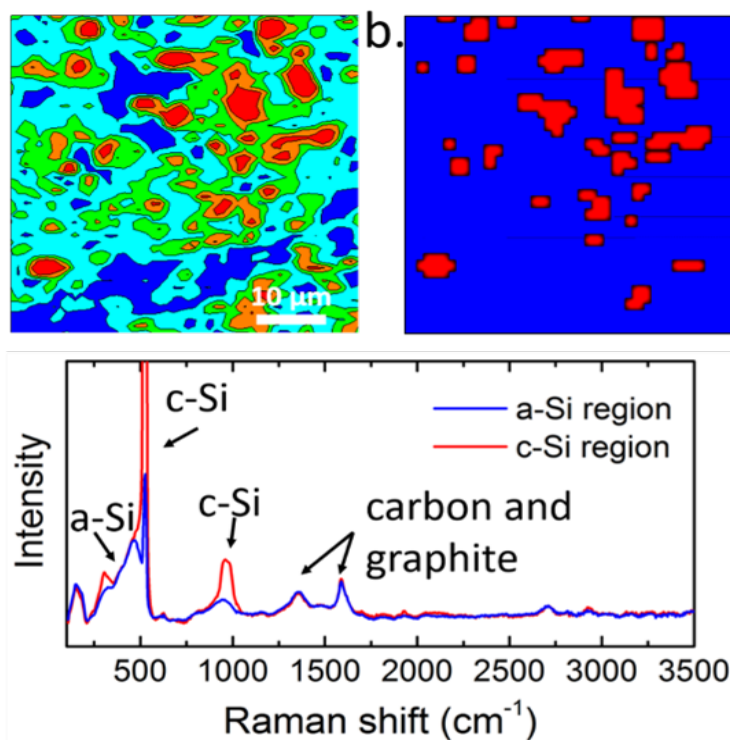


Figure 17. (a) Raman map of the intensity of the main band from crystalline silicon at 520 cm^{-1} in a silicon-graphite composite electrode after 1 charge-discharge cycle. The fraction of crystalline silicon increases from blue to red. (b) Two level map of the same data presented in (a). The red pixels are from the electrode areas with the highest concentration of crystalline silicon. (c) The average Raman spectra from regions with high and low concentrations of crystalline silicon is mapped in (b).

to amorphous transition. Inactive Si was observed even after 100 cycles in full cells and in half cells with a virtually infinite supply of active lithium. To understand if the inactive regions of the electrode could be electronically isolated, we collected Raman spectra from a large area ($50 \times 50 \mu\text{m}$, 2500 pixels) and broke it into two groups to separate out the spectra with the largest fraction of crystalline silicon (Figure 17b). No difference in the intensity of the bands from carbon and graphite were observed in the spectra with the most crystalline silicon compared to all other regions of the electrode (Figure 17c). Differences in carbon content do not explain

why some Si is electrochemically inactive and suggest that electronic conductivity is not the limiting factor. This points to a need to further improve electrode processing.

In addition to using Raman spectroscopy to elucidate the uniformity of the electrode and level of particle isolation, it also can be used to study the solid electrolyte interphase (SEI) layer. In this context, we characterized the SEI layer on silicon by using surface-enhanced Raman spectroscopy (SERS). Although SERS normally introduces metallic islands in the SEI layer that may lead to non-representative results, it is a powerful tool that may under certain conditions yield insights into the SEI layers structure and composition. In this study, we utilized Cu nanoparticles on the surface to increase the Raman signal. Copper was chosen as the metal nanoparticle surface because it does not react/alloy with lithium and is already a constituent in the cell.

The silicon laminate electrode was provided by the CAMP Facility at Argonne. It consisted of 70.7 wt% Nano&Amor Si particles (70 nm to 130 nm), 9.4 wt% Timcal C-45 conductive additive and 19.9 wt% polyacrylic acid-lithium salt (LiPAA). The methodology followed to prepare the Cu-coated electrodes utilized a solution-based reduction in an aqueous solution of $\text{Cu}(\text{SO}_4)_2$ with application of the appropriate voltage and current. With the purpose of finding the optimum Cu electrodeposition, six different protocols were examined, as shown in **Table 6**.

Table-6 Electrodeposition protocols applied to prepare the Cu-coated silicon electrodes.

Sample	Voltage (mV) vs. Ag ⁺ /Ag	Charge (C/in ²)
1	-461	0.2
2	-711	0.2
3	-961	0.2
4	-711	0.6
5	-711	1.8
6	-961	0.6

The copper distribution and size varied from sample to sample, as a function of the protocol employed (see **Fig. 18**). Samples 1, 3 and 4 exhibited a more evenly dispersed copper than samples 2, 5 and 6, in which the copper particles were randomly distributed. At higher magnifications (bottom images of **Fig. 18**), the size of copper particles varied from tens (sample 4) or hundreds of nanometers (sample 3) to micron size (sample 2), for instance.

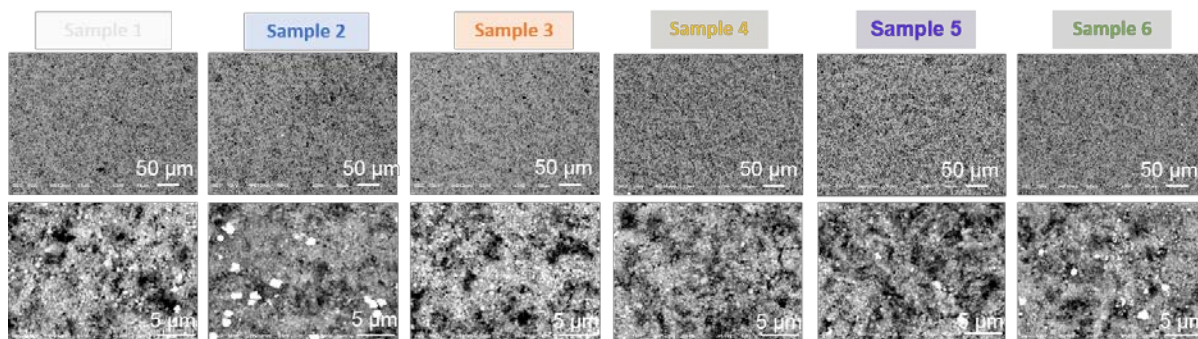


Figure 18. SEM images of the different Cu-coated silicon electrodes obtained by applying the 6 different electrodeposition protocols collected in Table 2.

For these samples, only sample 1 showed a signal enhancement. As copper is only weakly active for the purpose of SERS-based signal enhancement when compared to the more commonly used silver or gold nanoparticles (Figure 19). For the sample that showed the most enhancement, the signal strength (related to the amount of copper deposited) was insufficient to significantly enhance any additional peaks compared to the baseline samples.

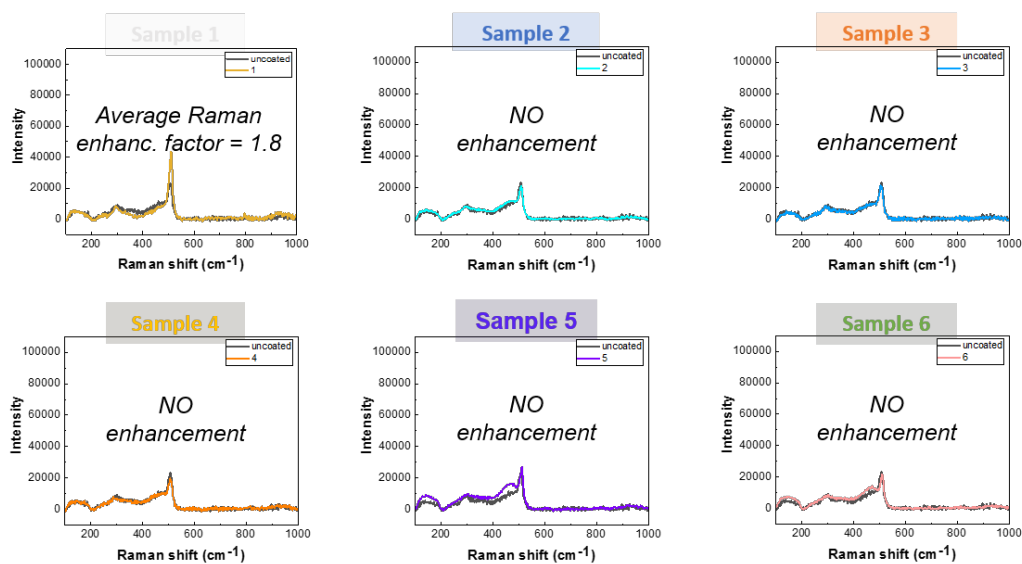


Figure 19 Raman spectra of the different Cu-coated silicon electrodes obtained by applying the 6 different electrodeposition protocols collected in Table 2.

Charged Silicon Electrode Reactivity

One of the core problems associated with Li-Si chemistry in Li-ion batteries is the inherent reactivity of the lithium silicides, the active material that forms upon the lithiation. These phases can react with almost all battery components such as binders, electrolytes, additives and impurities such as moisture and air, which cause Li loss and irreversible capacity, as well as continuously low coulombic efficiencies during cycling, leading to electrode death.

To systematically study the reactivity of different battery components (including binders and electrolyte solvents) in direct contact with lithiated Si electrodes, crystalline lithium silicide (LS) with the Li_7Si_3 composition is synthesized as the model compound, which is associated with voltage of approximately 350 mV (vs Li) [19]. Li-Si phase diagram and crucible studies were used to optimize the material synthesis conditions and procedures. The chosen process was found to be a stoichiometric mixture of Si and Li, Ta crucibles, with a heating ramp to 750 °C, followed by a one-hour hold, all under an argon atmosphere. Initial samples were near single phase Li_7Si_3 by powder X-ray diffraction (XRD) and ^{29}Si NMR. After this method was identified, we started to re-focused on a scale-up synthesis of crystalline LS compounds for team members to use these in the continued stability studies. The XRD of the as-synthesized scale-up LS sample is shown in Figure 20, which are mainly Li_7Si_3 phase with a little less-lithiated $\text{Li}_{12}\text{Si}_7$ phase.

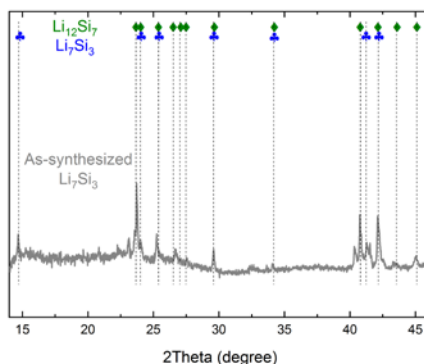


Figure 20. XRD of as-synthesized Li_7Si_3 , with a small amount of the slightly oxidized phase $\text{Li}_{12}\text{Si}_7$.

To study the reactivity of different binder materials in contact with lithiated Si electrodes, X-ray diffraction and Solid State Magic Angle Spinning (MAS) NMR spectroscopy have been used to qualitatively and quantitatively study the evolution after grinding the lithium silicides model compounds with different binder materials, such as LiPAA and PVDF, under the Ar environment. It is found that compared with PVDF, LiPAA lead to less chemical shifts in ^7Li and ^{29}Si MAS NMR and less structural evolution in XRD results after mixed and ground with Li_7Si_3 model compounds (see Figure 21). Particularly, compared with the Li_7Si_3 + LiPAA mixture, the main ^7Li peak at ~16 ppm moved to much higher ppm after mixing Li_7Si_3 with PVDF, which according to the previous NMR study [20,21] representing more delithiation of lithium silicides and worse chemical stability in contact with the charged Si species. Meanwhile, the new ^7Li peak appeared at ~0 ppm in the Li_7Si_3 + PVDF mixture indicating the formation of new diamagnetic Li species coming from the degradation of PVDF. In general, PVDF showed less chemical stability when in contact with lithiated Si species compared with LiPAA, indicating PVDF is a less preferable binder material used for Si anode.

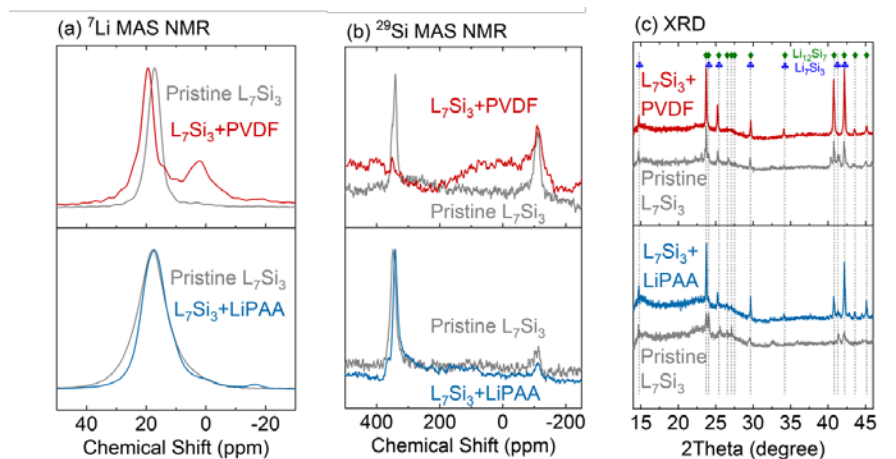


Figure 21. (a) ${}^7\text{Li}$ NMR, (b) ${}^{29}\text{Si}$ NMR, and (c) XRD results of pristine LS samples and their mixture with 10 wt% PVDF or LiPAA.

To explore the degradation mechanism of PVDF in contact with the lithiated Si electrodes, the ${}^1\text{H}$, ${}^{13}\text{C}$ and ${}^{19}\text{F}$ MAS NMR spectra of the mixture of Li_7Si_3 and PVDF were measured, as shown in Figure 22. Compared with the pristine PVDF, the mixture of Li_7Si_3 and PVDF showed a broadened ${}^1\text{H}$ peak and several new ${}^{13}\text{C}$ peaks, indicating the potential breaking of C-H and C-C bonds in the PVDF $(-\text{CH}_2-\text{CF}_2)_n$ structure. In the case of ${}^{19}\text{F}$ NMR results, although the relative peak intensities changed after mixing PVDF with Li_7Si_3 , no obvious peak broadening or new chemical environment, including LiF, was observed, indicating that the C-F bonds are relatively stable during the degradation of PVDF in contact with Li_7Si_3 .

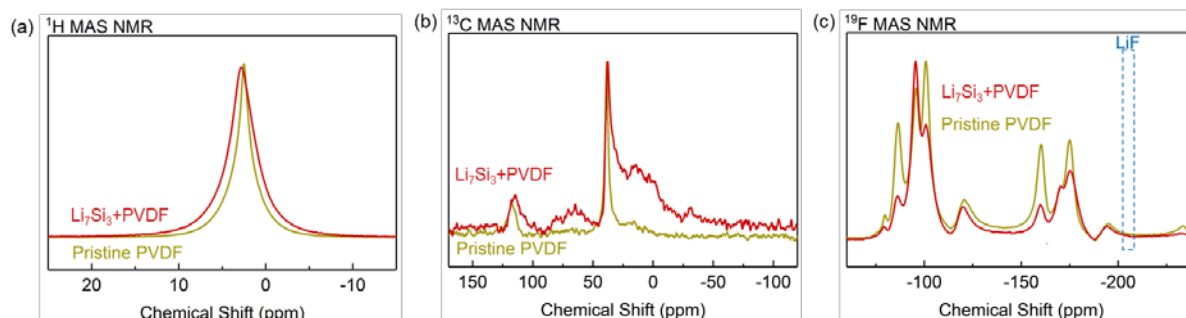


Figure 22. (a) ${}^1\text{H}$, (b) ${}^{13}\text{C}$, and (c) ${}^{19}\text{F}$ MAS NMR spectra of pristine LS samples and their mixture with 10 wt% PVDF..

The potential breaking of C-H bonds by the extremely reducing Si anions in LS may lead to the formation of H_2 . To confirm this hypothesis, we designed a special gas-trapping setup to catch the potential gas generation after mixing PVDF with Li_7Si_3 . Initially, pristine PVDF powder and pristine ground LS powder were put at the two ends of a glass vial, as shown in the top left image in Figure 4, to minimize their contact before mixing. A hole was drilled on the cap of the vial, and a totally-flat balloon was bonded to the cap to catch the generated gas. The cap was tightly screwed onto the glass vial, with additional parafilm sealing to prevent the gas leaking. Then the sealed system was hand-shaken for 10 min to physically mix the PVDF with LS. Due to the loose contact and limited mixing between LS and PVDF after the hand shaking, no clear gas generation was observed immediately after the mixing, as shown in the bottom left image in Figure 23. After sitting in the glovebox for 1 day, notable gas formation was observed with the balloon being inflated, as shown in the right image in Figure 23.

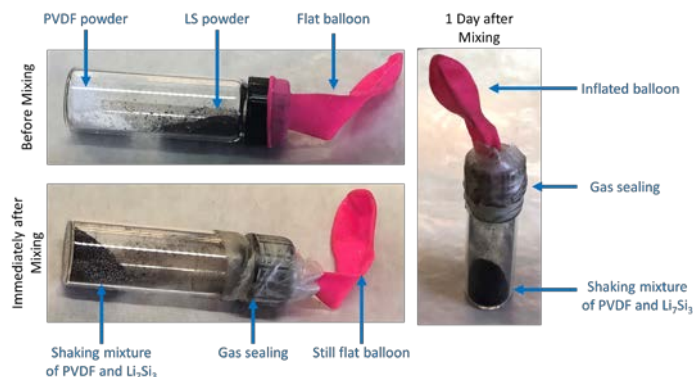
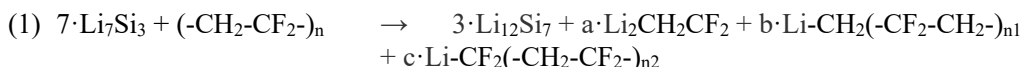
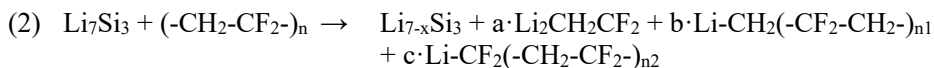


Figure 23. Images of gas-catching setup before, immediately after, and 1 day after the mixing of PVDF and Li_7Si_3 .

Based on the above characterization results, here we proposed several potential reaction mechanisms between Li_7Si_3 and PVDF after physical mixing. In one possibility, the severe delithiation of Li_7Si_3 in contact with PVDF may cause its transformation to a lower-Li-concentration phase such as $\text{Li}_{12}\text{Si}_7$. Meanwhile, the C-C bonds may be broken and lithiated to form organolithium complexes. The reaction could be written as below:

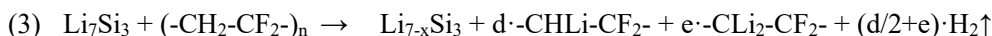


Here $a + b + c = 13$, representing different amounts of Li complexes formed. Since the phase transition from Li_7Si_3 to $\text{Li}_{12}\text{Si}_7$ requires a big change in the Si skeleton, such reaction maybe kinetically hindered. In another possibility, Li may leave the Li_7Si_3 structure without disturbing the Si skeleton too much, forming a less-lithiated silicide phase with crystal, semi-crystal, or even amorphous structures. This will give us:

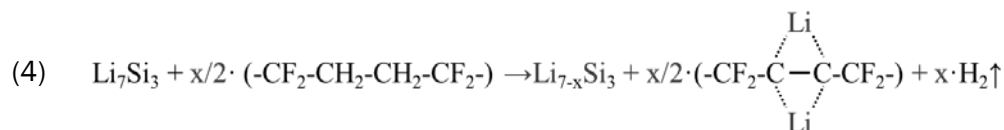


Here $a + b + c = x$.

In addition to the C-C bonds, the C-H bonds could also be broken and lithiated after mixing LS with PVDF, with protons being reduced to H_2 , as shown in Figure 2. The potential reaction can be written as below:



Moreover, in PVDF there are usually some structural defects, such as the existence of $-\text{CF}_2-\text{CH}_2-\text{CH}_2-\text{CF}_2-$ sequence.^{35, 36} The replacement of two adjacent C-H bonds with C-Li bonds may overly reduce the C-C bond to a $\text{C}\equiv\text{C}$ triple bond, as is shown below:



In all reaction equations listed above, the C-F bonds were keep intact, because no sign of loss of fluoride from the PVDF or LiF formation was observed in ^{19}F NMR after the reaction between Li_7Si_3 and PVDF. To screen out the real PVDF degradation mechanism, further characterization supports from FTIR, Raman and XPS techniques will be applied in the future.

In addition to the binder materials, we also used LS model compounds to investigate the stability of electrode solvents in contact with lithiated Si electrodes. Figure 24 shows the ^7Li and ^{29}Si MAS NMR results of the LS model compound and its mixture with different electrolyte solvents, including EC, EMC, FEC and triglyme.

The results showed the highest Li loss and bulk reaction for EC and the lowest for FEC/triglyme after mixing with Li_7Si_3 . Furthermore, no LiF at ~ 0 ppm in ^7Li NMR was detected in the Li_7Si_3 + FEC experiment, contrary to common belief that FEC de-fluorination reaction would be prevalent in the presence of lithiated Si species. The FEC results suggest either Li_7Si_3 of about 300-400mV potential vs. Li is not reducing enough and/or a flow of electrons is also required for FEC passivation reaction.

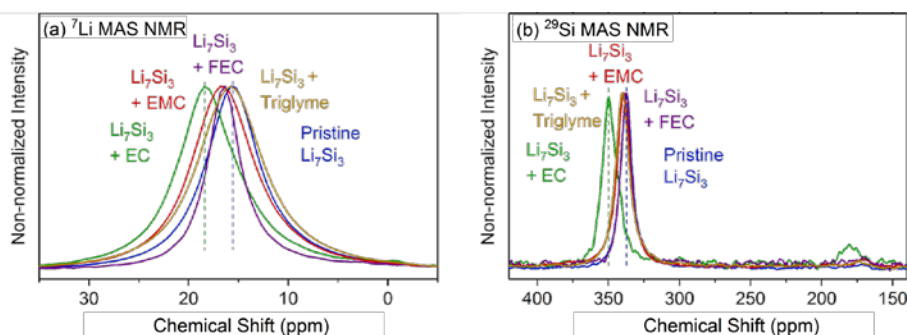


Figure 24. (a) ^7Li and (b) ^{29}Si solid state MAS NMR for Li_7Si_3 and its mixture with different electrolyte solvents.

To test the hypothesis that the Li_7Si_3 -stable solvents such as FEC may react with more deeply lithiated Si species, new LS model compound with higher Li contents (i.e. representing lower charging potential) were synthesized. The newly synthesized lithium silicide was identified as $\text{Li}_{21}\text{Si}_5$ according to its ^7Li MAS NMR spectrum shown in Figure 6a, which corresponds to about 0.05-0.1 V vs. Li during the lithiation of Si electrodes [22,23]. The ^7Li and ^{29}Si MAS NMR results of the mixture of $\text{Li}_{21}\text{Si}_5$ and different electrolyte solvents, including EC, FEC and triglyme, are shown in Figure 25. After mixing with EC, the main ^7Li peak of $\text{Li}_{21}\text{Si}_5$ at ~ 75 ppm shifted by ~ 4 ppm, indicating EC is still pretty reactive in contact with $\text{Li}_{21}\text{Si}_5$. Meanwhile, unlike the minor ^7Li and ^{29}Si NMR shifts previously observed after mixing Li_7Si_3 with FEC and triglyme (see Figure 5), this time clear positive peak shifts and notable broadening were observed after mixing $\text{Li}_{21}\text{Si}_5$ with FEC and triglyme, indicating that although FEC and triglyme might be relative stable when in contact with the slightly-lithiated Si anode, it could react with the Si anode lithiated to lower voltages. In addition, in the ^7Li MAS NMR spectra shown in Figure 25a, a clear diamagnetic ^7Li peak around 0 ppm (representing LiF) appeared after mixing $\text{Li}_{21}\text{Si}_5$ with FEC. This means our earlier observation that the mixing of FEC and Li_7Si_3 causes no LiF formation is because Li_7Si_3 is not reducing enough. When the Si anodes are further lithiated and more reducing LS such as $\text{Li}_{21}\text{Si}_5$ are formed, FEC will start to react with the charged anodes, forming LiF through the defluorination process, which is consistent with the common belief mentioned earlier.

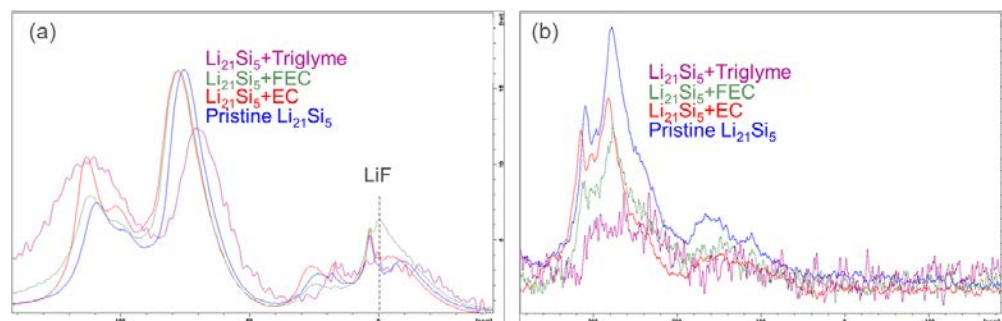


Figure 25. (a) ^7Li and (b) ^{29}Si in-situ solid state MAS NMR for $\text{Li}_{21}\text{Si}_5$ and different electrolyte solvents. ANL, unpublished results.

Based on the reactivity study results and due to the lack of literature results on glymes and silicon electrodes, a preliminary test of the electrochemical performance of a triglyme-based electrolyte formulation (1M LiTFSI in triglyme) was studied via a simple baseline silicon powder and hard carbon mixture in half cells. Figures 26a show the electrochemical profile comparison of the new triglyme-based electrolyte vs. the baseline Gen 2 + 10wt% FEC electrolyte, suggesting no major changes in the overall lithiation and delithiation electrochemistry. The 1st cycle electrochemical performance, shown in Figure 26a, was about 75% higher in discharge capacities than the baseline electrolyte (Gen 2 + 10wt% FEC). This result alone is consistent with the hypothesis that the inertness of the electrolyte system could minimize side reactions and improve the overall capacity that can be obtained from silicon. While the baseline electrolyte capacities are lower in the first few cycles, they rapidly stabilize and are consistent for 10+ cycles, whereas the triglyme electrolyte performances are never found to stabilize and decay fast, with much lower coulombic efficiency (see Figure 26b). This behavior could be explained by a lack of passivation on the electrode surface and/or Li-salt side reactions on the Li metal when using the new triglyme-based electrolyte. Figure 26c illustrates an attempt to simply incorporate a passivation aid, FEC, to the system, which improved the initial coulombic efficiency (Figure 26d) but did not improve the overall cyclability. The instability of triglyme-based electrolyte is consistent with the $\text{Li}_{21}\text{Si}_5$ highly-lithiated model compound test results shown in Figure 6 that the Li_7Si_3 -stable solvents like FEC and triglyme can be reactive in contact with more deeply lithiated Si species. The above results suggest triglyme solvents are not stable enough as the electrolyte solvent for Si anodes. New carbonate electrolyte formulations are required to further improve the coulombic efficiency. Meanwhile, more basic characterization studies are required to study the degradation of triglyme-based electrolytes (e.g. full-cell electrochemistry, NMR, electron microscopy, FTIR and XPS) in order to optimize the triglyme-based electrolyte for Si electrode applications.

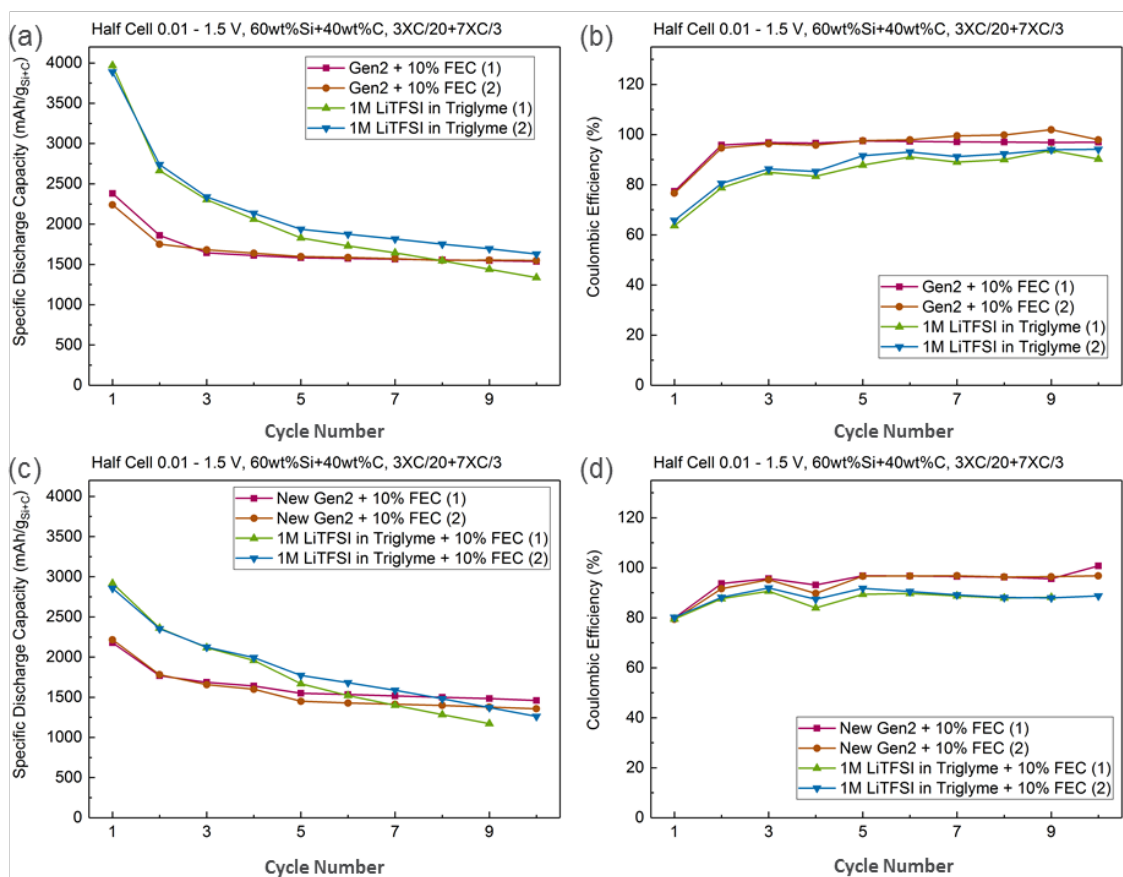


Figure 26. Electrochemical profiles of Paraclete baseline silicon powder and carbon SP electrodes vs. Li metal half cells comparing Gen2 + 10% FEC and 1M LiTFSI in Triglyme electrolytes. ANL, unpublished results

To understand the potential degradation mechanism of triglyme-based electrolytes used for Si electrodes, we measured the chemistry evolution of the Si anodes in half cells cycled between 0.01-1.5 and 0.05-1.5 V vs. Li respectively for 15 cycles using 1 M LiTFSI in triglyme as the electrolyte, as shown in Figure 27. The ^{13}C NMR results indicated that the reaction between triglyme solvents and charged Si anodes could cause the degradation of triglyme into ethylene glycol and some other organic compounds. Additionally, lower cut-off voltage of 0.01 V for Si anode charging process led to the formation of a new ^7Li peak at ~ 10 ppm compared with that charged to 0.05 V vs. Li, implying that more reducing lithium silicides could trigger additional reactions with the electrolyte solvents. In the future, further NMR characterizations together with microscopy, FTIR and XPS techniques will be applied to understand the true degradation mechanism of triglyme system in contact with charged Si anodes in both half-cell and full-cell electrochemistry measurements.

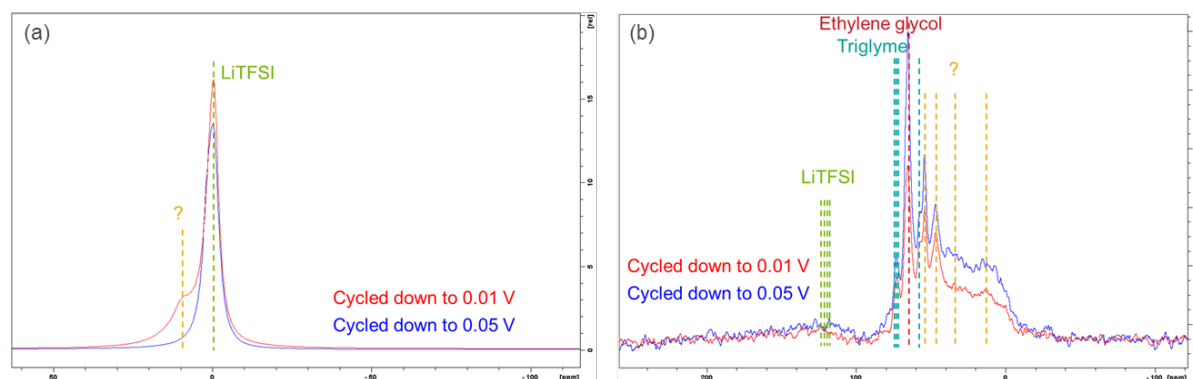


Figure 27. (a) ^7Li and (b) ^{13}C solid state MAS NMR for post-electrochemistry Si loose-powder anodes after cycling between 0.01-1.5 and 0.05-1.5 V vs. Li respectively for 15 cycles, using 1 M LiTFSI in triglyme as the electrolyte. ANL, unpublished results.

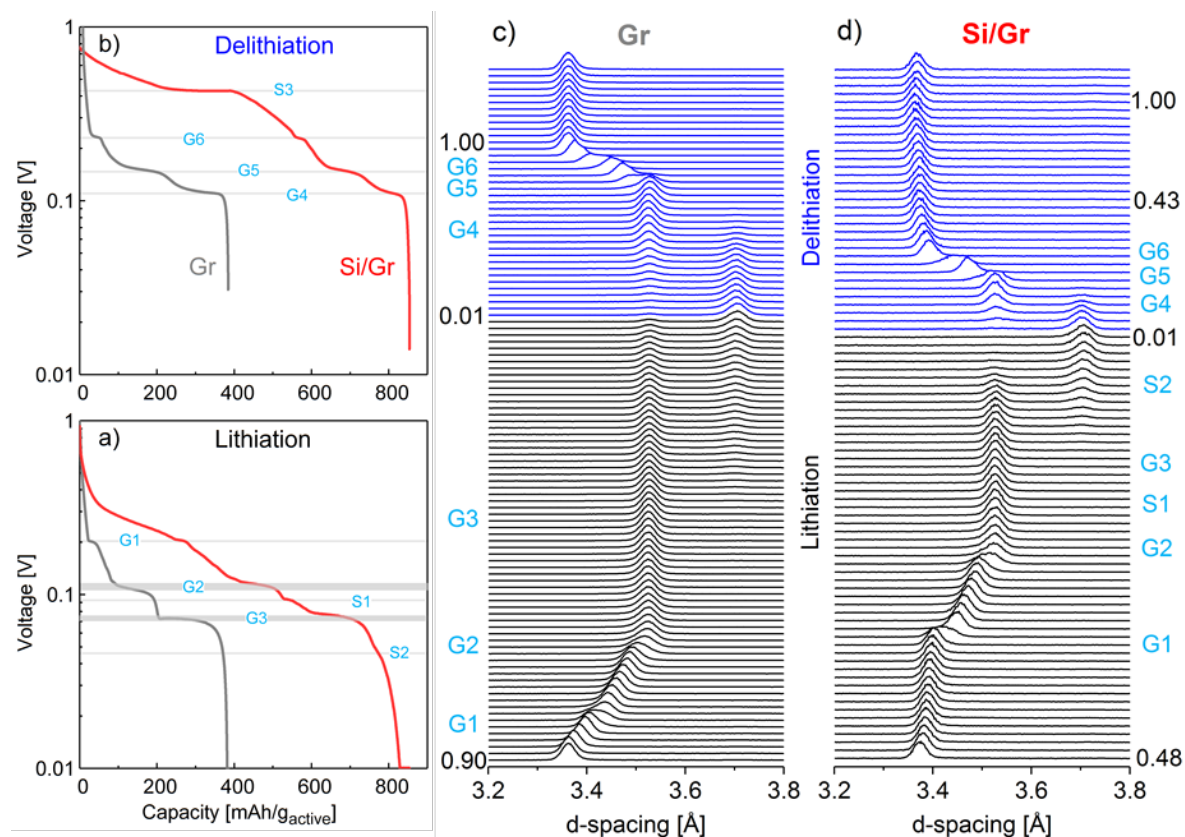
Silicon Electrode Electrochemistry

The use of blended silicon-graphite (Si-Gr) negative electrodes increases the energy density of lithium-ion cells over those containing only graphite (Gr) electrodes. However, the potentials and kinetics of lithium insertion into (and extraction from) Si and Gr are known to be different. Silicon is active in the entire 1.0-0.0 V range, whereas Gr is active only at potentials < 0.25 V vs. Li/Li^+ during electrochemical cycling in (half) cells containing a Li-metal counter electrode. However, the relative lithiation/delithiation behavior of the Si and Gr components in blended electrodes is not well understood. Knowledge of the distribution of Li^+ ions in the Si and Gr components is important because (in addition to electrode porosity) it determines the volume expansion of the blended electrode during electrochemical cycling. One reason for the knowledge gap is the amorphization of crystalline Si that occurs during lithium insertion, which makes it difficult to track the evolution of the component by techniques such as X-ray diffraction. We conducted operando energy dispersive X-ray diffraction (EDXRD) to quantify lithiation/delithiation of Gr in a 15 wt% Si-Gr (Si-Gr) blended electrode; then, by taking into account the measured coulometric capacity of the cell we inferred the lithiation/delithiation behavior (and hence the volume changes) of the Si component. In parallel, we also conducted operando studies on a Gr electrode and used the data to calibrate behavior of the Gr component in the blended electrode. The EDXRD data were collected on cells containing a Li-metal counter electrode (*half* cells) at the 6BM-A beamline of Argonne's Advanced Photon Source (APS). The 2032-type coin cell was used without any modification as the white beam (5-250 keV) penetrates the stainless steel casing.

The volume changes in the Si particles that occur during cycling causes deterioration of the solid-electrolyte interphase (SEI) layer on the particles resulting in further electrolyte reduction that immobilizes Li^+ ions and, therefore, capacity fade. A natural question to ask is whether the observed fast capacity fade in Si-Gr electrodes

vs. Gr electrodes (for which the volume variation is $< 10\%$) is solely due to the volume changes, or if there are other compounding factors that are specific to Si particles alone? To answer this question we developed a calendar-aging test, which included a potentiostatic hold. Full cells with Si-Gr and Gr negative electrodes (and $\text{Li}_{1.03}(\text{Ni}_{0.5}\text{Co}_{0.2}\text{Mn}_{0.3})_{0.97}\text{O}_2$ containing positive electrodes) were assembled, tested, and compared using complementary cycle-life and calendar-life aging protocols. Because the Si particles volume changes are not expected to occur during a potentiostatic hold, by comparison of data from the cycle-life and calendar-life aging tests we were able to assess the role of volume changes in the deterioration of cell cycling performance. In order to gain insights into the capacity loss mechanisms we examined the cell electrolytes after completion of the electrochemical tests. The electrolyte samples were collected into polypropylene containers, diluted 1:10 v/v with CD_3CN , and analyzed by nuclear magnetic resonance (NMR) spectroscopy. ^{19}F and ^{31}P NMR spectroscopy data were obtained on the electrolyte samples to track PF_6^- hydrolysis, as the products have different chemical shifts from the parent compound. For accurate integration of the ^{19}F and ^{31}P NMR resonances, 10-15 s delays were introduced between the excitation radiofrequency pulses. For comparison purposes, we also conducted measurements on the fresh electrolytes, and on samples from as-prepared full cells that were held at open circuit for ~ 130 h after assembly *but never cycled*. These latter samples provided information on changes in the electrolyte during electrode “soaking”, which was compared with changes to the electrolyte after formation cycling (~ 130 h is the time elapsed for three $C/20$ formation cycles).

The electrode potential vs. capacity profiles and the XRD data from the operando lithiation and delithiation



cycles are displayed in Figure 1. Prior to collecting these data, the 2032-type coin cells were cycled two times at a $\sim C/20$ rate in the 1.50-0.01 V vs. Li/Li^+ (abbreviated as V_{Li}) range to form the SEI on the Gr (or Si-Gr).

Figure 28 Electrode potential vs. capacity during lithiation (a) and delithiation (b) of a Gr-only electrode (grey line) and of a Si/Gr (15/73 w/w, red line) blended electrode cycled vs. Li metal. Operando XRD spectra (shown in the 3.2 to 3.8 Å d-spacing range) collected during the electrochemical cycling in (a) and (b) for the Gr-only (c) and Si-Gr (d) electrodes. Spectra collected on lithiation and delithiation are shown in black and blue coloring, respectively.

The electrochemistry data in Figure 28 shows several plateaus in the voltage profile. On lithiation at $\sim C/30$ rate (Fig. 1a), starting from ~ 1.5 V to a 10 mV cut-off, three major plateaus are seen for the Gr-only electrode, at 0.202 (G1), 0.106 (G2), 0.072 V_{Li} (G3). For the Si-Gr electrode, five plateaus are observable at voltages values of 0.206 (G1), 0.116 (G2), 0.094 (S1), 0.078 (G3), 0.047 V_{Li} (S2). The delithiation (Fig. 28b) profile shows three plateaus for the Gr-only electrode at 0.111 (G4), 0.150 (G5), and 0.232 (G6) V_{Li}. These same three plateaus are also seen in the Si/Gr electrode data. In addition, the plateau at 0.429 V_{Li} (S3) is seen only in the Si/Gr electrode data. Plateaus S2 and S3 have been attributed to the crystallization of amorphous Li_xSi_y to Li₁₅Si₄ below ~ 50 mV during lithiation and its subsequent delithiation above ~ 400 mV, respectively. The plateau S1 likely arises from structural changes in the (amorphous) Si component that continue during the change in graphite potential from the plateau G2 to G3.

XRD data collected during the electrochemical cycling are presented in Figure 28c and 28d. Given that the strongest diffraction peaks belonging to the (001) family of planes of the Li-Gr intercalation system occur within the range 3.2-3.8 Å, only this region is presented. It is worth noting that no spectral peaks were observed that could be attributed to a crystalline phase of Si; this observation is in agreement with prior research, which indicates that the crystalline Si becomes X-ray amorphous after the initial lithiation. The Gr electrode data (Figure 1c) shows the following: (i) The average d-spacing increases in the early stages of lithiation prior to the G2 point. (ii) At the onset of plateaus G1 and G2, the diffraction peak broadens indicating the appearance of additional phases with intermediate spectral features. (iii) Between the G2 and G3 points, a Bragg peak centered at 3.54 Å is observed; the position of this peak does not change between the plateaus. (iv) Past the G3 point, in addition to this 3.54 Å peak, a new peak at 3.70 Å emerges. From these observations, we conclude that at least five ordered phases (known as the lithiation stages) are formed during Li intercalation between the graphene layers in the graphite. These same phases are also observed during Gr delithiation (Figure 1c). The similarity between the stages observed during Gr lithiation and delithiation is consistent with the well-known reversible nature of Li⁺ ion intercalation into graphite. As lithiation progresses the sequential formation of dilute stage I (denoted I'), stage IV/III, stage III, stage II, and stage I has been reported. Of these stages, the stoichiometry of stages II and I has been determined as LiC₁₂, and LiC₆; ambiguity exists as to the exact stoichiometry of the other three stages. In our analysis below we assume the following stoichiometries: stage I' (Li_xC₆, 0 < x < 0.1), stage IV/III (Li_xC₆, 0.1 < x < 0.22, represented by LiC₃₀), and stage III (LiC₁₈).

A custom computer code was written to deconvolute the Li_xC_y phases observed in the XRD patterns. After this deconvolution, the average Li⁺ content (i.e., capacity) of the Gr component was quantified from the XRD peak intensities. For the Si-Gr electrode, the lithium content of the Si-component was obtained by subtracting the Gr capacity from the total cell capacity; the results are as portrayed in Figure 2. Figure 2a shows that during the initial lithiation (region 1, 1.0 – 0.20 V_{Li}), Li mainly alloys with the Si; the lithiation ratio Li_{Si}/Li_{Gr} of Si vs. Gr is 0.96/0.04 in this range. That is, when the electrode capacity during lithiation is 1.5 mAh, the capacity of the Si and Gr components are ~ 1.44 mAh and ~ 0.06 mAh, respectively. In region 2, the relative fraction of Gr lithiation increases as the electrode potential decreases to 0.20 V_{Li}, below which most of the Gr lithiation is expected. In this region (0.01 – 0.2 V_{Li}), the average Li_{Si}/Li_{Gr} is $\sim 0.58/0.42$; i.e., the lithiation of Si occurs preferentially over Gr even in this region. During the initial delithiation (region 3, 0.01 – 0.22 V_{Li}), almost all Li⁺ ions are extracted from Gr, and the Li_{Si}/Li_{Gr} ratio is zero. In region 4, almost all Li⁺ ions are extracted from Si, and in this region (0.22 – 1.0 V_{Li}) the Li_{Si}/Li_{Gr} ratio is $\sim 0.97/0.03$.

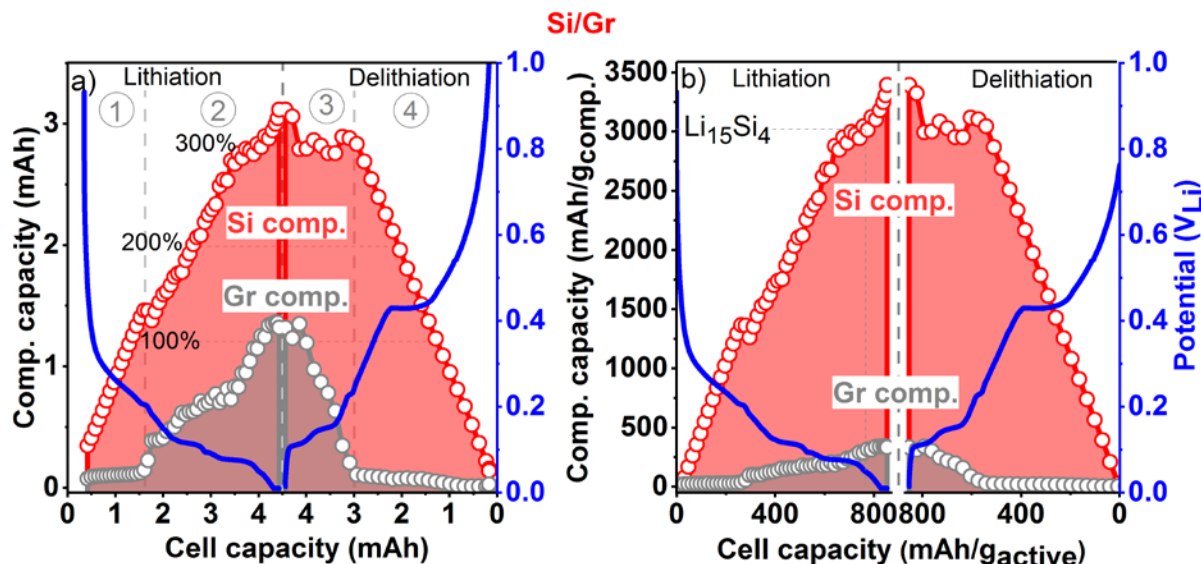


Figure 29. Capacity (a) and specific capacity (b) of the Gr and Si components in a Si-Gr electrode during lithiation and delithiation. Note that the capacity increases during lithiation and decreases during delithiation. Regions 1 to 4 are indicated with the circled numerals in panel a. The percentages shown in panel (a) are the estimated expansions of Si particles.

These results indicate that delithiation of the Si-Gr electrode occurs sequentially, first from the Gr and then from the Si. This behavior has practical implications for electrode cycling. Figure 29b shows the specific capacity in the *individual* components plotted as a function of the *net* specific capacity. When the potential reaches $0.2 V_{Li}$ during lithiation, the specific capacity in the Gr is negligible, whereas for the Si particles it is $\sim 1350 \text{ mAh}\cdot\text{g}^{-1}_{Si}$, which corresponds to a volume expansion of 135 % (assuming a linear expansion rate of 100% per $1000 \text{ mAh}\cdot\text{g}^{-1}_{Si}$). When the potential is $0.01 V_{Li}$ during lithiation, the specific capacity of the Gr is $\sim 340 \text{ mAh}\cdot\text{g}^{-1}_{Gr}$, whereas for the Si particles it is $\sim 3400 \text{ mAh}\cdot\text{g}^{-1}_{Si}$, which corresponds to a volume expansion of 340 %. On delithiation, the Si particles remain at ~ 340 % expansion until the electrode potential reaches $0.20 V_{Li}$ since Li^+ ions are extracted only from the Gr particles in the $0.01\text{--}0.2 V_{Li}$ range. The Si particles begin to contract only when the potential is in the $0.2\text{--}1.0 V_{Li}$ range. Previous research has shown that volumetric changes in the Si particles during electrochemical cycling greatly accelerate capacity fade. With that in mind, Figure 29b can be used to design cycling regimes to minimize such changes by avoiding the formation of the expanded $Li_{15}Si_4$ phase, in this way extending the cycle life of the cell. Note, that the plots in Figure 29b will be affected by the Si content, which will alter capacity contributions of the Gr and Si components.

Calendar-life versus Cycle-life aging of Lithium-ion Cells with Silicon-Graphite Composite Electrodes

Potential profiles for the positive electrode from a NCM523/Si-Gr (10 wt% FEC) cell that underwent cycle-life aging is shown in Fig. 30a and from a similar cell that underwent calendar-life aging is shown in Fig. 30b. The negative electrode potential is simply the difference between the cell voltage and positive potential at any given instant. For example, cycle 2 in Fig. 30a indicates that the positive potential changes from 3.68 V to 4.22 V (as a result of oxide delithiation), when the cell is charged from 3.0 to 4.1 V; the negative potential correspondingly changes from 0.68 V to 0.12 V (indicating lithiation of the Si-Gr electrode). The reverse process happens during cell discharge from 4.1 to 3.0 V; the positive potential changes from 4.22 V to 3.68 V (as a result of oxide lithiation), and the negative potential correspondingly changes from 0.12 V to 0.68 V (indicating delithiation of the Si-Gr electrode).

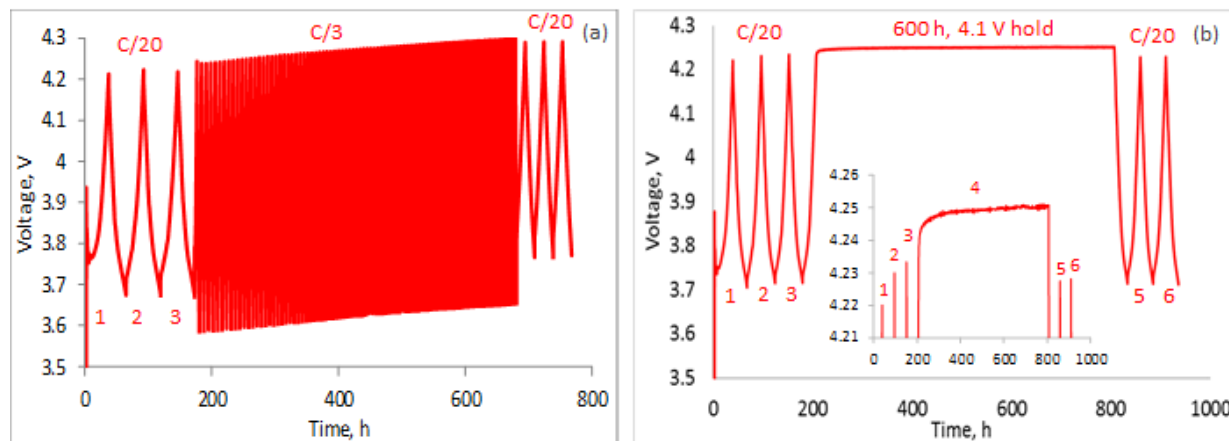


Figure 30. Changes in the positive electrode potential during (a) cycle-life aging and (b) calendar-life aging of a NCM523/Si-Gr (10 wt% FEC) cell. The inset in (b) shows the top 50 mV of the plot. In both plots, the first 3 (formation) cycles are at a $\sim C/20$ rate. In (a), cycles 4-97 (aging) are at a $\sim C/3$ rate and cycles 98-100 are at a $C/20$ rate. In (b), cycle 4 includes a 600 h hold after charging to 4.1 V; the cycle 4 discharge and the final diagnostic cycles 5 and 6, are at a $C/20$ rate

As the cell is cycled, the positive potentials at the end of charge and discharge gradually increase over the 100 cycles, and the cycling window narrows. For example, when the cell is charged from 3.0 to 4.1 V at cycle 99, the positive potential changes from 3.77 V to 4.29 V (Fig. 30a). The higher upper potential (4.29 V vs. 4.22 V at cycle 2) indicates increasing delithiation of the oxide during cycling and the narrower cycling window (0.52 V vs. 0.54 V at cycle 2) indicates ongoing capacity loss. The observed changes can be obtained by the electrode potential shifts (known as “voltage slippage”) that occur during cell cycling. This slippage, results from a net loss of mobile Li^+ ions, as they become incorporated into the solid electrode phase (SEI) of the Si-Gr negative electrode. The capacity loss (cycle 99-cycle 2, $C/20$ rate) for the cell is $\sim 44\%$.

For the calendar-life test cell, electrode potential changes during the formation cycles are similar to that of the cycle-life cell, as expected. During the potentiostatic hold the positive electrode potential of this cell also increases, indicating increasing delithiation of the oxide (Fig. 30b). However, after the potentiostatic hold, the positive potentials at the end of charge and discharge are *slightly lower* than those before the hold. For example, the highest potential for cycle 5 is 4.227 V vs. 4.233 V for cycle 3; the lowest potential for cycle 5 is 3.714 V vs. 3.716 V for cycle 3. The capacity change during the 600 h potentiostatic hold was obtained through measurements of small parasitic currents, flowing through the cell: in Fig. 30b, 11.1 mAh/g_{oxide} charge was transferred between the electrodes during the 600 h potentiostatic hold.

A possible explanation for the observation in Fig. 30b is as follows: additional sites for Li^+ ion insertion in the negative electrode become available during the potentiostatic hold. These “higher impedance” sites, presumably in the silicon, are not accessible during typical charging, even at a $C/20$ rate. Lithiation of these “additional” sites lead to increased delithiation of the oxide resulting in a higher potential at the positive electrode. However, SEI formation would also be expected at these newer sites, leading to some irreversible loss of Li^+ ions. The measured capacity loss of cycle 4 (4.5 mAh/g) is the difference between the additional charge from accessing new sites and the charge consumed during SEI formation. The lower positive electrode potential during the fourth discharge results from the insertion of an additional charge into the oxide particles.

The mole fractions of the PO_2F_2^- anion were determined for various electrolyte samples. This anion forms because the electrolyte salt LiPF_6 is hydrolytically unstable and reacts with the water contained in the LiPAA binder. As expected, no detectable PO_2F_2^- was observed in the freshly prepared electrolytes. For the cell after three formation cycles, the mole fraction of PO_2F_2^- anions in solution was low, ca. 2%. After cycle-life aging,

this fraction increased to 6%. For the calendar-life aged cell (which was held at 4.1 V for 600 h) this PO_2F_2^- fraction was considerably higher, ca. 25%. When the FEC electrolyte was simply put in contact with the electrode (no cycling) for 130 h (equivalent to time for formation cycles), the PO_2F_2^- mole fraction was 11%. This value is considerably *higher* than the fraction in the cycle-life aged cells but *lower* than in the calendar-life aged cells.

These data indicate that the extent of LiPF_6 hydrolysis in the electrolyte is ~ 4 times greater for calendar-life cells than for the cycle-life cells; that is, the chemical evolution of the electrolyte is different during calendar-life aging than during cycle-life aging. We propose the following explanation for the observations. When the Si-Gr cell is cycled and particle volumes change, the SEI becomes unstable, so HF can access and reacts with the surface. These reactions decrease the concentration of HF in the electrolyte. In contrast, during the potentiostatic hold, the SEI is not restructured so both water and HF can access the surface of the lithiated Si particles only slowly (by diffusion through the “static” SEI). Consequently, water has no reaction sink other than LiPF_6 hydrolysis; this is why the LiPF_6 hydrolysis becomes so efficient. However, even during the potential hold, some HF can reach the Li_xSi particle surface, where it corrodes the protective layer causing electrolyte reduction and the small ($\sim 3\%$) capacity fade mentioned above.

Conclusions: Silicon-based Electrodes

Operando energy dispersive XRD was conducted on 2032-type coin cells to monitor the evolution of the Gr-component in a composite Si/Gr (15/73, w/w) electrode during lithiation/delithiation cycling. Deconvolution of the Gr peaks combined with quantitative XRD analysis allowed us to monitor of the (de)lithiation fraction in each active component. The lithiation begins with Li^+ ion storage mainly in Si; the Gr intercalates Li^+ ions only at potentials < 0.20 V. In the 0.20–0.01 V range, the relative lithiation of Si and Gr are $\sim 58\%$ and 42% , respectively. On delithiation, Li^+ extraction occurs mainly from Gr in the 0.01–0.23 V range (region 3) and from Si in the $> 0.23 - 1.50$ V range; that is, the delithiation current is carried sequentially, first by graphite and then by silicon. This type of information can be used for the rational selection of electrochemical cycling windows that limits volumetric expansion in Si particles and thereby extending cell life.

The calendar-life and cycle aging behavior of several cells with a NCM523-based positive electrode and a Si-containing (or a Gr-based) negative electrode were compared. The cells contained the baseline Gen2 electrolyte (1.2 M LiPF_6 in EC:EMC 3:7 w/w) with or without 10 wt% FEC. Our data indicated that the capacity fade was greater for the cycle-life tests than for the calendar life tests. The fade mainly results from immobilization of Li^+ ions in the negative electrode SEI. Furthermore, a small parasitic current flow was observed in the cell during the potentiostatic hold; after ~ 100 h, the current flow was infrequent, indicating an SEI that is passivating for most of the time. However, periods of cell activity seen as random bursts of current flow indicate some charge loss to the SEI. Electrolytes harvested from the cycle aged and calendar aged cells were examined. Our data showed that the concentration of LiPF_6 hydrolysis products (PO_2F_2^- anion, specifically) was significantly greater in the electrolyte from the calendar-life cells. Also, electrolytes that were simply in contact with the electrode (no cycling) showed significant amounts of the PO_2F_2^- anion, indicating that the Si-Gr electrodes are a source of water in the cell (even though they are dried at 150°C in a vacuum oven). The HF generated during LiPF_6 hydrolysis can diffuse through the SEI and react with the Si particle surfaces. Such corrosion is more likely during cycle-life aging (which causes continuous restructuring of the SEI) than during calendar-life aging (wherein the SEI slows down, but does not prevent, HF access to the particle surfaces).

Developing an understanding of how the lithiated Si species within the electrode interacts with their environment is critical to the SEI layer formation and the cyclability of the Si electrodes. We have synthesized and scaled up lithium silicides model compounds that represent the silicon electrode at various states of charge, and used MAS-NMR and X-ray diffraction to assess the stability of different battery components, including binders and electrolyte solvents, in contact with the highly-reactive lithiated Si electrodes. NMR results showed that the contacting between PVDF and LS would cause the breaking of C-C and C-H bonds in PVDF, formation H_2 gas and lithium complexes, leading to the degradation of PVDF and the final failure of Si

anodes. Several potential reaction mechanisms between PVDF and Li_7Si_3 were proposed. In comparison, LiPAA showed good chemical stability in contact with the LS model compounds, implying it can be a better binder material for Si anode. In addition, the quantification study of the reactivity of Li_7Si_3 vs. carbonates (EC, EMC and FEC) and triglyme showed that exposure Li_7Si_3 to triglyme or FEC induced the least structural and chemical changes, whereas the reactions with EMC and EC are more pronounced. However, triglyme and FEC become much more reactive after mixed with the more deeply lithiated model compound $\text{Li}_{21}\text{Si}_5$. Triglyme-based electrolytes were prepared and showed much higher initial capacity, outperformed the baseline by 75%. However, electrochemistry results suggest that interface passivation for the triglyme-based electrolytes is inadequate and cell performances decay rapidly.

Analysis of the electrodes via Raman Spectroscopy indicated that issues associated with homogeneity and electronic isolation exist as different parts of the electrode were found to have different levels of lithiation after cycling. Utilization of copper nanoparticles electrodeposited on the surface was identified as a method to increase the sensitivity of Raman Spectroscopy signal by the SERS effect with minimal chance of introducing new materials or altering the SEI deposition. Unfortunately, the enhancement associated with the Cu-coated electrodes was not significant enough to identify additional species.

The generation and consumption of gas in these slurries is, for the most part, a direct result of Si oxidation during slurry preparation. Furthermore, solvent contribution alone is not the limiting factor rather the addition of Carbon Black (CB) played a role in promoting the oxidation of the Si particles. Based on gassing results of the NanaAmor Si particles from the water slurries, the samples containing carbon black suffered the greatest amount of oxidation confirming CB is a key reagent. The CB-samples may be producing more gas as their was additional evidence that the CB containing samples had more CO_2 in the gas stream. We believe the CB acts as a high surface area catalytic site in which a proton coupled, charge transfer could take place. Both OH and H^+ readily diffuse through amorphous SiO_x . Despite the acidic environment, the natural dissociation of water provides sufficient OH⁻ ions, which could diffuse through the amorphous SiO_x and oxidize the Si core. In this proposed scenario the CB lowers the activation energy needed to reduce the protons, which may not take place on the SiO_x surface alone.

3 Silicon Surface Modifications

Silane-based Surface Modifications

The chemical and electrochemical reaction on the surface of the silicon (Si) and lithiated silicon (Li_xSi) with electrolyte solvent/additive plays a significant role in the battery performance of silicon anode. The non-volatile reaction products deposit on the particle and form the so-called solid-electrolyte-interface (SEI). For the traditional graphite-based anode, this exclusively Li^+ -conducting SEI layer passivates the surface of the lithiated graphite and prevents the further reactions with electrolyte thus enables the reversible lithiation / delithiation chemistry of lithium ion battery. However, due to the huge volume expansion/contraction of silicon-based anode, the surface passivation is not established since the SEI cracks and reforms with cycling which consumes considerable amount of active lithium resource from the cathode leading to the rapid capacity decay.

The overall goal of this project is to develop sustainable high-energy density of Si-based nanocomposite electrodes for electric vehicle application. Specifically, in this work, we try to engineer the Si surface chemistry through different approaches with a target to stabilize the interface affording a Si anode with extended cycle life. The first approach is to develop new electrolyte/additive that could chemically / electrochemically decomposes and deposits on the lithiated Si surface forming a resilient SEI layer that stabilizes the interfacial reactivity of Li_xSi and electrolyte. Fundamental understanding of how the reactivity of electrolyte/additive with Si anode and how the chemical composition of SEI affects the cell performance will be systematically performed. The second approach is to functionalize the surface of Si particles through organic silane chemistry with a target to stabilize the interface affording a Si anode with extended cycle life.

A two-step approach was employed to introduce the epoxy group to the surface of commercial silicon nanoparticles. The SiNPs were first treated by hydrogen peroxide (H_2O_2) to enrich the surface silanol (Si-OH) group followed by a surface hydrolysis/condensation reaction with the epoxy-containing silane precursor. For comparison, methylsilane surface-modified SiNPs were also synthesized by the same procedure and the impact on the cycling performance was directly compared in coin cell tests. Post-test analysis included Fourier-transform infrared spectroscopy (FT-IR), X-ray photoelectron spectroscopy (XPS), thermogravimetric analysis (TGA), and scanning electron microscopy/energy-dispersion X-ray spectroscopy (SEM/EDX). The results shed light on the source of the improved electrochemical performance of the epoxy-functionalized SiNPs anode materials.

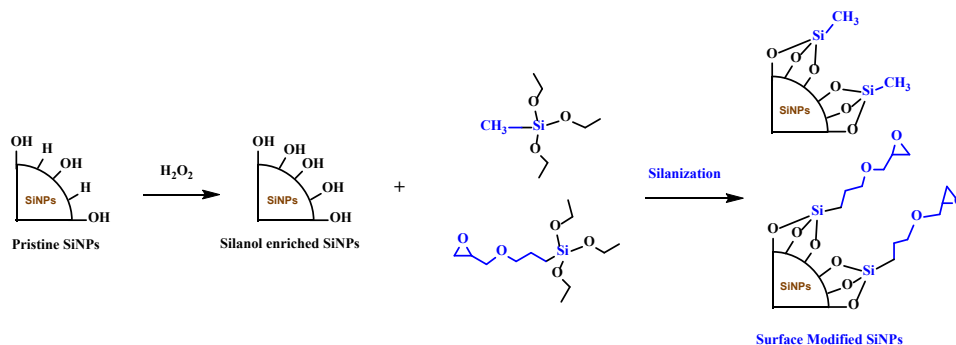


Figure 31.. Synthesis of surface-functionalized SiNPs with methyl and epoxy terminal groups.

Figure 31 outlines the synthesis route for the surface-functionalized silicon nanoparticles. Commercial SiNPs were first treated by hydrogen peroxide solution to convert Si-H and Si-O-Si groups to silanol (-Si-OH) group following a literature procedure. The Si-OH SiNPs are subject to surface hydrolysis/condensation reaction with glycidylpropyltriethoxysilane. The pristine SiNPs showed a broad peak at 1100 cm^{-1} (expands from 1000 cm^{-1} to 1250 cm^{-1}) in the FT-IR spectrum (Figure 1a), which is a typical stretching vibration peak for the Si-O-Si bond and indicates the existence of a native SiO_x layer on the pristine SiNPs. [24] After the hydrogen peroxide treatment, the increase in Si-OH peak intensity ($\sim 3300\text{ cm}^{-1}$) indicates that more silanol group was generated on the surface of the pristine SiNPs [25] and confirms the successful enrichment of surface silanol group. During the synthesis of epoxy-terminated SiNPs, a hydrolysis and condensation reaction formed a new Si-O-Si bond on the surface of the particle. The FT-IR spectrum of epoxy-SiNPs is also shown in Figure 32a. The band at $1250\text{-}1500\text{ cm}^{-1}$ originated from the ring expansion or breathing of the epoxy ring [26-28] and typical C-H vibration bands of the alkyl group appear at 2923 cm^{-1} and 2880 cm^{-1} . The TGA data further confirmed the successful attachment of the epoxy group. As shown in Figure 32b, negligible weight loss (0.3%) was observed for the pristine SiNPs. However, this value increased to 3.2% for the epoxy-SiNPs.

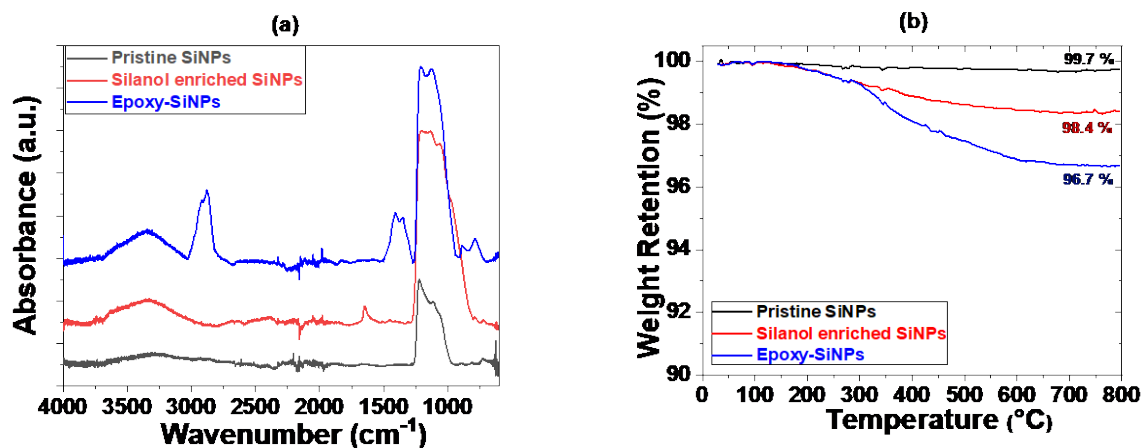


Figure 32. (a) FT-IR spectra and (b) TGA thermograms of pristine SiNPs, silanol-enriched SiNPs, and epoxy-SiNPs.

To determine the electrochemical performance, Si electrodes were coated with pristine SiNPs, CH₃-SiNPs, and epoxy-SiNPs as active anode materials. After three C/20 formation cycles, the Si/Li cells were operated for 100 cycles at a C/3 rate. Cell capacity and Coulombic efficiency for three formation cycles at C/20 rate are shown in Figure 33a, and the cycling performance for one 100 cycles at the C/3 rate is shown in Figure 33b. The pristine SiNPs electrode shows an initial delithiation capacity of 1989 mAh/g and an average capacity 1890 mAh/g for 100 cycles. Both values for the epoxy-SiNPs electrode are much higher (initial capacity of 2294 mAh/g and average capacity of 2169 mAh/g) than those for the pristine anode. Surprisingly, the CH₃-SiNPs electrode exhibited rapid fade in capacity with increasing cycle number (initial capacity of 1976 mAh/g and average capacity of 1212 mAh/g) (Figure 2b). These data clearly indicate that the functional group on the surface of the SiNPs dictates the electrochemical performance of the Si electrode. The cell performance agrees well with our initial approach of introducing epoxy group on the surface of SiNPs to promote the integration of active particles with the binder, current collector, and other cell components. To further verify this positive impact, the chemical reaction between the epoxy-SiNPs and PAA binder was examined by mixing the SiNPs and PAA binder with the same composition used in the anode slurry and stirring at room temperature for overnight. The reacted SiNPs were isolated by high-speed centrifugation and subjected to TGA analysis. For the CH₃-SiNP particles, the TGA profiles are almost identical before and after the reaction with PAA binder (data not shown); nevertheless, an additional weight loss was observed for the PAA treated epoxy-SiNPs. This indicates that PAA segments were attached to the surface of the epoxy-SiNPs particles via the ring-opening addition reaction of the epoxy group with the hydroxyl group from the PAA binder.

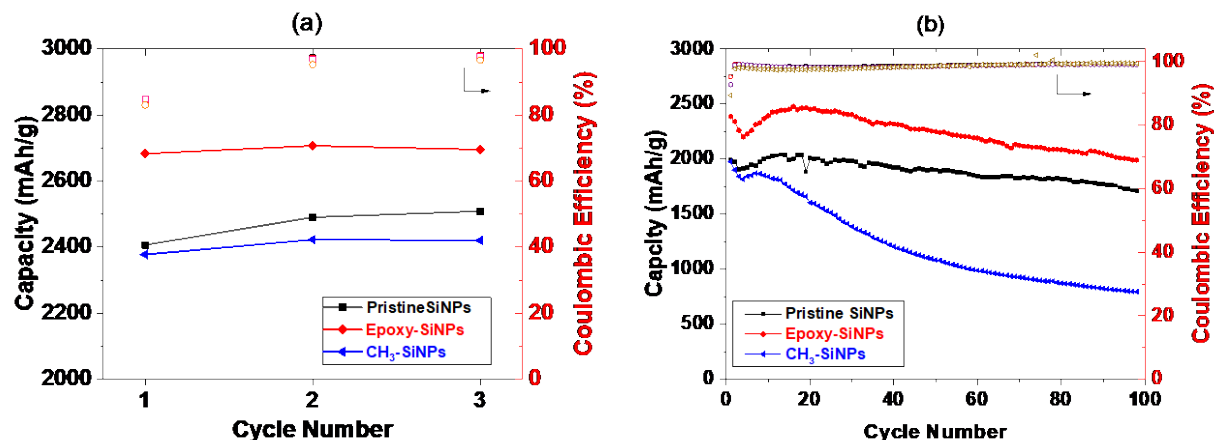


Figure 33. Initial capacity and Coulombic efficiency of Si/Li cells: (a) three C/20 formation cycles and (b) one-hundred C/3 cycles.

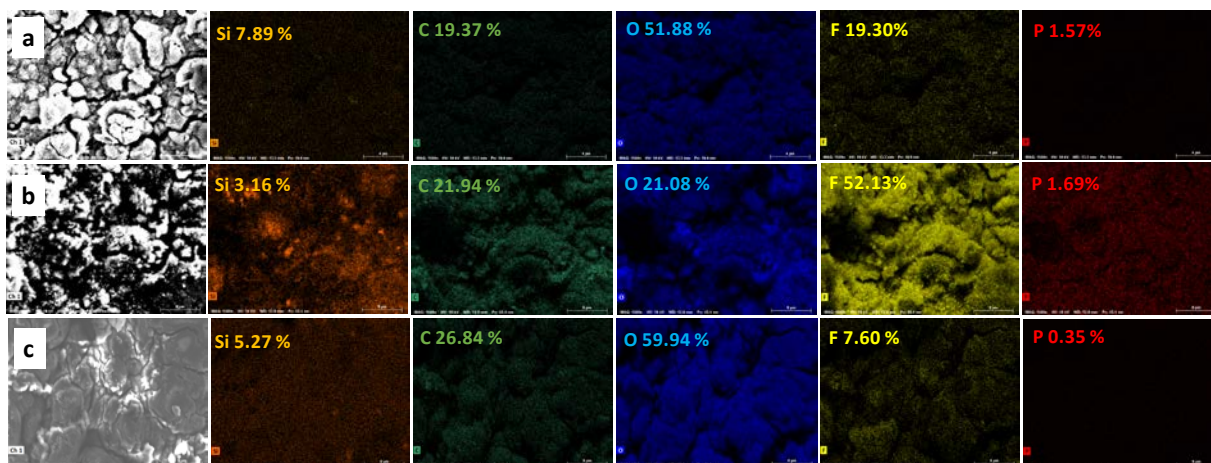


Figure 34. EDX elemental mapping (Si, C, O, F, P) for Si/PAA electrodes with (a) pristine SiNPs, (b) Si-OH SiNPs and (c) epoxy-SiNPs after 100 cycles.

Figure 34 shows the surface chemical composition of the cycled electrodes: pristine SiNPs, Si-OH SiNPs, and epoxy-SiNPs. For all three electrodes, the detectable surface Si amount decreased, indicating the formation of a thick SEI layer. Fluorine and phosphate were detected from the surface of all three cycled electrodes due to the decomposition of the electrolyte. The surface of the electrode made from epoxy-SiNPs has much less fluorine and phosphate content than that of the other two electrodes, as shown in Figure 34c. This finding suggests that the surface modification of SiNPs mitigated the continuous reduction/decomposition of the electrolyte. It is notable that the fluorine content on the surface of the electrode made from Si-OH SiNPs is much higher than that on the surfaces of the other two electrodes (Figure 34b). We speculate that the surface

silanol group tends to eliminate water via a condensation reaction during repeated cycling, leading to severe hydrolysis of the LiPF_6 electrolyte salt at the electrode surface. [29]

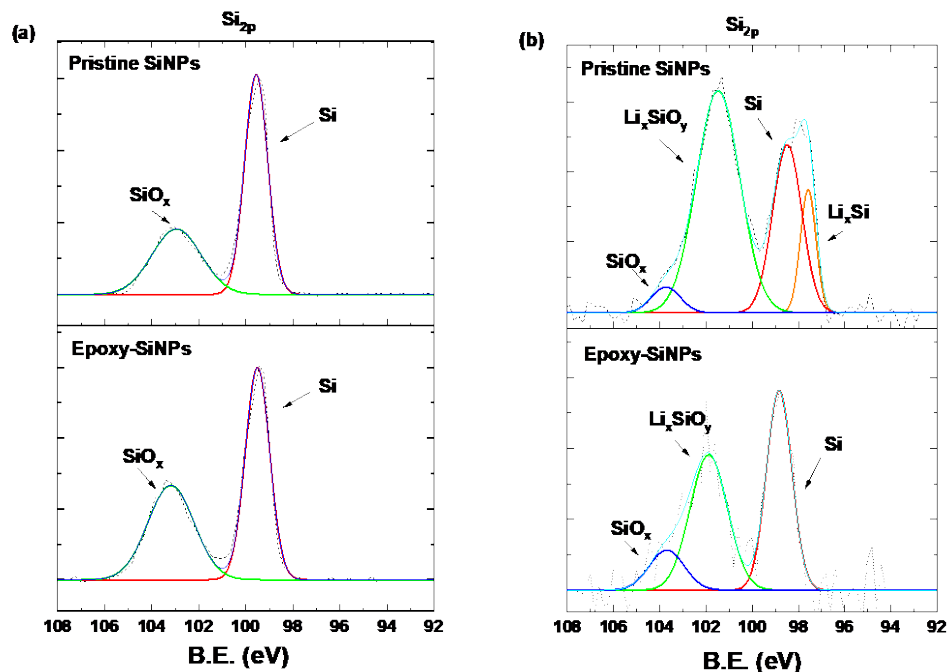


Figure 35. Si_{2p} XPS spectra of the Si electrodes based on pristine SiNPs and epoxy-SiNPs before and after one formation cycle: (a) fresh Si electrode before cycling and (b) Si electrode after one formation cycle at delithiated state.

The surface of the cycled electrodes was examined by XPS. Figure 35a show the Si_{2p} spectra of the pristine SiNPs and epoxy-SiNPs electrode before cycling. The peaks related to elemental silicon (99.4 eV) and oxidized silicon SiO_x (103.5 eV) resemble the spectra of their corresponding nanoparticles, indicating that the epoxy-SiNPs nanoparticles remain inert after exposure to the aqueous slurry. After one formation cycle, new peaks appeared in both spectra at 102 eV (Figure 35b), a characteristic peak of Li_xSiO_y formed by irreversible reduction of SiO_x at the electrode surface. [30,31] However, a lower intensity Li_xSiO_y peak was observed for the epoxy-SiNPs electrode. In addition, the presence of a new peak at a binding energy of 98 eV (Li_xSi) from the pristine SiNPs electrode implies that not all the lithium was extracted from the pristine SiNPs electrode. Without the surface group, the pristine SiNPs tends to react with the lithiated silicon causing impedance buildup and the polarization of the electrode. In contrast, the epoxy-functionalized SiNPs reduced the parasitic reactions with Li_xSi and enabled the reversible lithium insertion and extraction. Actually, the Li_xSi peak was not observed on the XPS spectrum of the epoxy-SiNPs electrode at the fully delithiation state. Surface modification of silicon nanoparticles could mitigate the irreversible reduction of SiO_x during lithiation and facilitate the extraction of lithium during delithiation. Since both Li_xSiO_y and Li_xSi species contribute to the irreversible capacity in the first lithiation/delithiation cycle, the XPS results are in good agreement with the higher initial capacity and Coulombic efficiency of the epoxy-SiNPs electrode.

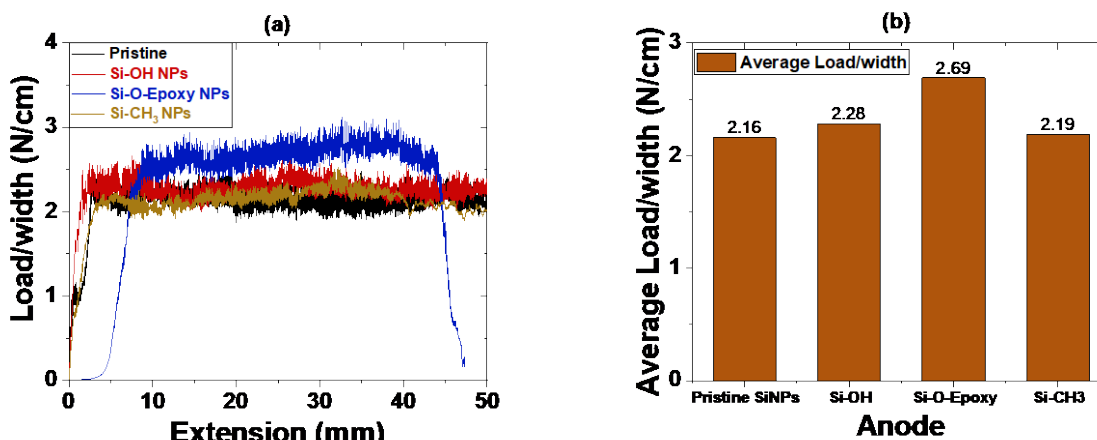


Figure 36. (a) Adhesion strength of the Si anodes with pristine SiNPs, Si-OH SiNPs, epoxy-SiNPs, and CH₃-SiNPs as active materials, and (b) summarized data of average load per unit width (N/cm).

The binding strength is critical to the electrochemical performance of the Si-based electrode since strong bonding between the active particles and the particle/current collector help maintain the electrical contacts and the integrity of the Si anode. [32] A peel test was employed to evaluate the adhesive strength of the Si/PAA anode. A continuous force was applied to the surface of the electrode and when the Si/PAA anode was peeled off of the current collector (copper foil in this case), the resulting load/width (N/cm) reflects the adhesive strength of the whole electrode. Figure 36 summarizes the test results. The epoxy-SiNPs showed the strongest adhesion among the tested three electrodes, which is attributed to the high reactivity and strong interaction of the epoxy group with hydroxyl groups from the PAA binder and the Cu current collector. This result confirms one of our initial material design ideas, i.e., introducing an epoxy group onto the surface of nanosilicon particles will maintain the electrode integrity and thus exert a positive impact on the electrochemical performance.

Characterization of Silane-based Coatings on Silicon

The project aims to develop a systematic understanding and synthesis of surface coating materials to chemically or physically change the surface of the silicon (Si) materials, in order to manipulate the interphase chemistry for enhanced electrochemical reversibility and mechanical integration in Si-based electrodes. Continuous decomposition of electrolyte on the silicon surface is one of the factors dictating the electrochemical performances of Si electrode. Tremendous efforts have been dedicated in our collaborative project to stabilizing the surface: (i) depositing an artificial protective layer by using atomic layer deposition (ALD) or molecular layer deposition (MLD), (ii) using a polymeric binder that mitigates electrolyte decomposition, and (iii) introducing electrolyte additives that sacrificially decompose to generate a protective film. To study the fundamental roles of the surface species on the electrochemical and physical properties of the electrodes, we devoted FY 18 research to develop the liquid-phase deposition process to functionalize the silicon surface. The liquid-phase deposition are capable to explore various functional groups and can be applied for both laminated electrodes and the nanoparticles. The in-depth understanding from these studies will help establish effective mitigation to address the key challenges in Si-based electrodes; and develop strategies to deploy high-energy silicon alloys and composite electrode configurations in the full Li-ion cells.

Three functional groups (-CH₃, -CF₃, and -COOH), which are usually found in the functional polymer binding materials, have been selected and deposited on the surface of our Si (100) wafer electrodes by spinning coating or by directly immersing the samples into the liquid bath. The corresponding silane compounds with the selected functional groups were used as the precursors, including silanescarboxyethylsilanetriol, n-propyltriethoxysilane, and trimethoxy(3,3,3-trifluoropropyl)silane. A self-assembled molecular (SAM) film forms on the surface of the Si electrodes. The SAM film is assembled on the surface of Si wafer through the formation of the Si-O-Si bond between the silanol and the native silicon oxide on the surface of the Si wafer. The covalently attachment enhances the adhesion of the silane film on the surface of silicon, which ensures the coating effects during the electrochemical process. A variety of SAM films can be assembled by changing the functional groups in the corresponding silane compounds.

Electrochemical behavior of the surface-modified electrodes was characterized by using galvanostatic cycling tests. Figure 37 displays the voltage profiles of the functionalized Si electrodes, cycled in the Gen2 (1.2 LiPF₆ in EC: DEC 3:7) electrolyte with 10 wt% FEC additive. Each electrode was lithiated for 2 hours and delithiated up to 1.5 V (vs. Li/Li⁺) with a current density of 27.3 μA/cm². The Coulombic efficiencies (CE) of the functionalized electrodes are slightly higher than CE in the pristine electrode, -CF₃ (92.9%) > CH₃ (92.2%) > COOH (91.8%) > Pristine (90.9%). The lithiation of the crystalline Si starts below 0.1 V (vs. Li/Li⁺), which is much lower than the reduction potential of the carbonate electrolyte (>0.5 V) and the lithiation of native silicon oxide. Thus, the majority of capacity gained above 0.1 V can be attributed to the

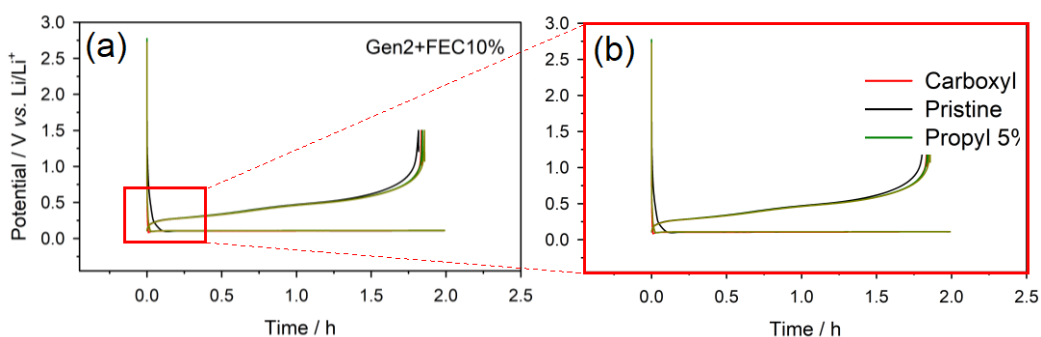


Figure 17. The voltage profiles of the functionalized electrodes. Cut-off : 2 hours lithiation, 1.5 V delithiation.
Current density : 27.3 μA/cm².

side reactions related to the interphase formation. Figure 37b shows an enlarged plot of Figure 37a. It is clearly seen that less activities were observed in the treated electrodes above 0.1 V, as compared to the pristine electrode. The behavior in the surface-treated Si electrodes is attributed to the insulating properties of the SAM layer at the top of Si electrodes; that is, the SAM layer hinders the electron transfer from the bulk to the surface of the Si electrode.

Reduction of the carbonate electrolyte and its interaction with the surface species of the Si electrodes lead to the formation of solid electrolyte interphase (SEI). Due to the different functional groups used for surface modification, distinct SEI layers could be expected for each surface-modified Si electrode. X-ray photoelectron spectroscopy (XPS) with high sensitivity to the surface species has been performed to characterize the chemical structure of the SEI on the surface-modified Si electrodes. Table 1 summarizes the composition of the surface layer, based on the XPS results. The SEI on the pristine electrode is enriched by Li and F, identified as LiF based on the binding energy of each element. As mentioned in previous sections, FEC was used in the galvanostatic testing. FEC has been known to be decomposed sacrificially prior to EC or DMC, generating LiF-rich SEI with minor ingredients of poly (VC), Li₂CO₃ and Li₂C₂O₄ on the surface.[33] As compared in Table 7, XPS data show negligible impacts of the functional groups on the

chemical composition of the interphase. It is interesting to note that the interphase formed on the treated Si electrodes are also dominated by LiF as the interphase of the pristine electrode does. Minor changes are observed in C, O, and Li spectra (not presented) especially on the surface of the CH₃-treated electrode, implying the different concentration of Li₂CO₃ or Li₂C₂O₄ in the interphase.

Table 7. Chemical composition of SEI calculated using XPS spectra.

Element	Pristine	-CH ₃	-COOH	-CF ₃
C 1s	8.8	13.9	10.5	11.2
Li 1s	35.8	34.1	35.6	35.3
F 1s	38.2	29.4	34.8	34.7
O 1s	9.6	15.7	12.9	12.3
P 2p	0.8	0.9	1.1	0.8
Si 2p	6.9	6.0	5.2	5.6

Electrochemical impedance spectroscopy (EIS) was used to evaluate the impact of the functional groups on the interfacial resistance of the Si electrodes. The Si electrodes surface-modified with different functional groups were cycled in a 3-electrode cell to measure impedance without the interference from a counter electrode. The same electrolyte, which is GEN2 with 10% FEC, was used for all of electrochemical

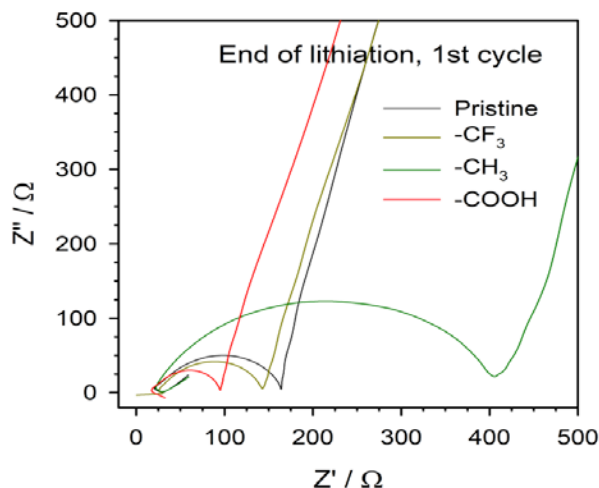


Figure 38. Impedances of the surface treated electrodes, measured at the end of lithiation.

reactions. The EIS data were collected at the end of lithiation using 3-electrode cells. In the Nyquist plot in Figure 3, the semi-circle in the high frequency region reflects the interface resistance; SEI (R_{SEI}) and charge transfer resistance (R_{ct}). The spike in the low frequency region is Warburg impedance of Li^+ diffusion in the electrochemical active material—Si electrode. Although the chemical compositions of the SEIs are comparable and dominated by LiF, the interface resistances are significantly different. The interface resistance increases in the order of $-\text{CH}_3$ (420Ω) > Pristine (180Ω) > $-\text{CF}_3$ (140Ω) > $-\text{COOH}$ (100Ω).

In Figure 38, the ionic conductivity of the Si electrodes functionalized by $-\text{CH}_3$ and $-\text{COOH}$ shows the largest and smallest values, respectively. Then, these two electrodes were selected to run the quasi in-situ EIS for further understanding the impedance evolutions during lithiation/delithiation. A representative voltage profile of Si wafer is provided in Figure 39a. EIS was conducted at the different potential, highlighted in red dots in Figure 39a. The SEI layer formed on $-\text{CH}_3$ (or $-\text{COOH}$) modified surface is denoted as SEI- CH_3 (or SEI- COOH) hereafter. In Figure 39b and c, the Nyquist plots visualize the evolution of surface resistance during 1st lithiation and delithiation. As aforementioned, the first semi-circle in Nyquist plot reflects the SEI resistance. It shows that the SEI resistances for both SEI- CH_3 and SEI- COOH shows negligible changes during lithiation and delithiation. However, the resistance of the SEI- CH_3 is about 4 times larger than that of SEI- COOH , as indicated in Figure 38, 39b and 39c. While the SEI resistance is distinctive in the Nyquist plots, the charge transfer resistance is hard to be distinguished. Charge transfer resistance is usually observed in the mid-frequency range. In our case, the charge transfer resistance is likely overlapping with either SEI resistance appeared in a higher frequency range or Warburg diffusion resistance shown in a lower frequency range.

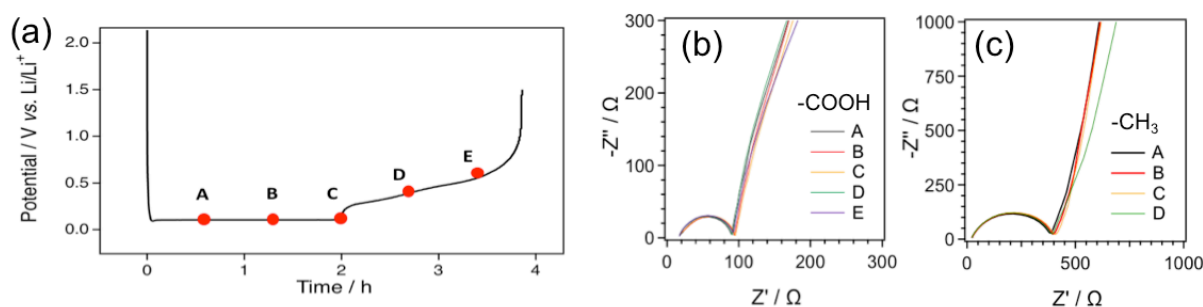


Figure 39. (a) A representative voltage profile of Si wafer electrode. (b) and (c) Nyquist plots of SEI- CH_3 and SEI- COOH . EIS measurements were conducted at specific state of lithiation and delithiation marked by the red circles in (a).

Nyquist plot has been widely used to evaluate the SEI and charge transfer resistance, without providing details about the formation process of SEI and the charge transfer reaction on electrodes' surfaces. In this study, we introduce Bode plots to compensate for the limitations inherent in Nyquist plot, provide the information about the interphase structure and formation process. Bode plots collected from both $-\text{CH}_3$ and $-\text{COOH}$ treated Si electrodes are presented in Figure 40, in which the phase angle is plotted versus frequency. Due to the frequency dependency, the Bode plots offer a better means to distinguish the individual electrochemical response that has a different time constant. The high-frequency region from $10^6 \sim 10^1$ Hz is attributed to the SEI layer. As indicated in Figure 40a, the responses for the SEI- COOH are slightly different from those found in the SEI- CH_3 . The peaks for both SEI- CH_3 and SEI- COOH locate about 10^4 Hz, which reflect the similar mobility of lithium ions in both SEI layers. As described in earlier section, LiF and Li_2CO_3 are the dominate species for both SEI- CH_3 and SEI- COOH layers, thus leading to the similar mobility for lithium ions. However, the SEI- COOH layer shows a shoulder in the higher

frequency range in the Bode plot. The shoulder in the Bode plot of SEI-COOH is related to the ionic diffusion through the -COOLi layer between the top SEI layer and the Si surface. It is known that the -COOH SAM film can be lithiated ($-\text{COOH} + \text{Li}^+ + \text{e}^- \rightarrow \text{COOLi} + \text{H}_2$) [33], resulting in the formation of the interlayer of lithium carboxylate between the Si surface and FEC-driven SEI. Regarding the -CH₃ treated electrode, a longer tail is observed in the lower frequency range, indicating a layer forming between the top SEI and the Si surface. It is believed that the functional group -CH₃ involves in the formation of the layer. However, the frequency range where the shoulder appears is higher than that for the tail in the -CH₃ treated Si. We expect that the overall lithium ion mobility would be higher in the -COOLi layer than that in the -CH₃-incorporated layer.

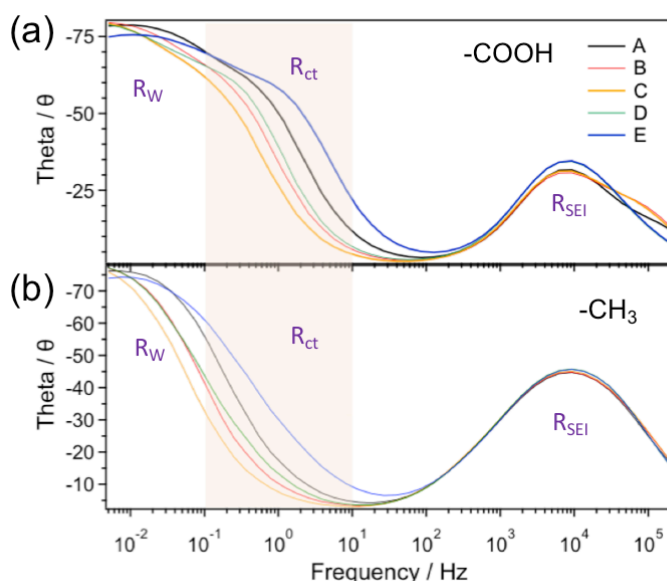


Figure 40. Bode plots of silicon electrodes fictionalized by (a) -COOH and (b) -CH₃.

Charge transfer reaction on composite Si electrode is usually seen as a separated semi-circle in Nyquist plot. But the semi-circle is overlapped with Warburg resistance for these Si wafer electrodes (Figure 4b). Here, we used Bode plot to identify the charge transfer process, considering the charge transfer process occurs in the mid-frequency range $10^1 \sim 10^{-1}$ Hz. In Figure 40a, a shoulder-like peak in the range of $10^1 \sim 10^{-1}$ Hz is observed for the SEI-COOH, especially at the beginning of lithiation (labelled as A). As the alloying reaction proceeds, the charge transfer resistance at the interphase becomes reduced (denoted C in Figure 5a). But the plateau become more noticeable at the end of delithiation—denoted as E in Figure 40a. In a strong contrast, the smooth linear Bode curve is observed for SEI-CH₃ at that frequency range, as shown in Figure 40b. It indicates that the much smaller charge transfer resistance is observed for the SEI-CH₃ layer, as compared to that of the SEI-COOH layer.

Combining the data from Nyquist and Bode plots, we found that the SEI-COOH interphase has a smaller SEI resistance (higher lithium ion mobility across the layer), but a higher charge transfer resistance than that of SEI-CH₃. It is known that the charge transfer resistance includes the lithium ion transfer at the interface between the SEI layer and the bulk Si electrode, as well as the solvation/desolvation process at

the interface between the electrolyte and the SEI layer. Due to the similar chemical composition on both SEI-CH₃ and SEI-COOH, we expect a similar solvation/desolvation process at the surface of both SEI layers. Therefore, the high charge transfer resistance, observed for the SEI-COOH, should be attributed to the lithium ion transfer at the interface between the SEI layer and the bulk Si electrode.

In addition to the lithium ion conductivity, the electronic resistivity of the interphase also plays an important role in governing electrochemical reversibility of Si electrode. The electron-insulating property of the SEI layer can block the electron transfer, then suppress parasitic reactions at the surface of the SEI layer. However, the direct measurement of the electronic resistivity is extremely challenging, majorly because of the absence of methodology for such measurements. Recently, NREL SEISTa team has developed a technique which scanning spreading resistance microscopy (SSRM) was customized to directly measure

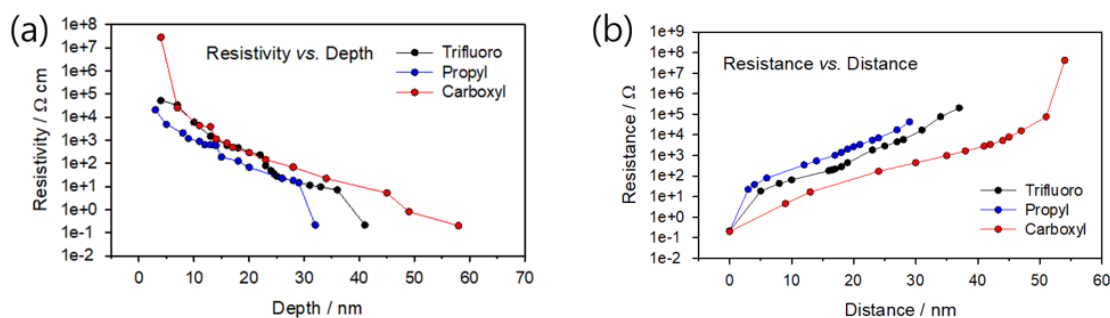


Figure 41. Surface coating effects on the electronic conductivity. Resistivity depth profile in (a) was plotted as a function of depth. All of the measurements end at the point where the resistivity reaches $\sim 10^{-1} \Omega\text{cm}$, indicating that the AFM probe has touched the bulk Si electrode. The resistance profile in (b) was calculated and plotted as a function of the distance from the bulk Si electrode.

the SEI electronic resistivity. By applying a small voltage bias between the sample and a nanoscale AFM probe, the current response will be monitored and used to calculate the electronic resistivity based on the instrument parameters and sample dimensions. The most important feature of SSRM is to provide the electronic resistance of a nanometric scale of sampling volume. By moving the AFM probe, the technique can be applied for the electronic conductivity mapping of SEI layers. Furthermore, the technique has been used to detect the evolution of the electronic resistance along the thickness of the sample, providing a depth profile of the electronic resistance. The details about the technique has been submitted. [34]

Here, SSRM was used to investigate the electronic conductivity of the SEI layers on the surface-treated Si electrodes. The resistivity/resistance from SEI-CH₃, SEI-COOH, and SEI-CF₃ (treated with trimethoxy(3,3,3-trifluoropropyl)silane) is plotted as a function of the depth—from the top of the SEI layer, and the distance from the bulk Si, as shown in Figure 41. The resistivity continuously reduces, finally reaches $\sim 10^{-1} \Omega\text{cm}$ —the resistivity of the bulk Si wafer. Therefore, the thickness of the interphase can be determined by the point at which the resistivity reaches to that of the bulk Si wafer. Resistivity, which shows the intrinsic property of the material, has also been calculated based on the formula, $R = \rho l/A$, in which R is the resistance, ρ is the resistivity, l is the length, and A is the area of the sample. The comparison of the resistance data in Figure 41a reveals that the SEI-COOH has a higher resistivity than the other surface-treated electrodes. In addition, Figure 6a indicates that the SEI-COOH layer is much thicker than those observed in the SEI-CH₃ and CH-CF₃. Furthermore, the resistance R per unit area was plotted as a function of distance from the bulk Si electrode. The interface between the bulk Si and the SEI layer was defined as ‘0’ at the x-axis. The inner sections of the SEI-CH₃ and the SEI-CF₃ layers actually is more

insulating than that of the SEI-COOH layer, while the outer section of the SEI-COOH shows the highest electronic resistance than the other two SEL layers. This peculiar growth at the latter stage of SEI formation is likely due to a chemical reaction in which electron transfer is not involved, considering the SEI resistance already reaches $\sim 10^5 \Omega$ before the sudden increase. The underlying mechanism is still not clear and require more investigation.

The results from both EIS and SSRM confirms that the SEI-COOH layer with a thickness about 60 nm has the highest ionic conductivity but the lowest electronic conductivity, as compared to the other surface-treated Si electrodes. Therefore, the -COOH terminated Si surface very likely facilitates forming a passivate SEI layer that can prevent electron transfer but allow fast ion transfer across the SEI layer. The results provide new insights on the working mechanism underlying the improved cycling performance found in the Si particle functionalized by -COOH groups and the Si electrode employing PAA or CMC binders. [35-36]

Silicon Oxide and Lithium Silicate-based Surface Modifications

In our previous work, we investigated the stability of partially oxidized silicon nanoparticles in aqueous slurries and optimized the oxide layer thickness of silicon nanoparticles for optimal electrochemical performance. However, the silicon oxide layer is electronic and ionic insulating material, which will affect the rate performance. The silicon oxide layer could also potentially cause the side reaction, which will adversely affect the coulombic efficiency.

A Li_2SiO_3 coating has been reported to be beneficial for Li-ion batteries. When such a coating is present for a $\text{LiNi}_{0.6}\text{Co}_{0.2}\text{Mn}_{0.2}\text{O}_2$ cathode, improvement in both rate and cycle performance is observed owing to the excellent ionic conductivity of Li_2SiO_3 as well as the enhanced structural stability it provides [37]. A coating containing Li_2SiO_3 has also been applied to the Si anode. The resulting material showed improved capacity retention, however, with a compromised specific capacity [38]. Nonetheless, the improved capacity retention suggests that the Li_2SiO_3 coating may improve the mechanical stability of the Si nanoparticles. In this work, we will convert the silicon oxide layer to lithium silicates and its impact on the electrochemical performance will be investigated.

Figure 42 shows the diagram for the synthesis of silicate-coated silicon nanoparticles. To obtain silicate-coated silicon nanoparticles of different silicate layer thicknesses, the Si nanoparticles with an average diameter of 80 nm were first treated at 400, 500, and 600°C in the air for 15 hours to obtain a surface oxide layer with different thicknesses. The silicon oxide thicknesses of all three samples, plus pristine Si were estimated to be 2.2, 2.8, 3.7, and 5.8 nm from low to high temperature treatment. All four Si nanoparticles were then mixed with Li_2CO_3 with a molar ratio of $n(\text{Si in SiO}_2) : n(\text{Li in Li}_2\text{CO}_3) = 1:2$, and lithium silicate formation reaction was carried out at 800°C under Ar atmosphere for 6 hours before collection for characterization



Figure 42 Diagram for the synthesis of Li_2SiO_3 -coated silicon nanoparticles

The silicate-coated Si nanoparticles were then characterized by x-ray diffraction performed at Advanced Photon Source at Argonne National Laboratory. The x-ray wavelength is 0.1173Å. Figure 43 shows the x-ray diffraction patterns of silicate-coated Si nanoparticles with different initial oxide layer thicknesses of 2.2 nm, 2.8 nm, 3.7 nm and 5.8 nm, corresponding to pristine, treated at 400°C, treated at 500°C, and treated at 600°C in air. The peaks corresponding to Si, Li_2SiO_3 and Li_4SiO_4 are labeled in the figure. A major formation of Li_2SiO_3 and a minor formation of Li_4SiO_4 are observed in all samples, which are also confirmed by the FTIR results. As the thickness of the initial oxide layer increases, the peaks corresponding to silicates also increases in intensity, suggesting the formation of thicker silicate layers with thicker initial oxide layers.

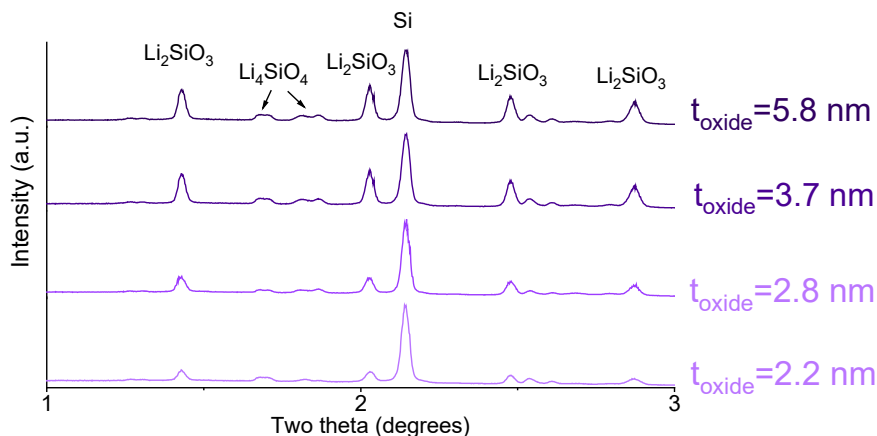


Figure 43 XRD patterns of silicate-coated Si with starting Si nanoparticles of different oxide layer thicknesses

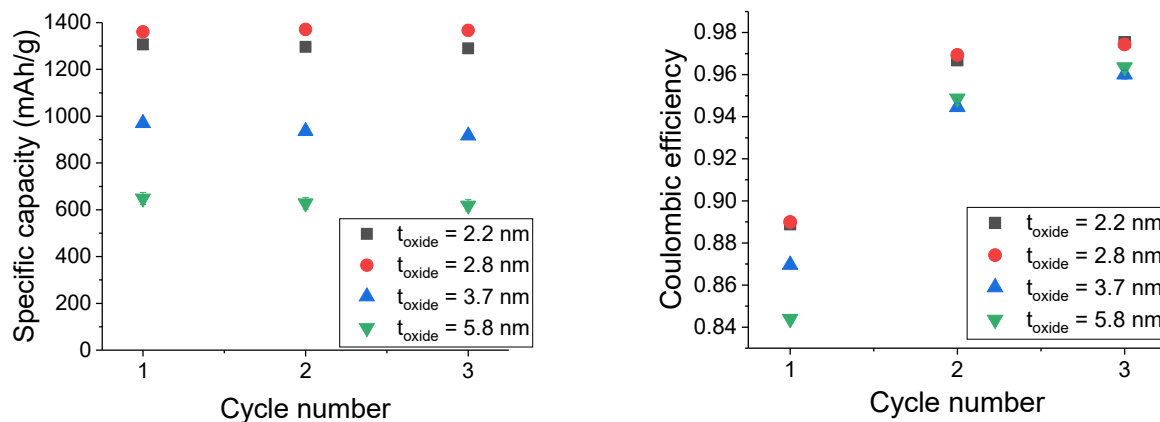


Figure 44 Electrochemical performance of formation cycles for silicate-coated Si with different silicate layer thicknesses

The silicate-coated Si nanoparticles were then fabricated into laminates with 20 wt% LiPAA and 10 wt% C45. The electrodes were then tested in half-cell configuration with Gen II electrolyte (1.2 M LiFP₆ in EC:EMC=3:7) with 10 wt% FEC. The cells underwent three formation cycles at C/10 rate between 1.5 V and 0.01 V. Figure 44 shows the electrochemical performance of formation cycles for silicate-coated Si nanoparticles with different silicate layer thicknesses. As the oxide layer increases, the capacity obtained from the electrode

decreases. Although a lower capacity (but better cycling stability) is expected for silicon nanoparticles with a thicker oxide layer, the capacity observed for all samples were lower than expected values. A likely cause of the compromised capacity is the formation of large aggregates from the solid-state reaction between Si nanoparticles and Li_2CO_3 .

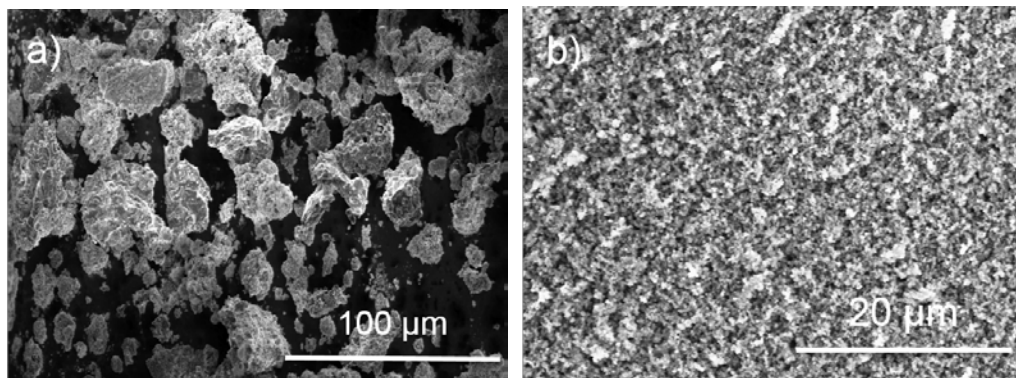


Figure 45 SEM of silicate-coated Si with starting Si nanoparticles of different oxide layer thicknesses

The silicate-coated silicon sample was then characterized by scanning electron microscopy (SEM). Figure 45a shows that large agglomerates of 50-100 μm were present after the solid-state reaction between the silicon nanoparticles and the Li_2CO_3 . The presence of such agglomerates in the electrodes may result in difficulty of accessing the active silicon material inside the agglomerates, leading to low capacity in the electrochemical testing. We then investigated the effect of high-energy ball milling at breaking up the aggregates with help from the CAMP Facility at ANL. The silicate-coated silicon sample was first milled in an air-filled zirconia container containing 20 zirconia balls (2mm in diameter) for 5 minutes at 500 rpm using a Retsch Mill, and then milled in water for another 20 minutes. The resulting milled silicate-coated silicon sample was then collected and characterized under SEM. Figure 4b shows the SEM image of the ball milled silicate-coated silicon. Unlike the silicate-coated silicon after the solid-state reaction, the ball milled silicate-coated silicon showed no major agglomerates. The dynamic light scattering also confirmed the absence of larger agglomerates, further supporting the effectiveness of high-energy ball milling to break agglomerates.

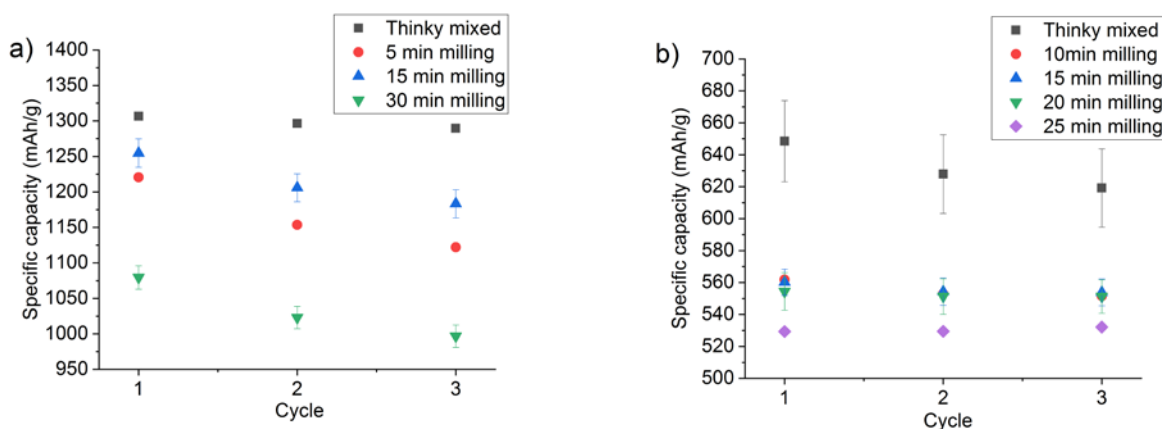


Figure 46 Electrochemical performance of formation cycles for high-energy-ball-milled silicate-coated Si with a) a thinner silicate layer and b) a thicker silicate layer.

To test the effect of high-energy ball milling on the electrochemical performance of silicate-coated silicon, silicate-coated silicon samples of two different silicate thicknesses were synthesized. The silicate-coated silicon with a thinner silicate layer was obtained from the reaction between Li_2CO_3 and Si nanoparticles with an oxide layer of 2.2 nm. The silicate-coated silicon with a thicker silicate layer was obtained from the reaction between Li_2CO_3 and Si nanoparticles with an oxide layer of 5.8 nm. To fabricate the laminates for electrochemical testing, the silicate-coated Si samples were ball-milled with 20 wt% LiPAA and 10 wt% C45 using the Retsch Mill. The laminates were coated after different milling times. The electrodes were then punched from the laminates and tested in the half-cell configuration with Gen II electrolyte (EC: EMC=3:7, 1.2 M LiPF_6) with 10 wt% FEC. For formation test, the cells underwent three cycles at C/10 rate between 1.5 V and 0.01 V. Figure 46 compares the electrochemical performance of the electrodes made using the regular Thinky Mixer and the electrodes made using the Retsch Mill. Both silicate-coated silicon with a thinner silicate layer (shown in Figure 6a) and the silicate-coated silicon with a thicker silicate layer (shown in Figure 6b) showed worsened performance with high-energy ball milling process. The worsened performance suggest that the agglomeration may not be the key factor that leads to the poor electrochemical performance of the silicate-coated silicon.

Conclusions – Silicon Surface Modifications

Surface functionalized SiNPs were designed and synthesized via a silanization reaction between functional trialkoxysilane and Si-OH-enriched SiNPs. The epoxy-functionalized SiNPs showed much improved performance compared with the pristine and methyl-substituted Si particles due to the formation of covalent bonding between the epoxy group and the hydroxyl group from the polyacrylic acid binder. Furthermore, the surface functionalization protected the parasitic reactions of the Li_xSi with electrolyte and enabled the reversible insertion and extraction of lithium with much improved initial capacity and capacity retention compared with the anode prepared with pristine Si particles. Additionally, the enhanced chemical stability of the functionalized silicon particles enabled a successful aqueous slurry making/electrode coating process with no observed gassing or foaming issues. This research provided insight that the surface functionalization on the particle level of the silicon anode is a feasible approach to mitigate the parasitic reactions of the pristine Si powder and Li_xSi with the electrolyte, tailor the formation and chemical composition of SEI, and manipulate the interaction of active material with other electrode components to enable Si anode materials in next generation lithium-ion batteries with improved electrochemical performance.

Li_2SiO_3 -coated Si nanoparticles were successfully synthesized via solid-state reaction with Li_2CO_3 . The silicate-coated Si showed compromised capacity in the initial electrochemical tests, with decreased capacity obtained with increased silicate layer thickness. A likely cause of the low capacity is the presence of aggregates due to the solid-state reaction.

The Coulombic efficiencies of the surface-coated electrodes (termination groups— $-\text{CH}_3$, $-\text{COOH}$, or $-\text{CF}_3$) are similar to the pristine un-treated Si electrode for the 1st cycle; $-\text{CF}_3$ (92.9%), CH_3 (92.2%), COOH (91.8%), Pristine (90.9%). The chemical compositions of the SEI layers are comparable based on the XPS analysis. Surprisingly, the ionic conductivity from EIS measurement and electronic conductivity obtained by using SSRM show significant differences in these treated Si electrodes. The SEI- COOH layer has much higher ionic conductivity, but lower electronic conductivity, than the other two surface-treated electrodes. This integrated functionalization and characterization approach provides a systematic methodology to investigate the effect of surface functional groups on the SEI formation, the electrochemical behavior, lithium ion conductivity, and the interfacial resistance of the Si electrode.

4 Electrode Construction

Binder Development

Electrolyte decomposition products play a critical role in the stabilization of the negative electrodes in lithium-ion batteries, as the negative electrode is operated outside the stability window of the electrolyte. The electrolyte decomposition products form insoluble SEI layer, which stabilizes the electrode and electrolyte interface. Silicon alloy material has large volume expansion and surface reactions with the electrolyte when it is electrochemically lithiated. When delithiated, the Si alloy volume shrinks and surface area also decreases. This dynamic surface change causes excessive side reactions with the electrolyte [39]. Moreover, some of the key electrolyte decomposition products are soluble in the electrolyte rather than solid precipitates [40]. Surface coatings on Si materials by organic and ceramic have demonstrated improved surface stability towards electrolytes. Nano-sizing the Si materials can successfully prevent cracking of Si material. The Si particles are assembled by a functional polymeric binder to further improve the electrode stability in a composite electrode [41].

This project is aimed to gain a comprehensive understanding of electrolyte decomposition products to SEI property relationship and understand the electrode binder's effect during electrochemical process, and to guide the design and synthesis of new electrolytes and additives and electrode binder for Si based materials. New electrolyte design with consideration of the SEI structure and functions on the Si materials can lead to enhanced Si performance over the traditional mixed carbonate based electrolyte. Both Si surface coating and functional electrode binders can enhance cyclability of the Si based composite electrode. Our recent development of an aqueous based dispersion binder can provide good point-to-point binding with the Si particle surface and allow the Si particles to expand and contract during cycling process. Surface coating on Si can prevent electrolyte interaction with the reactive surface and slow down the side reactions at the interface. Here, we propose to further reduce the Si surface reactivity by investigating electrolyte and additive functions to SEI formation and stabilization.

Designing organic molecules with preferred decomposition pathways during electrochemical process can lead to controlled SEI formation on Si surface [42]. One consideration is to vary the composition of the decomposition products to produce SEI with different flexibility to understand if a flexible SEI can be a better choice to reduce Si surface reaction. The other consideration is to strengthen the adhesion force between the decomposition products and Si materials to prevent dissolution of the electrolyte decomposition products to achieve a robust SEI layer. The bonds between the SEI layer and the Si materials need to be both strong and flexible to accommodate large volume change. Emphasis will also be on understanding the adhesion force and nature of bond between Si and organic decomposition products. This information can also be used to further development of electrode binders.

Functional binders: Pyrene (Py)-based polymers derived from 1-pyrenemethyl methacrylate (PyMA) were established as candidate electrically-conducting polymers. The flexible chain backbone of these polymers allows self-assembly of the Py side chains into ordered structures, realizing electron conductivity via the side chain π - π stacking force of the aromatic Py moieties. A versatile radical-based polymerization was used to synthesize PPyMA and also facilitated the incorporation of additional functional groups. For adhesion, we used the building block of dopamine methacrylamide (DMA) synthesized based on a literature procedure. Poly(1-pyrenemethyl methacrylate-co-dopamine methacrylamide) (PPyMADMA) was synthesized through free-radical polymerization where the adhesive monomer, DMA, accounts for 36 mol% of this copolymer (1H-nuclear magnetic resonance spectroscopy) (Figure 47a). PPyMADMA had a number-average molecular weight of 29,000 Dalton and a polydispersity index of 1.9, while being soluble in solvents such as tetrahydrofuran (THF) and N-methylpyrrolidone (NMP). The data for PPyMA in Figure 47b and 47c were shown in our previous publication,⁴ and are incorporated here for comparison. Wide-angle X-ray scattering (WAXS) results show the ordered phase characteristic of the pyrene in both PPyMA and PPyMADMA (Figure 47b). Diffraction peaks are located at $\sim 0.95 \text{ \AA}^{-1}$ and $\sim 1.02 \text{ \AA}^{-1}$, respectively. This corresponds to a lattice spacing of

~0.6 nanometers (nm). The broadening of the diffraction peak for the PPyMADMA sample indicates that the crystal grain size is smaller when copolymerized with DMA (Figure 47b).

To ensure that the newly-designed PPyMADMA binder still maintains the electronic conductivity, we studied the electronic structure of both the PPyMA and PPyMADMA polymers using synchrotron-based x-ray absorption spectroscopy (sXAS). sXAS is a direct probe of the excitations of core level electrons to the unoccupied valence states. Previous results demonstrate that sXAS is the tool-of-choice to reveal the critical electron state associated with the electric properties of polymer binder materials in batteries. The methodology is based on the principle that the lowest-energy sXAS feature directly corresponds to the state of the lowest unoccupied molecular orbital (LUMO), which defines the electric properties of the polymers.⁷ We also note that a comparative sXAS measurement between polymers with different functional groups is reliable without the core-hole potential concerns. Figure 47c shows such a comparison of the sXAS spectra of PPyMA and PPyMADMA. The splitting peaks around 285-286 eV correspond to the $\pi^*C=C$ bonds with conjugation, and the features around 288 eV are from $\pi^*C=O$.⁷ Focusing on the low-energy sXAS features corresponding to the LUMO states, it is obvious that incorporating the DMA group does not change the lowest-energy features in sXAS, indicating the LUMO of the PPyMA polymer is intact in PPyMADMA. Except for a finite change at high energies away from the LUMO states, the consistency of the overall line-shape implies that the electron states close to the Fermi level are dominated by the pyrene-based PPyMA states.

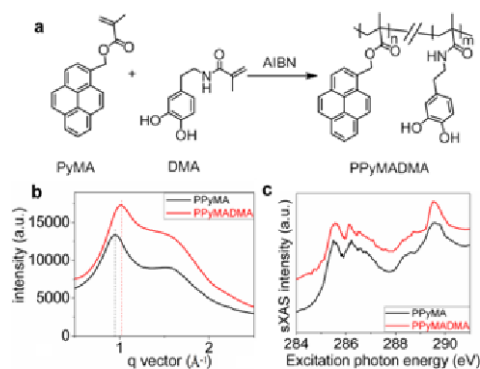


Figure 47. (a) Generic synthesis of poly(1-pyrenemethyl methacrylate-co-dopamine methacrylamide) (PPyMADMA). (b) Wide angle X-ray scattering (WAXS) of PPyMA and PPyMADMA polymers. (c) Carbon K-edge sXAS of PPyMA and PPyMADMA shows that the LUMO energy is intact in PPyMADMA, although non-conductive DMA groups are introduced.

Latex Binders: To combine the advantages of conductive polymer binders and aqueous battery electrode coating processes, a versatile emulsion polymerization method is developed to prepare conductive polymer binder emulsions in water for lithium ion battery applications. These polymer emulsions are used as-is as the binder for silicon containing anode materials. Aqueous process of conductive polymer binders has been realized for silicon containing anode materials. Emulsion polymerization methods have been developed to prepare a series of conductive polymer emulsions in water. The final binder emulsions can be used as is for slurry mixing and electrode coating without further treatment. It combines the advantages of both conductive polymer binders and aqueous process, saving energy and time while making the electrode fabrication process low-cost and environmentally friendly for silicon containing materials. Both homopolymer and copolymer emulsions in water have been synthesized and successfully been used as the binder for silicon containing anodes materials. These polymers bear different aromatic units in the polymer structure, which has shown to affect the resulting battery performance. The electrodes using these polymer emulsions as the binder show promising performance for both pure silicon and silicon/graphite composite materials. The resulting electrodes

can achieve an initial capacity of about 880 mAh/g and 75% capacity retention after 200 cycles for the electrode containing 17% silicon and 83% graphite after optimization.

In order to perform the emulsion polymerization, the monomers are normally liquid or gas. However, while the benzyl methacrylate (BzM) is a fluid liquid, the 1-naphthalenemethyl methacrylate (NaM) is a viscous liquid and the 1-anthracenemethyl methacrylate (AnM) is a solid. Therefore, BzM and NaM were used directly to produce homo-polymer emulsions (Figure 48a, P1 and P2) and AnM was dissolved in butyl methacrylate (BuM) before the reaction to finally produce co-polymer emulsions (Figure 48a, P3 ~ P8). Besides the monomers and water, surfactants with high hydrophile-lipophile balance (HLB) values were used together with CMC as the stabilizer in the reaction mixture to form a stable colloidal system. And potassium persulfate (KPS) was used as the water-borne initiator. Finally, a series of polymer emulsions in water are obtained, as shown in Figure 48b and 48c.

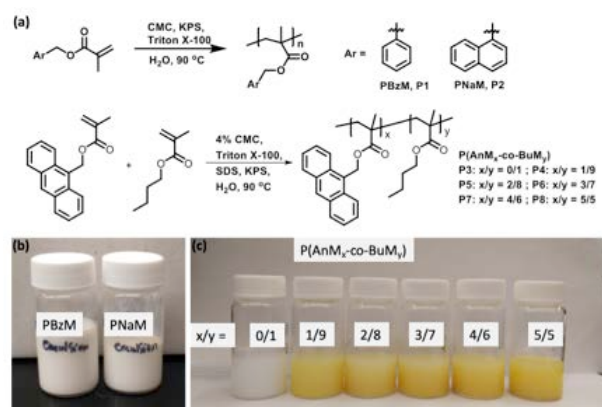


Figure 48. 1 (a) Synthetic scheme, (b, c) physical appearance of PBzM, PNaM and P(AnM_x-co-BuM_y) polymer emulsions.

New Bi-Functional Electrolyte Additives This research is aimed to gain a comprehensive understanding of electrolyte decomposition products to SEI property relationship, and to guide the design and synthesis of new

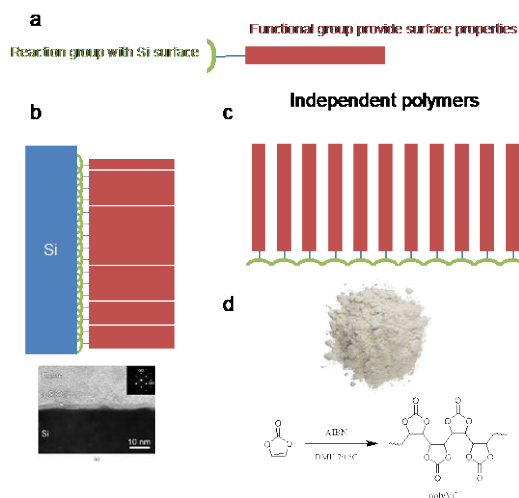


Figure 49. a. A schematic of bi-functional additives. b. Formation of surface layer on the Si surface. c. Formation of bulk polymer. d. An example of vinylenecarbonate polymerization to form polyvinylencarbonate bulk polymer.

electrolytes and additives for Si based materials. New electrolyte design with consideration of the SEI structure and functions on the Si materials can lead to enhanced Si performance over the traditional mixed carbonate based electrolyte. Designing organic molecules with preferred decomposition pathways during electrochemical process can lead to controlled SEI formation on Si surface [4]. An effort to construct a bi-functional additive toolbox is underway (Figure 49).

The bi-functional additive molecules have one reaction functional group to form coating on the surface of Si particles at low potentials, and another functional group to provide desired surface properties for the SEI layers. The reaction functional groups can also react with each other to form bulk polymer in a controlled organic chemistry environment. Figure 1d describe our previous work to synthesis bulk polyvinlylenecarbonate (PolyVC) polymer material. PolyVC can be used as binder and surface modifier for graphite based negative electrode to prevent propylene carbonate solvent molecules intercalation into the graphite layers.

Two groups of bi-functional additives have been investigated based on either a vinylencarbonate or a methacrylate reactive groups and a hydrophilic or hydrophobic functional group (Figure 50). Three new VC reactive functional additives are synthesized, and five new methacrylate reactive functional additives were identified. In the VC series (Figure 50a), the first one is MVC with an additive methyl group at the 3 position. The C8MVC has an extended hydrophobic alkyl group at the 3 position, whereas the TEGMVC has an extended hydrophilic ethyleneoxide group at the 3 position. In the methacrylate series (Figure 50b), dodecyl and butyl side chains give the additive coating a hydrophobic nature on the active materials surface, whereas, the ethyleneoxide segments side chains give the additive coating a hydrophilic nature. Both VC and methacrylate functional groups can react with the Si surface at low potential to form surface coating. The hydrophilic and hydrophobic chains can tune the properties of the either graphite or Si surface. The synthetic scheme is developed and the intermediate and final products are qualified by the ^1H NMR spectroscopy. The methacrylate series of additives results are highlight in Figure 50c,d. When the methacrylate based additives are used with graphite based electrode (Figure 50), testing results show similar coulombic efficiencies (CE) but lower capacities due to the development of resistive film on the surface of the graphite material. The CE for the graphite electrode is very high ($\sim 99.7\%$), therefore, the CE difference between the additives cannot be detected for graphite electrode. However, when the methacrylate based additives are used with Si based electrode (Figure 50d), testing results show higher CE of the ones with hydrophobic additives (DoMAA and BuMM). The higher efficiency is due to the hydrophobic effect of the coating, which tends to expel electrolyte from the active materials surface.

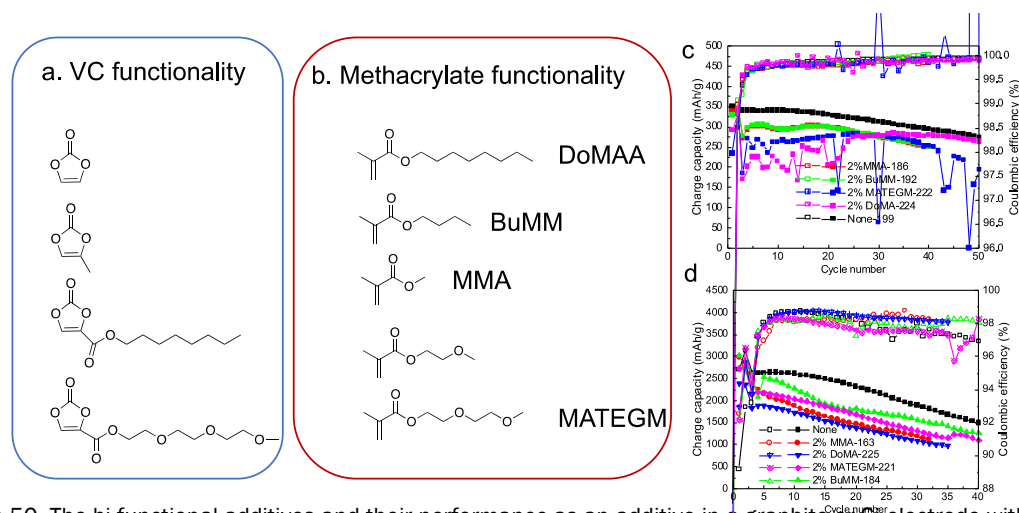


Figure 50. The bi-functional additives and their performance as an additive in a graphite or Si electrode with EC/DMC LIPF₆ electrolyte and lithium metal counter electrode. There is no FEC additive in the electrolyte. a. VC reactive functional group class of bi-functional binder. b. Methacrylate reactive functional group class of bi-functional binder. c. Graphite electrode performance with different methacrylate series of additives. d. Si electrode performance with different methacrylate series of additives.

A novel designing practice of functional conductive binders and latex binders for lithium ion batteries has been conducted. A series of conductive polymer binder emulsions in water has been prepared using emulsion polymerization methods. These polymer emulsions have been further used for lithium ion battery applications. The electrode coating process is water-based without using any organic solvents, which is lower in cost and more environmentally friendly. Using these polymer emulsions as the binder, silicon materials, solely or together with graphite materials, have been fabricated into electrodes showing promising cycling performance.

A rational design, synthesis and testing of electrolyte additives have been conducted. Two classes of bi-functional electrolyte additives with surface reaction functional group and coating functional group on one molecule have been synthesized. A toolbox is under construction with different reactive groups and hydrophobic and hydrophilic surface coating groups. The preliminary results show the surface reactive groups are able to form surface coating on the active materials, whereas the film functional groups can provide designed interaction with the electrolyte. Advanced diagnostic and full cell testing will be applied to these bi-functional electrolyte additives to further elucidate the molecular level interactions and quantify their electrochemical performances.

Polycarboxylate polymers, such as alginate, carboxymethyl cellulose (CMC) and poly(acrylic acid) (PAA), show greater promise as their functional groups form strong covalent bonds with siloxyl (SiOH) groups on the Si surface maintaining cohesion during volumetric changes. Among these polymers, PAA is particularly attractive due to a combination of excellent performance as a binder and low cost. As a matter of fact, PAA has been selected as the standard binder materials for the Silicon Deep Dive program. While PAA is becoming increasingly used, the factors controlling its performance in the LIBs are not fully understood. Meanwhile, the performance of silicon lithium-ion batteries using PAA binders is still far from meeting the requirement of practical use. Therefore, it is of paramount importance to gain in-depth understanding of the factors controlling the performance of PAA binders and evolving those binders towards improved cell performance for silicon lithium-ion batteries. In this year, we have conducted extensive efforts under those directions. **Firstly**, followed the molecular weight study,[43] another important factor, the pre-lithiation of PAA binder, has been carefully investigated and the property changes of the lithiated/non-lithiated polymer in solution, slurries, and the electrode matrix have been comprehensively characterized. **Secondly**, the re-engineered PAA binders, such as the cross-linked PAA, stiff poly(4-vinylbenzoic acid) (P4VBA), have been continuously pursued and evaluated in both half cells and full cells. **Thirdly**, initial efforts have been conducted to investigate the surface compatibility between the Si particles and binders.

Pre-lithiation of PAA binders is common practice for silicon lithium-ion batteries, which could benefit the large scale lamination process and enable the fabrication of mechanically robust electrodes. However, lithiation processes involves strong basic lithium hydroxide, LiOH, which dramatically impact the pH values of PAA polymers, consequently leading to the properties changes of the pH-responsive PAA binders and causing side reactions. For instance, the surface of the Si particles is more venerable against hydroxide under basic environment and can lead to formation of silicon oxide and generation of hydrogen. In addition, non-lithiated PAA films have been shown to have a higher tensile strength than the fully lithiated PAA films (the Young moduli were 1.4 vs. 1.0 GPa, respectively),[44] suggesting that the former material has better mechanical resistance to volumetric changes in the Si particles. Therefore, we decided to quantify the effects of lithiation on the properties the PAA polymers and the performance of silicon-graphite (Si-Gr) composite electrodes containing such binders. A composite electrode was used in this study which contained ~15 wt% Si. For fair comparison, we have standardized the preparation of the polymer, the fabrication and coating of the slurries, the thermal treatment of the electrode matrices, and the testing protocols.

Lithiated PAA samples ($M_n = 147$ kDa, PDI = 4.9) were prepared by mixing the aqueous PAA solutions with LiOH. Figure 51a gives pH of these solutions as a function of the molar ratio $x\%$ of LiOH relative to the $-CO_2H$

groups. This pH dependence is reminiscent of a strong base - weak acid titration curve. Below $x = 90\%$, the pH slowly increases from 2 to 6, which is followed by an abrupt change from 6 to 12 when x increases from 90% to 92%. As the Li^+ substitution progresses further, the pH increases from 12.0 to 12.6. The observed equivalence

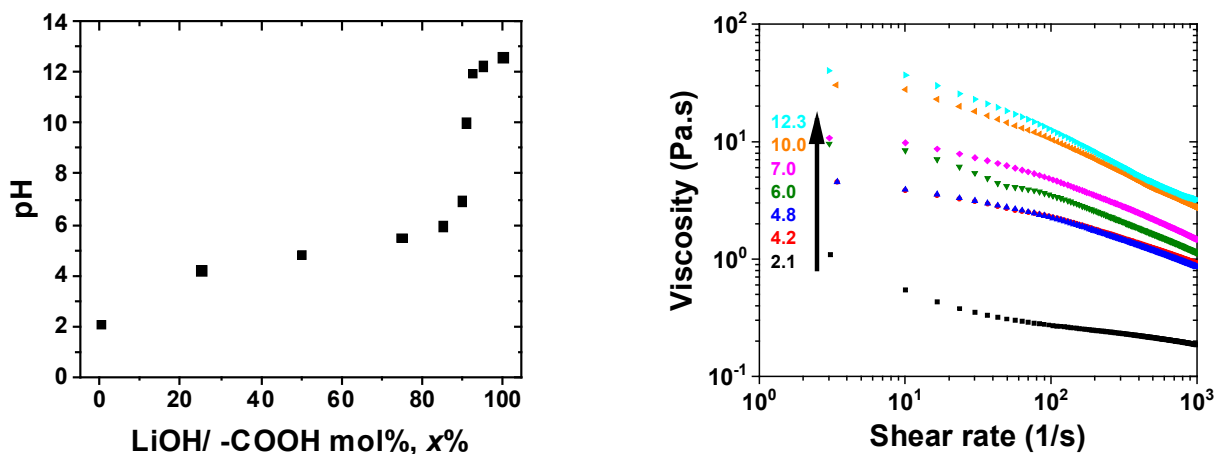


Figure 51. A plot of pH vs. LiOH/COOH molar ratio (a) and the apparent viscosity vs. the shear rate (b) for 10 wt% aqueous solutions of PAA. The pH of the aqueous solutions is color coded in panel b. Mind the logarithmic scales in panel b.

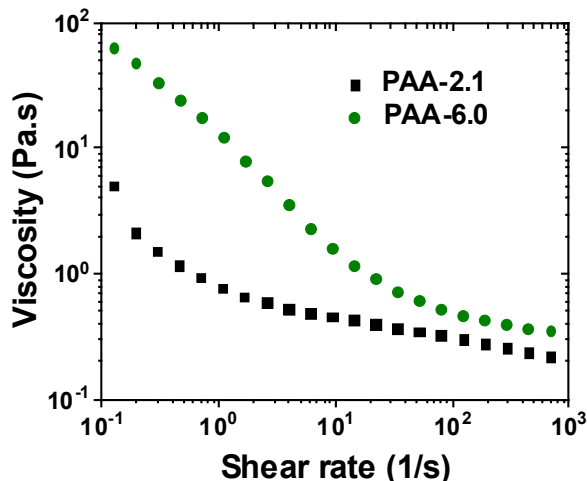


Figure 52. A viscosity plot for the PAA polymers at two pHs

point of 92% is lower than expected from the stoichiometry which we attribute to structural defects in the PAA polymer. Figure 51b shows the apparent viscosity of these polymer solutions as a function of the shear rate. As seen from this plot, the viscosity of the solution systematically increases with the lithiation, the biggest increase seen between pH 2 and 4. This increase can be attributed to tighter packing of polymer chains in coils for neutral PAA compared to ionized one. In rheology, shear thinning refers to the non-Newtonian behavior of complex fluids whose viscosity decreases under shear strain. According to the power-law model,

$$\eta(\dot{\gamma}) = K(\dot{\gamma})^{n-1} , \quad (1)$$

where η is the apparent viscosity, $\dot{\gamma}$ is the shear rate, K is the consistency index, and n is the flow index. The fluid is pseudoplastic (shear thinning) when $n < 1$, and a smaller n indicates stronger shear thinning. The parameters in eq. 1 were determined by fitting the apparent viscosity in the shear rate range of $10^2 - 10^3 \text{ s}^{-1}$. It is seen that n decreases from ~ 0.83 at $\text{pH} = 2.1$ to ~ 0.40 for $\text{pH} 12.3$, indicating that the lithiation increases shear thinning effect. Rheology data in Figure 52 indicate that aqueous Si-Gr slurries formulated using PAA polymers in Figure 51b also exhibit shear thinning, and the viscosities of these slurries remain in the acceptable range for

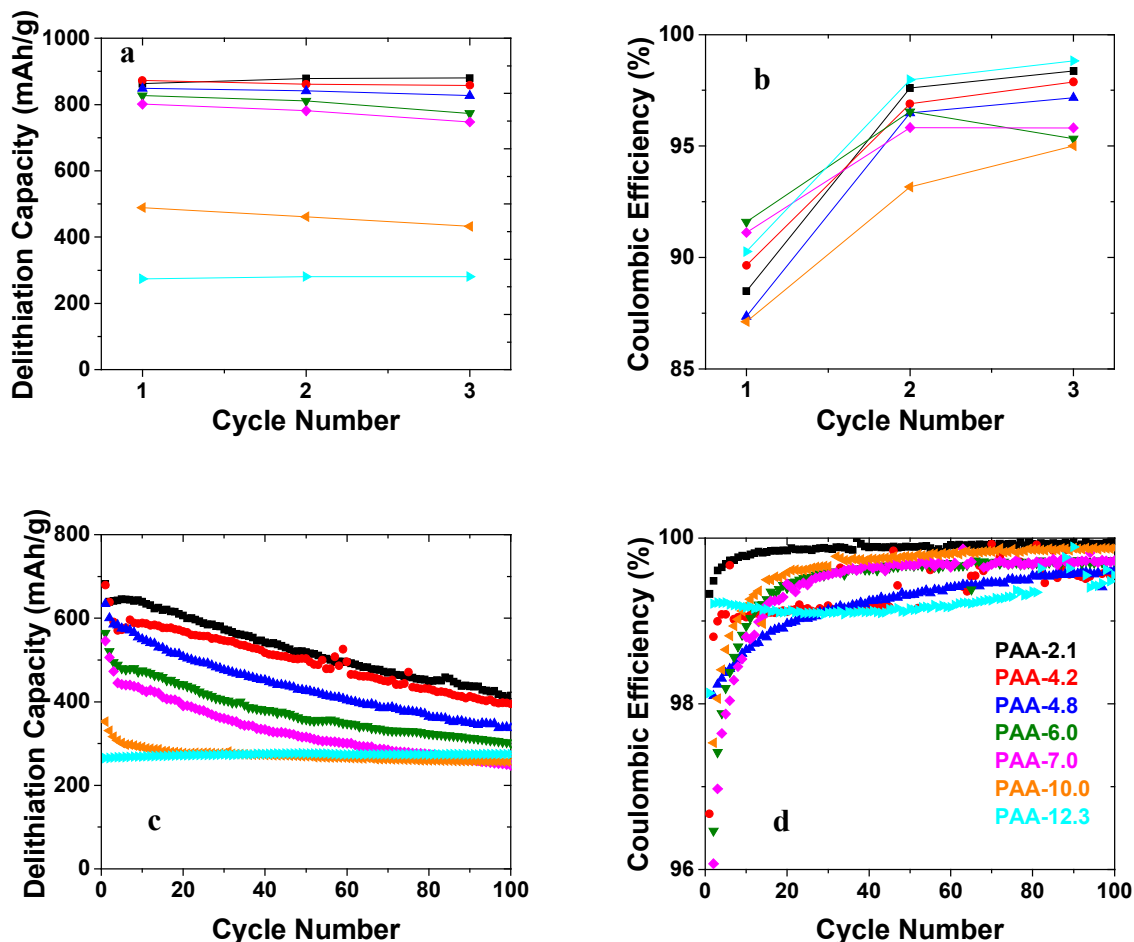


Figure 53. Specific delithiation capacity (a and c) and Coulombic efficiency profiles (b and d) of half cells assembled using lithiated PAA during formation cycles at a C/3 rate (a,b) and after 100 cycles at a C/3 rate (c,d). The pH of the PAA solutions (Figure 51) is color coded in panel d.

all practically significant shear rates. While higher viscosity and shear thinning are favorable physical properties for blending of Si nanoparticles in thick suspensions, slowing down their sedimentation, there seem to be no decisive advantages of lithiated vs. non-lithiated PAA from the processing standpoint.

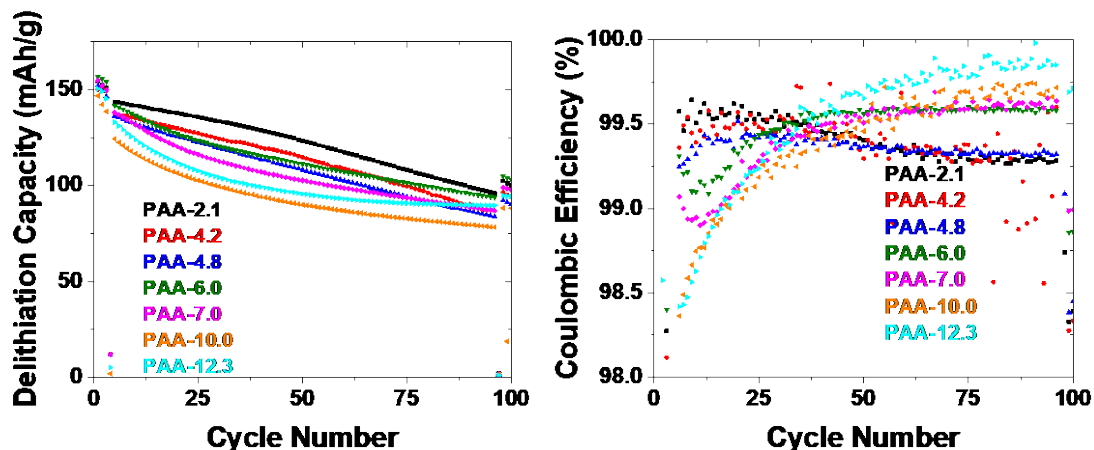


Figure 54. Specific discharge capacity (left) and Coulombic efficiency (right) for full cells. The pH of PAA solutions in Figure 1 is indicated in the plot.

The lithiated PAA binders were then used to fabricate Si/graphite electrodes and later were assembled into half cells to The polymer solutions were then used to fabricate Si-Gr composite electrodes (15% Silicon), and the electrochemical performance was evaluated in half cells. The loading densities of these electrodes were similar around 2.7~3.0 mg/cm². As expected, their half cells performance was very different. The cells containing less lithiated PAA polymers demonstrated higher initial delithiation capacity, average capacity, and capacity retention. (Table 8 and Figure 53). During the formation cycles (Figure 53a), PAA-2.1 cell exhibited the highest initial specific capacity of 695 mAh/g. As pH increased to 7.0, the initial capacity decreased to 598 mAh/g. For pH >4, there was approximately linear decrease of the initial capacity with the increasing pH. For PAA-10.0 and PAA-12.3 cells the initial capacities were 353 mAh/g and 265 mAh/g, respectively. From the capacity profiles (Figure 53c), it is obvious that the cells with less lithiated binders (lower pH value) generally afford better cycling performance. As shown in Figures 53c and 53d, less lithiated PAA binders also demonstrate better capacity retention and coulombic efficiency. The capacity retention decreases from 60% to 40% as pH increases from 2 to 7.

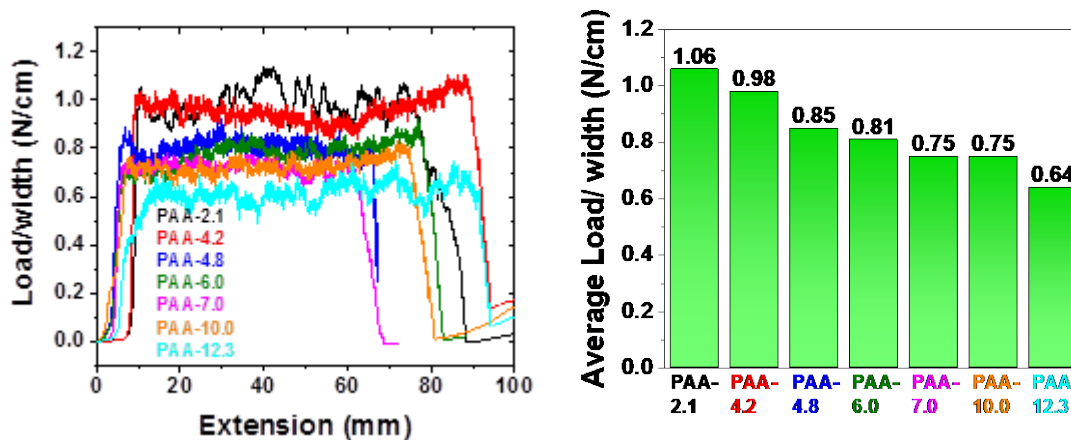


Figure 55. The 180° peeling test for the Si-Gr electrode composed using different PAA binders (left). The load/width ratios averaged over a range of 50 mm for different electrodes (right). The pH of PAA solutions in Figure 51 is indicated in the plots.

Table-8: The N/P ratio, initial capacity, average capacity and capacity retention data of full cells consisting of Si/graphite anode and NCM523 cathode.

Sample		N/P ratio	Initial specific capacity, a mAh/g	Average capacity, mAh/g b	Initial Coulombic efficiency, %c	Capacity retention, % d
1	2.1	1.3	143.6	121.7	99.6	66.8
2	4.2	1.4	137.6	113.2	99.4	63.2
3	4.8	1.3	136.2	108.4	99.2	61.5
4	6.0	1.2	141.5	112.8	99.3	66.3
5	7.0	1.1	138.1	105.4	99.1	63.1
6	10.0	0.9	124.3	93.2	98.4	63.0
7	12.3	0.6	133.1	100.1	98.4	67.3

a) specific discharge capacity after the formation cycles at C/20; b) averaged capacity over 92 cycles; c) first Coulombic efficiency at C/3, after formation cycles at C/20; d) after 92 cycles at C/3.

It is reasonable to suggest that these trends could reflect the ability of the polymer binder to provide structural cohesion in the matrix. In **Figure 55**, the peeling test was used to assess the adhesive/cohesive strength of the electrode. This test suggests that the increased lithiation of PAA decreases the cohesion in the matrix. This can be attributed to the reduced number of $-CO_2H$ groups that esterify siloxyl groups on the surface of Si particles, forming strong bonds between the polymer chains and the Si nanoparticles. Clearly, the reduced cohesion also makes the polymer binder less efficient in countering the effects of volumetric changes of Si particles in the electrode matrix. We remind that according to previous report lithiated PAA is 40% less stiff than non-lithiated PAA, so the two trends (the cohesion and tensile strength) act in the same direction.

The cycling performance of the full cells, in which the Si-Gr electrode is paired with an NCM523 cathode, is shown in **Figure 54**. The N/P ratio, initial and average capacities, the capacity retention, and the area specific impedance (ASI) are summarized in **Table 1**. Low pH cells still exhibited the superior performance and PAA-2.1 cell is the best among them. As pH increased, the cycling performance decreased except for PAA-6.0 cell, which demonstrated arguably the second best performance. Compared to the half-cell results, this relative unclear trend may partly due to the inconsistent cathode/anode matching issues.

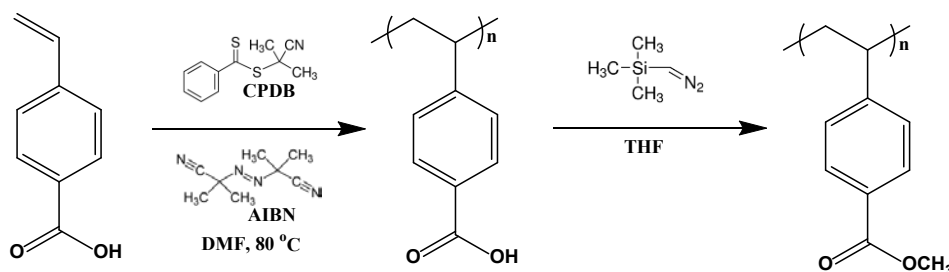


Figure 56. Synthesis of P4VBA and Methylation for GPC Analysis

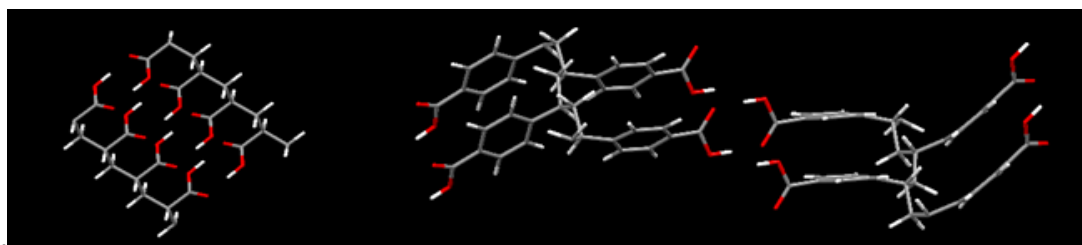


Figure 57. MOPAC Computed Conformations of PAA and P4VBA Dimers

Polybenzoic Acids: While there has been rapid progress in developing water-soluble polymer binders for Si-based electrodes, developing polymer binders that allow water-free processing from organic solvents has lagged behind. Such alternatives are desirable, as the wet processing introduces hard-to-remove moisture that leads to acid corrosion of Si during electrochemical cycling, resulting in rapid capacity fade. Here we demonstrate the use of poly(4-vinylbenzoic acid) (P4VBA) to fabricate high quality Si/graphite composite electrodes from 1-methyl-2-pyrrolidinone (NMP) slurries. Compared to PAA binders, P4VBA provides higher initial and average capacities and better capacity retention. We believe that P4VBA offers the urgently needed alternative to wet processing of the Si-based electrodes.

Polymer chains of varied length were synthesized as shown in **Figure 56**. The arene rings improve stiffness of these polymers (which is important for countering the effects of volume changes) and favor their syndiotacticity. As a result, neighboring P4VBA chains can interlock by H bonding more strongly compared to PAA chains as illustrated in **Figure 57**, resulting in greater cohesion. Below we demonstrate that NMP-processed P4VBA-containing Si/graphite composite (Si-Gr) electrodes considerably outperform PAA-containing electrodes in our electrochemical tests. Three batches of P4VBA with different molecular weights were prepared and characterized as described in the preceding section. Size exclusion chromatograms for these polymers are shown in **Figure 58a**, which also gives the estimates for M_n and PDI. We will refer to these samples as P4VBA-1 (63.5 kDa), P4VBA-2 (29.3 kDa) and P4VBA-3 (11.8 kDa). For comparison, we also used protiated PAA polymer

(29.1 kDa) which had M_n close to P4VBA-2. **Figure 58b** shows the apparent viscosity of 30 wt% P4VBA solutions in NMP plotted as a function of the shear rate. As expected, the viscosity rapidly increases with M_n . While P4VBA-2 and PAA have similar M_n , the viscosity was lower for the PAA solution, especially at high shear rates. The P4VBA solutions behave as Newtonian fluids at the shear rates $< 102 \text{ s}^{-1}$, and they show

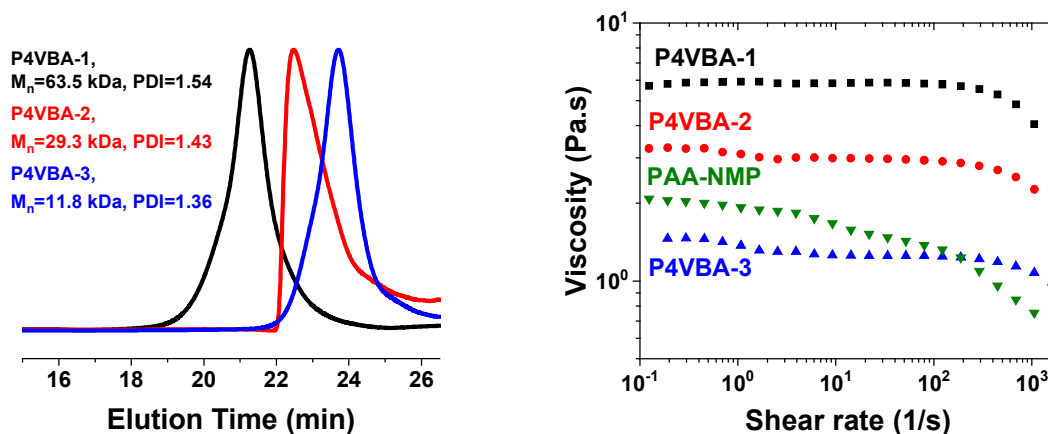


Figure 58. (a) Size exclusion chromatograms for synthesized P4VBA polymers; (b) The apparent viscosity vs. the shear rate for 30 wt% P4VBA solutions in NMP. See the color coding in the plot.

negligible shear thinning at higher rates (in contradistinction to the PAA solutions). As this shear thinning can cause uneven deposition of ink during coating of the laminates, in these NMP solutions the P4VBA binder shows better rheological properties than the PAA binder.

The performance of Si-Gr electrodes fabricated from NMP-polymer slurries was evaluated in half-cells over 100 charge/discharge cycles (**Figure 59**). While the loading densities (**Table 9**) were similar, the cycling behaviors were quite different. The P4VBA cells containing higher M_n polymers exhibited higher initial and average specific capacities and better capacity retention over 100 cycles (**Table 9**). This trend is consistent with what the one we observed for water-based PAA polymers. In contrast to these P4VBA polymers, NMP-processed PAA electrodes performed very poorly, with ca. 70% loss of capacity after 25 cycles. The differential capacity (dQ/dV) plots for cycle 25 shown in indicate the complete loss of the 0.44 V feature from Li15Si4 phase in the latter case, whereas this feature is clearly seen in the P4VBA cells.

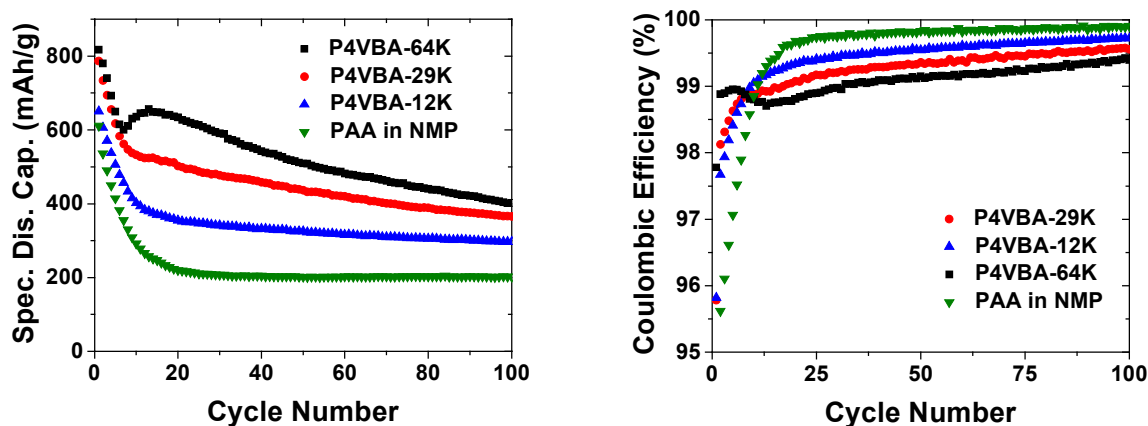


Figure 59. Specific discharge capacity (left) and Coulomb efficiency (right) for different half-cells (100 cycles at a constant C/3 rate).

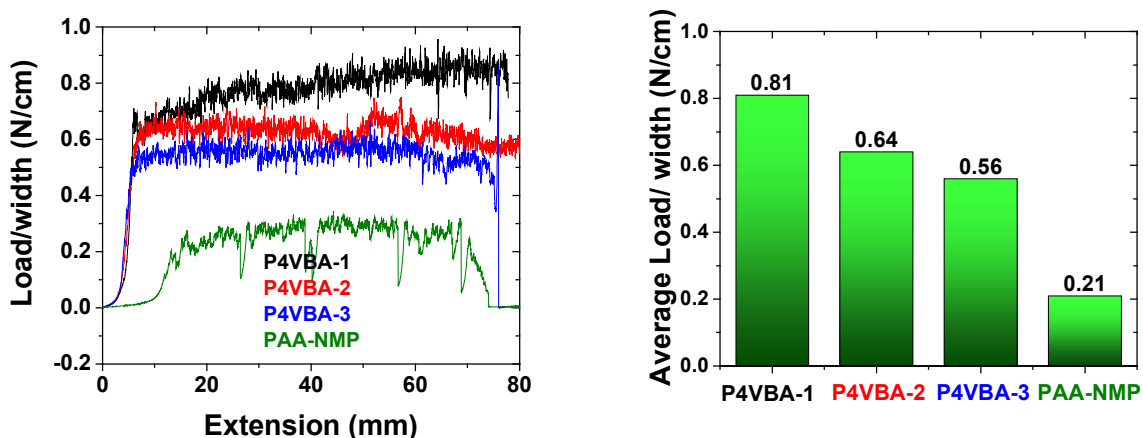


Figure 60. (a) The load/width ratio plotted vs. the extension and (b) the average ratio over the extension range for different S-Gr electrodes.

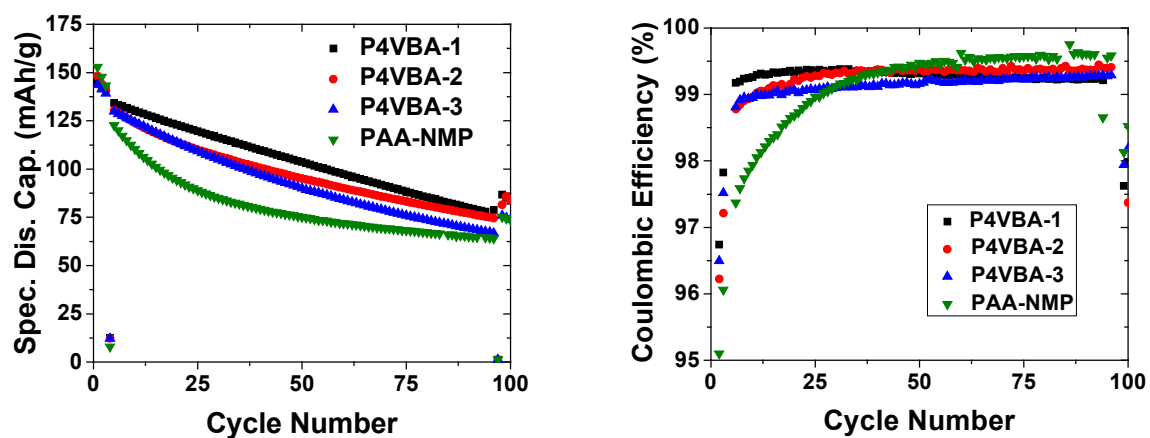


Figure 61. Specific discharge capacity (to the left) and Coulombic efficiency (to the right) for different full-cells.

Table-9: Loading density, initial specific capacity, initial Coulomb efficiency, capacity retention, and average capacity for half-cells.

Cell/ binder	Mn kDa	Loading density, mg/cm ²	Initial specific capacity, ^a mAh/g	Average capacity, mAh/g ^b	Initial Coulombic efficiency, % ^c	Capacity retention, % ^d
P4VBA-1	63.5	2.5	818	527	97.8	49
P4VBA-2	29.3	2.4	787	452	95.8	46
P4VBA-3	11.8	2.6	650	343	95.8	46
PAA	29.1	2.6	611	230	90.9	33

a) for the third formation cycle at a C/20 rate; b) average capacity over 100 cycles at a C/3 rate; c) Coulomb efficiency immediately after the formation cycles; d) capacity retention after 100 cycles at a C/3 rate.

To measure the adhesive/cohesive strength of the electrode a peel strength test was administered using a single column Instron 3343 universal testing system. As suggested by **Figures 60a** and **60b**, the cohesive strength of the P4VBA electrodes is much higher than the PAA electrode, and this strength increases by 45% from P4VBA-

3 to P4VBA-1 in the order of the increasing Mn. The full-cell tests are briefly summarized in **Figure 61**, which shows the same trends as our tests for half-cells. Once again, the P4VBA-1 cell showed the best cycling performance, whereas the PAA cell showed the worst cycling performance.

Initial investigation of the surface reaction between Si particle and binders: It has become more and more recognized that the Si particle's surface chemistry is very sensitive to conditions and often played important roles in influencing the electrode matrix. As a directly interacting component, binders are interacting or reacting to the surface of Si and the resulting binder-Si particle "bonding" often dictates the stability of electrode matrix and the final cycling performance. In some case, when Si particles change, the same binder could behave totally differently. For instance, the same PAA binders can lead to totally different or even reverse cycling performance on different Si particles. In a related study of PAA lithiation,[45] the lithated PAA performed much better compared to the non-lithated PAA binders, which is contradicting to our own results in section 1. The major difference was the Si particle used in both studies. Our study used NanoAmor Si particle, which has high content of pure silicon and limited amount of SiO_x, while in the other study, the Si particle was purchased from Sigma-Aldrich, which has a thick layer of SiO_x based on the XPS results. It is obvious that different source of Si particles can afford different composition and more importantly different surface properties. Therefore, understanding the relationship of the Si particle surface and binders property becomes a crucial challenge that can provide guidance for further optimization of the related materials. Here, we present some initial results toward this target.

Paracelete Si particles were used due to the availability of its large amount and better quality control. Those particles were heat-treated to form controlled SiO₂ layers. In this way, the silicon nanoparticles are oxidized in a controlled manner to obtain different thicknesses of SiO₂ layers.[46] Three samples were studied including the pristine, 400°C, and 600°C treated samples. The growing SiO₂ layers can lead to better protection of the Silicon as well as changes of the surface of the particles, therefore are excellent platforms to study the surface chemistry. Those samples were then used to fabricate Silicon anodes (70% Silicon) with PAA binders. As shown in Figure 62, half cells fabricated with non-lithiated PAA binders were firstly evaluated in half-cells. As expected, 400 °C and 600 °C cells delivered lower initial capacities, but higher Columbic efficiency and better capacity retention. More importantly, they all seem to work well with non-lithiated PAA binders. While these are preliminary results, we speculate that lithiated PAA may give much different cycling performance. More experiments are ongoing and more detailed analysis will be discussed shortly when results are available.

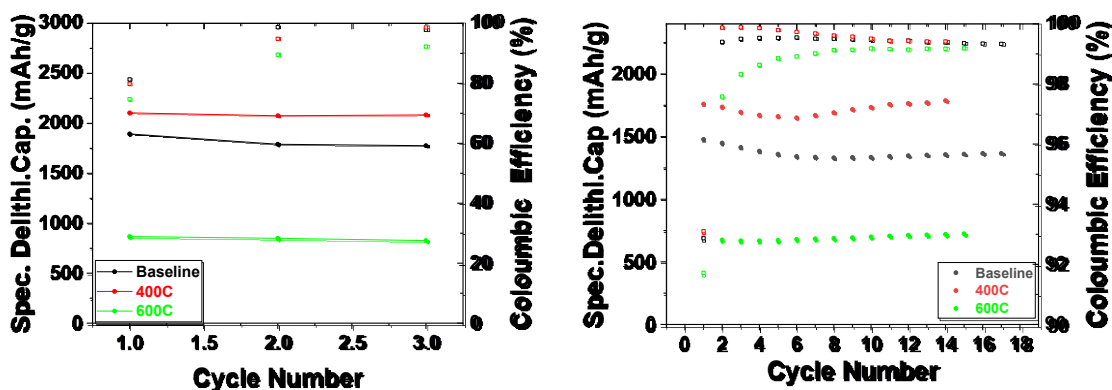


Figure 62. Specific discharge capacity (to the left) and Coulombic efficiency (to the right) for half cells using non-lithiated PAA binders during formation (a) and normal cycling (b).

Lithium Inventory

Lithium inventory control is an issue that is part of the Si deep dive (DD) project. Si/graphite blended electrodes require careful cell-capacity balancing to begin to enable the technology. Typically this requires much thicker (and heavier) cathodes to account for first cycle irreversible capacity losses (ICL). One would like to use a pre-lithiation component either in the anode or the cathode to allow less weight (less heavy) cathodes by negotiating the first cycle irreversible capacity loss on the anode side. In addition, pre-lithiation has been observed to help the cycle life. Another problem to address using pre-lithiation, is electrode voltage slippage; the SOC is hard to control, and cell capacity can be compromised. The usable capacity begins to shrink in the cell, and eventually Li-trapping in the Si material wins out, and lifetime is exhausted. The behavior must be understood and then addressed by the lithium inventory team as part of the overall project. This past year we focused on (1) continued understanding lithium inventory through use of a LiFePO_4 quasi-CE/RE in Si-graphite composite full cells, and (2) alternative methods to Li_5FeO_4 for introducing extra lithium into the cell from the cathode side. Alternative methods include using (a) $\text{Li}_{1+x}\text{NMC532O}_2$ electrodes where x is added Li for the cell, and (b) $\text{Li}_{1+y}\text{Ni}_{0.5}\text{Mn}_{1.5}\text{O}_4$ (lithiated 5 V spinel) wherein y represents the additional Li introduced into the Si-graphite full cell.

Completing the LiFePO_4 (LFP) part of the project culminated in two articles published [47-48]. These papers show the effectiveness of LiFePO_4 as a diagnostic tool in order to assay the quantity of Li consumption in a full cell as marked by the percent loss of lithium per cycle via SEI growth and/or SEI consumption and re-formation. The LFP work was presented in last year's annual report (FY '17).

To wrap up the FY '18 year we also accomplished three year-long objectives that were important to understand Li inventory and its effectiveness to help the Si-graphite anode-containing full cell demonstrate cycle improvement over the baseline.

LFO•NMC532/Si-graphite cell: Lithium iron oxide Li_5FeO_4 (LFO) was added to a NMC532 blended electrode laminate with two different examples of pre-lithiation amounts. The first was 3.3 wt.% LFO (86.7 wt.% 532) which is calculated to eliminate the first cycle ICL (irreversible capacity loss), and the second, 7.1 wt.% LFO (82.9 wt.% 532) which makes the n/p ratio 1.04, which is quite close to the goal of 1.1 ratio match, but will not be enough to detrimentally plate Li on the first charge. The results of Si protocol deep dive cycling (3.0 to 4.1 V) are shown in Figure 63.

The findings indicate that the inclusion of LFO improves the utilization of NMC. Mitigating the ICL (3.3 wt.% LFO; gold markers) increases the capacity of the cell, but the capacity fades at the same rate as the baseline. Maximizing the Li inventory (7.1wt.% LFO; cyan markers) increases the capacity and delays the capacity fade. The capacity retention after 100 cycles for 7.7wt.% LFO full cell is 80%. LFO•NMC cathodes exhibit lower impedance rise across 100 cycles, as determined by HPPC, and show higher rate performance. Thus Li inventory into the Si-graphite cell using LFO can indeed improve the capacity within these parameters. Future investigations will, together with the CAMP facility, focus on scaling up the LFO•NCM laminate casting and seek to better understand the role of LFO in lowering the impedance.

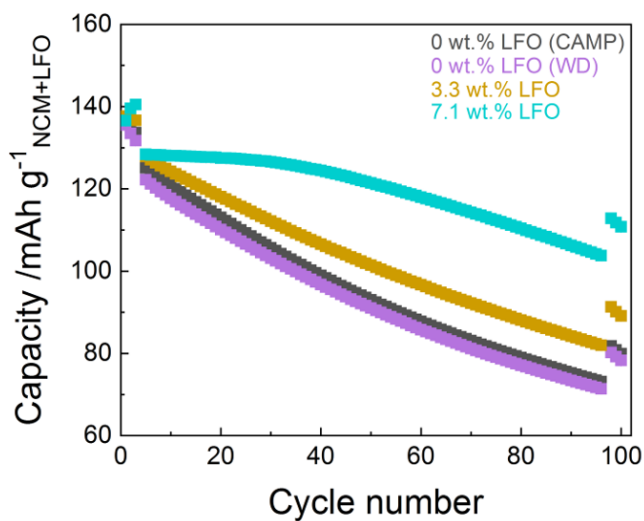


Figure 63. Cathode capacity versus cycle number plot of two LFO weight percent blended NMC532 electrodes (as labeled) together with the non LFO-containing Si-graphite full cells. In each case the Si-graphite electrode is from CAMP (A-A013). Black markers show the baseline performance, where the NMC cathode is from CAMP (A-C013B). The colored markers use a glove-box cast electrode, with the magenta markers serving as a 0 % LFO proxy (baseline) for the LFO-containing cells.

Note the glove-box cast electrodes (magenta (WD label)) match the performance of the CAMP full cells.

$\text{Li}_{1+x}\text{NMC532O}_2/\text{Si-graphite}$ cell: As LFO located within the cathode compartment of the cell (after Li release on the first charge) adds dead inactive weight to the cell with cycling, we hypothesized that over-lithiated NMC532 may be a good way to introduce Li into the cell, but not add dead weight. Thus to do this experiment, we discharge the NMC532 electrode first in a Li half-cell, then extract the over-lithiated NMC (x is amount of Li added into the system) electrode, after which a full cell is then rebuilt with the Si-graphite anode. Note we can control the amount of x inserted into the NMC532 layer by limiting the first discharge of pristine NMC532. Figure 64 shows the result on the cycling properties with the electrochemically produced over-lithiated NMC532 in a full cell at a few different x values (see caption Fig. 64).

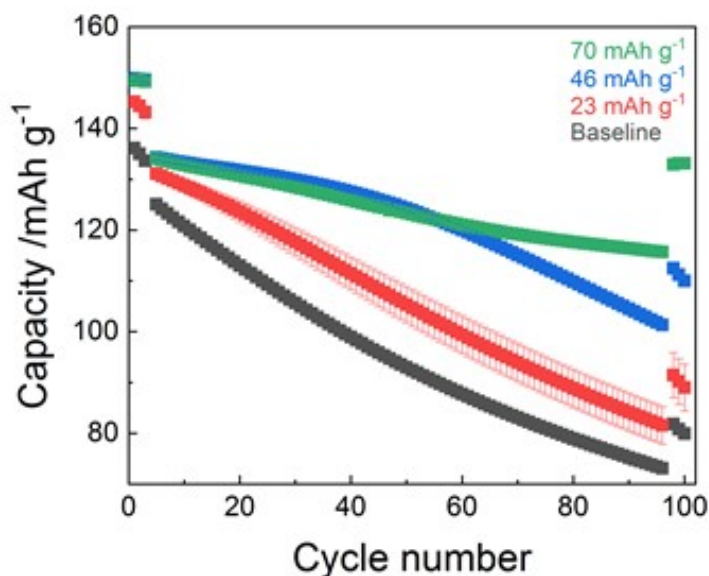


Figure 64. Cathode capacity versus cycle number plot (Si DD protocol) of three over-lithiated $\text{Li}_{1+x}\text{NMC5320}_2/\text{Si-graphite}$ full cells, and one black baseline cell. The x value represents the extra Li introduced into the cell (Li inventory) from prior electrochemical lithiation in a Li half cell. The labels are red markers (23 mAhg^{-1} ; $x = 0.09$), blue markers (46 mAhg^{-1} ; $x = 0.17$), and green markers (70 mAhg^{-1} ; $x = 0.26$). Note the black markers (baseline) is the matched NMC532/Si-graphite CAMP electrodes in a full cell.

The experiments demonstrate the following observations. Increasing the Li inventory (either by 46 or 70 mAhg^{-1}) delays the capacity fade. A 70 mAhg^{-1} over-lithiation capacity yields 89% capacity retention over 100 cycles compared to 59% for baseline cell. The capacity retention in early cycles correlates well with high Coulombic efficiency, and is due to a Li reserve on the anodes compensating for capacity losses in early cycles. An independent measurement of impedance via HPPC cycle indicates that the over-lithiated NMC has a similar impedance rise over cycling from cycle 4 to cycle 97.

$\text{Li}_{1+y}\text{Ni}_{0.5}\text{Mn}_{1.5}\text{O}_4/\text{Si-graphite}$ cell: Chemical lithiation using lithium metal dissolved in liquid ammonia was introduced this past year as a viable, potentially scalable method to over-lithiate cathode materials, in this case, the 5V spinel $\text{Li}_{1+y}\text{Ni}_{0.5}\text{Mn}_{1.5}\text{O}_4$ (LNMO or LiNMO) [49]. In this formula the value of y represents the amount of extra lithium inserted into the spinel. Such over-lithiated cathodes can subsequently be used to pre-lithiate high-energy anodes in a lithium-ion battery configuration during the first charge step. Lithiated 5V spinel $\text{Li}_{1+y}\text{Ni}_{0.5}\text{Mn}_{1.5}\text{O}_4$ cathode materials prepared by this technique show higher first delithiation capacities, confirming the chemically inserted lithium is electrochemically active. Full cells with a Si-graphite anode and the $\text{Li}_{1+y}\text{Ni}_{0.5}\text{Mn}_{1.5}\text{O}_4$ ($y=0.62$) cathode show a 23% higher reversible capacity in the first cycle than $\text{LiNi}_{0.5}\text{Mn}_{1.5}\text{O}_4$ baseline cells, and improved capacity retention. The extra, chemically inserted lithium therefore sacrificially compensates for the loss of lithium at the anode allowing higher utilization of the cathode capacity in following cycles.

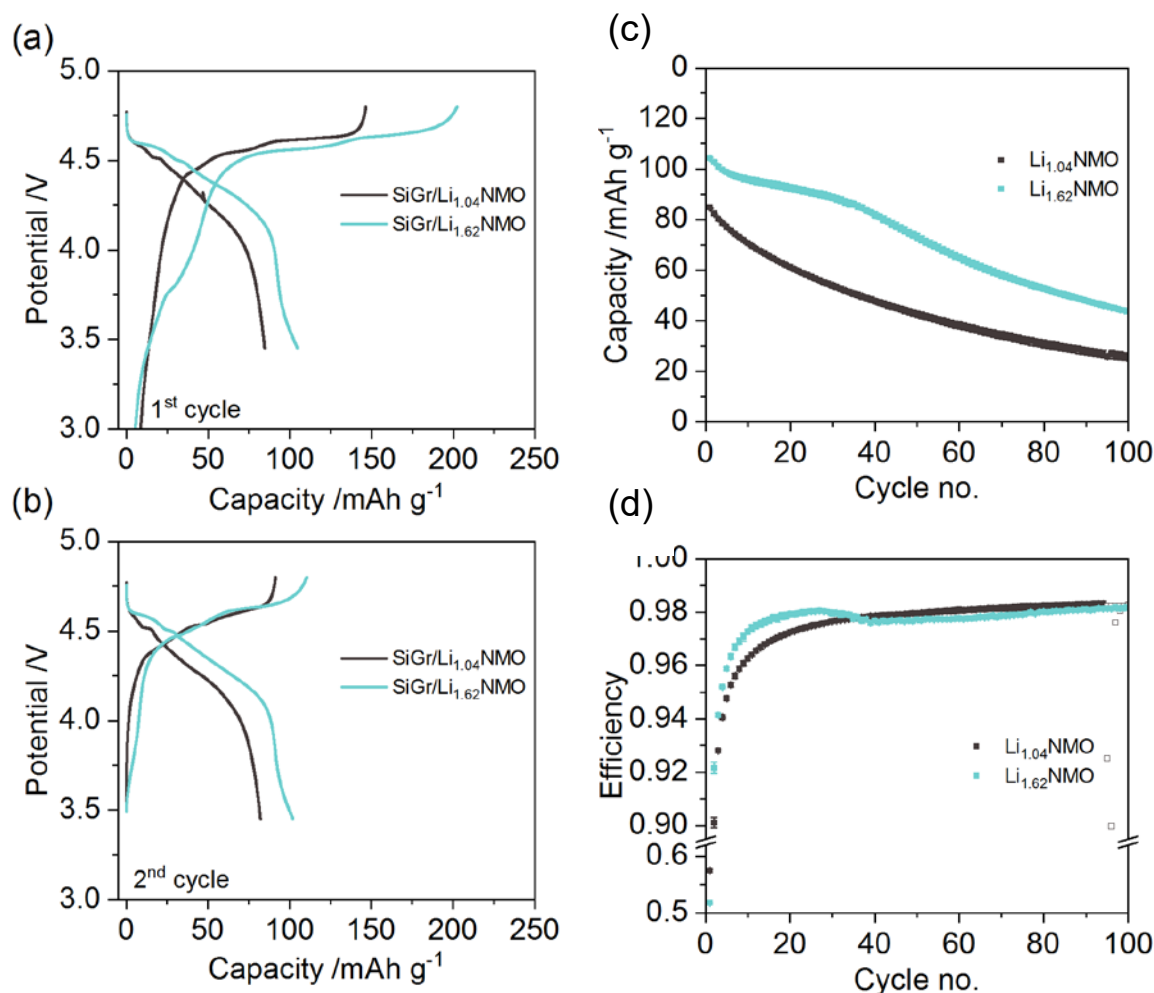


Figure 65. Full cell potential profiles for the (a) first and (b) second charge and discharge of $\text{LiNi}_{0.5}\text{Mn}_{1.5}\text{O}_4$ and chemically lithiated $\text{Li}_{1.62}\text{Ni}_{0.5}\text{Mn}_{1.5}\text{O}_4$ versus a Si-graphite composite anode at a rate of C/10. Full cell (c) discharge capacity and (d) cycle efficiency over 100 cycles for $\text{LiNi}_{0.5}\text{Mn}_{1.5}\text{O}_4$ and chemically lithiated $\text{Li}_{1.62}\text{Ni}_{0.5}\text{Mn}_{1.5}\text{O}_4$ versus Si-graphite at a rate of C/10. Filled data symbols represent the average of two duplicate cells, with error bars showing the deviation between them. The open data symbols in (b) represent the region where a scheduled ~20 h power shutdown interrupted cycling of $\text{LiNi}_{0.5}\text{Mn}_{1.5}\text{O}_4$ and the subsequent cell recovery/break-in time (cycles 95-100). In this region, data is shown from the two cells separately since they were interrupted on different cycle numbers. Cycling conditions: 4.8 to 3.5 V, C/10, 30 °C, and GEN2 electrolyte containing 10% FEC.

Pre-lithiation becomes more important when the ICL of the anode is large. To illustrate this, the first and second cycle potential profiles of Si-graphite/ $\text{Li}_{1.04}\text{NMO}$ and Si-graphite/ $\text{Li}_{1.62}\text{NMO}$ full cells are shown in Figures 65a and 65b. Due to the larger ICL of the Si-graphite electrode, the Coulombic efficiency for $\text{Li}_{1.04}\text{NMO}$ is 57 % (charge and discharge capacity of 147 and 85 $\text{mAh g}^{-1}_{\text{LNMO}}$, respectively). Conversely, with pre-lithiation the first charge capacity of $\text{Li}_{1.62}\text{NMO}$ is 201 $\text{mAh g}^{-1}_{\text{LNMO}}$, with a reversible capacity of 104 $\text{mAh g}^{-1}_{\text{LNMO}}$. The reversible capacity is therefore 19 $\text{mAh g}^{-1}_{\text{LNMO}}$ higher for the cells where the ICL is compensated by the cathode pre-lithiation; a 23 % improvement. The increased first discharge capacity carries over into subsequent cycles (Figure 65b), and after 100 cycles at C/10 the cells with $\text{Li}_{1.62}\text{NMO}$ deliver 44 $\text{mAh g}^{-1}_{\text{LNMO}}$ of capacity (Figures 65c and 65d). This is 18 $\text{mAh g}^{-1}_{\text{LNMO}}$ higher than the baseline $\text{Li}_{1.04}\text{NMO}$ case. Additionally, the capacity retention over 100 cycles is higher for $\text{Li}_{1.62}\text{NMO}$ relative to $\text{Li}_{1.04}\text{NMO}$ (42 % and 30 %, respectively).

Conclusions: Electrode Construction

A novel designing practice of functional conductive binders and latex binders for lithium ion batteries has been conducted. A series of conductive polymer binder emulsions in water has been prepared using emulsion polymerization methods. These polymer emulsions have been further used for lithium ion battery applications. The electrode coating process is water-based without using any organic solvents, which is lower in cost and more environmentally friendly. Using these polymer emulsions as the binder, silicon materials, solely or together with graphite materials, have been fabricated into electrodes showing promising cycling performance.

A rational design, synthesis and testing of electrolyte additives have been conducted. Two classes of bi-functional electrolyte additives with surface reaction functional group and coating functional group on one molecule have been synthesized. A toolbox is under construction with different reactive groups and hydrophobic and hydrophilic surface coating groups. The preliminary results show the surface reactive groups are able to form surface coating on the active materials, whereas the film functional groups can provide designed interaction with the electrolyte. Advanced diagnostic and full cell testing will be applied to these bi-functional electrolyte additives to further elucidate the molecular level interactions and quantify their electrochemical performances.

Lithium inventory in Si-containing full cells has been evaluated from the standpoint of diagnostic tools with LiFePO_4 as a quasi-CE/RE in Si-graphite blended composite anode-containing cells, and from loading the cell with extra lithium sources introduced at the cathode side such as Li_5FeO_4 , $\text{Li}_{1+x}\text{NMC532O}_2$, and $\text{Li}_{1+y}\text{Ni}_{0.5}\text{Mn}_{1.5}\text{O}_4$ spinel. All three methods of lithium introduction works in the Si-graphite cell at some level. From our results we find that the more Li introduced into the cell will increase the lifetime of the Si-containing cell to the extent that the extra Li is exhausted from SEI reactions. We need significant improvement to the SEI stability to mitigate irreversible Li consuming processes occurring on each cycle. Reversible SEI stripping and reformation without Li loss on every cycle would be excellent. Finally, if one can leak Li into the cell over the lifetime of the battery, perhaps dosing every 100 cycles, then we surmise that a better performance will be achieved.

Extensive efforts have been conducted towards gain in-depth understanding of the factors controlling the performance of PAA binders and evolving those binders towards improved cell performance for silicon lithium-ion batteries. Firstly, PAA binders were used to study the effect of Li^+ exchange in the polymer binder (the pre-lithiation of PAA) on the properties and electrochemical cycling of cells containing Si-Gr composite electrodes. From the standpoint of material chemistry, the pre-lithiation of PAA does not confer significant benefits and can be detrimental. For instance, it increases the viscosity and shear thinning of aqueous solutions and slurries and reduced the cohesion between the particles in the electrode matrices. Furthermore, for both half cells and full cells, sparse lithiation of the binder notably improves the cycling performance. For half cells, there is severe depletion of Si nanoparticles for Li^+ substitution $> 95\%$ (pH 7) due to corrosion during fabrication of the electrode. The optimum pH range is between 2 and 4, and the best results are obtained without any pre-lithiation. The peeling test of the fabricated electrodes showed that the pre-lithiation can adversely affect the mechanical strength of the prepared binders. Thus, it appears that contrary to the current practice of pre-lithiation of PAA by titration of the solutions to pH 7 (lithiation ratio > 0.9), little to no pre-lithiation may be more favorable for improved performance for Si-Gr composite anode batteries. Secondly, NMP-soluble poly(4-vinylbenzoic acid) (P4VBA) polymers were synthesized and used as binders to fabricate high-quality Si/graphite composite electrodes from water-free slurries. Compared to PAA, these P4VBA polymers (of the equivalent or higher Mn) have higher viscosity and lower shear thinning in the NMP solutions, yielding good quality electrode coatings with superior adhesive strengths (4X over PAA). The initial

and average capacity, Coulombic efficiencies, and capacity retention were also much better for these P4VBA polymer binders, and our post-mortem SEM examination suggests that the longer chain P4VBA polymers inhibit morphological deterioration of the electrode matrix during electrochemical cycling. Our results indicate that long-chain (~64 kDa) P4VBA can serve as an excellent polymer binder for fabrication of Si-based electrodes from NMP, which makes this polymer an appealing alternative to water-soluble polycarboxylate binders that introduce moisture leading to faster degradation of Si particles through the formation of corrosive HF.

5. Key Publications

1. K. Kalaga, M.-T. Rodrigues, S.E. Trask, I.A. Shkrob, D.P. Abraham, “Calendar-life versus Cycle-life aging of Lithium-ion Cells with Silicon-Graphite Composite Electrodes”, *Electrochimica Acta* **280** (2018) p. 221.
2. K. Kalaga, I.A. Shkrob, R.T. Haasch, C. Peebles, J. Bareño, D.P. Abraham, “Auger Electrons as Probes for Composite Micro and Nanostructured Materials: Application to Solid Electrolyte Interphases in Graphite and Silicon-Graphite Electrodes”, *J. Phys. Chem. C* **121** (2017), p. 23333.
3. J. Bareño, I.A. Shkrob, J.A. Gilbert, M. Klett, D.P. Abraham, “Capacity Fade and Its Mitigation in Li-ion Cells with Silicon-Graphite Electrodes”, *J. Phys. Chem. C* **121** (2017) p. 20640.
4. K.P.C. Yao, J.S. Okasinski, K. Kalaga, J.D. Almer, D.P. Abraham, “Operando Quantification of (De)Lithiation Behavior of Silicon-Graphite Blended Electrodes for Lithium-Ion Batteries”, *Advanced Energy Materials* (2018), under review.
5. Caleb Stetson, Taeho Yoon, Jaclyn Coyle, William Nemeth, Matt Young, Andrew Norman, Svitlana Pylypenko, Chunmei Ban, Chun-Sheng Jiang, Mowafak Al-Jassim, Anthony Burrell, submitted
6. Zhao, H.; Wei, Y.; Wang, C.; Qiao, R. M.; Yang, W. L.; Messersmith, P. B.; Liu, G., Mussel-Inspired Conductive Polymer Binder for Si-Alloy Anode in Lithium-Ion Batteries. *Acs Applied Materials & Interfaces* **2018**, *10* (6), 5440-5446.
7. Zhang, G. Z.; Yang, Y.; Chen, Y. H.; Huang, J.; Zhang, T.; Zeng, H. B.; Wang, C. Y.; Liu, G.; Deng, Y. H., A Quadruple-Hydrogen-Bonded Supramolecular Binder for High-Performance Silicon Anodes in Lithium-Ion Batteries. *Small* **2018**, *14* (29).
8. Yao, K.; Ling, M.; Liu, G.; Tong, W., Chemical Reduction Synthesis and Electrochemistry of Si-Sn Nanocomposites as High-Capacity Anodes for Li-Ion Batteries. *J. Phys. Chem. Lett.* **2018**, *9* (17), 5130-5134.
9. Yang, S. M.; Gu, Y. Y.; Qu, Q. T.; Zhu, G. B.; Liu, G.; Battaglia, V. S.; Zheng, H. H., Engineered Si@alginate microcapsule-graphite composite electrode for next generation high-performance lithium-ion batteries. *Electrochim. Acta* **2018**, *270*, 480-489.
10. Wang, Y.; Zheng, X. Y.; Qu, Q. T.; Liu, G.; Battaglia, V. S.; Zheng, H. H., A novel maleic acid/graphite composite anode for lithium ion batteries with high energy and power density. *Carbon* **2018**, *132*, 420-429.
11. Sabisch, J. E. C.; Anapolsky, A.; Liu, G.; Minor, A. M., Evaluation of using pre-lithiated graphite from recycled Li-ion batteries for new LiB anodes. *Resour. Conserv. Recycl.* **2018**, *129*, 129-134.
12. Gao, X. M.; Ding, Y. L.; Qu, Q. T.; Liu, G.; Battaglia, V. S.; Zheng, H. H., Optimizing solid electrolyte interphase on graphite anode by adjusting the electrolyte solution structure with ionic liquid. *Electrochim. Acta* **2018**, *260*, 640-647.
13. Fang, S.; Li, N.; Zheng, T. Y.; Fu, Y. B.; Song, X. Y.; Zhang, T.; Li, S. P.; Wang, B.; Zhang, X. G.; Liu, G., Highly Graphitized Carbon Coating on SiO with a - Stacking Precursor Polymer for High Performance Lithium-Ion Batteries. *Polymers* **2018**, *10* (6).

14. Chen, H.; Ling, M.; Hencz, L.; Ling, H. Y.; Li, G. R.; Lin, Z.; Liu, G.; Zhang, S. Q., Exploring Chemical, Mechanical, and Electrical Functionalities of Binders for Advanced Energy-Storage Devices. *Chem. Rev.* **2018**, *118* (18), 8936-8982.
15. Liu, D.; Fina, M.; Guo, J. H.; Chen, X. B.; Liu, G.; Johnson, S. G.; Mao, S. S., Organic light-emitting diodes with carbon nanotube cathode-organic interface layer. *Applied Physics Letters* **2009**, *94* (1), 3.

6. References

1. *Alloy Negative Electrodes for Li-Ion Batteries*. M.N. Obrovac and V.L. Chevrier, Chem, Rev. 2014, 114, 11444-11503.
2. *Modeling the Performance and Cost of Lithium-Ion Batteries for Electric-Drive Vehicles*. Second Edition, Argonne National Laboratory Report, ANL-12/55.
3. Hatchard, T. D.; Dahn, J. R., Study of the Electrochemical Performance of Sputtered Si_{1-x}Sn_x Films. *Journal of The Electrochemical Society* 2004, 151 (10), A1628-A1635.
4. Ahn, H.-J.; Kim, Y.-S.; Park, K.-W.; Seong, T.-Y., Use of Sn-Si nanocomposite electrodes for Li rechargeable batteries. *Chemical Communications* 2005, (1), 43-45.
5. Yao, K.; Ling, M.; Liu, G.; Tong, W., Chemical Reduction Synthesis and Electrochemistry of Si-Sn Nanocomposites as High-Capacity Anodes for Li-Ion Batteries. *The Journal of Physical Chemistry Letters* 2018, 9 (17), 5130-5134.
6. Xu, J.; Ling, M.; Terborg, L.; Zhao, H.; Qiu, F.; Urban, J. J.; Kostecki, R.; Liu, G.; Tong, W., Facile Synthesis and Electrochemistry of Si-Sn-C Nanocomposites for High-Energy Li-Ion Batteries. *Journal of The Electrochemical Society* 2017, 164 (7), A1378-A1383.
7. Li, J. L.; Daniel, C.; Wood, D., Materials processing for lithium-ion batteries. *Journal of Power Sources* 2011, 196, 2452-2460.
8. Wood, D. L.; Li, J.; Daniel, C., Prospects for reducing the processing cost of lithium ion batteries. *Journal of Power Sources* 2015, 275, 234-242.
9. Wood, D. L.; Li, J.; Daniel, C., Prospects for reducing the processing cost of lithium ion batteries. *Journal of Power Sources* 2015, 275, 234-242.
10. Toudjine, A.; Morcrette, M.; Courty, M.; Davoisne, C.; Lejeune, M.; Mariage, N.; Porcher, W.; Larcher, D., Partially Oxidized Silicon Particles for Stable Aqueous Slurries and Practical Large-Scale Making of Si-Based Electrodes. *J. Electrochem. Soc.* 2015, 162, A1466-A1475.
11. Zhang, L.; Liu, Y.; Key, B.; Trask, S. E.; Yang, Z.; Lu, W., Silicon Nanoparticles: Stability in Aqueous Slurries and the Optimization of the Oxide Layer Thickness for Optimal Electrochemical Performance. *ACS Appl. Mater. Interfaces* 2017, 9, 32727-32736.
12. Xun, S.; Song, X.; Wang, L.; Grass, M. E.; Liu, Z.; Battaglia, V. S.; Liu, G., The Effects of Native Oxide Surface Layer on the Electrochemical Performance of Si Nanoparticle-Based Electrodes.
13. Gurkaynak, A.; Tubert, F.; Yang, J.; Matyas, J.; Spencer, J. L.; Gryte, C. C., High-temperature degradation of polyacrylic acid in aqueous solution. *Journal of Polymer Science Part A: Polymer Chemistry* 1996, 34, 349-355.
14. Porcher, W.; Chazelle, S.; Boulineau, A.; Mariage, N.; Alper, J. P.; Van Rompaey, T.; Bridel, J.-S.; Haon, C., Understanding Polyacrylic Acid and Lithium Polyacrylate Binder Behavior in Silicon Based Electrodes for Li-Ion Batteries. *J. Electrochem. Soc.* 2017, 164, A3633-A3640.

15. Philippe, B.; Dedryvere, R.; Allouche, J.; Lindgren, F.; Gorgoi, M.; Rensmo, H.; Gonbeau, D.; Edstrom, K., Nanosilicon Electrodes for Lithium-Ion Batteries: Interfacial Mechanisms Studied by Hard and Soft X-ray Photoelectron Spectroscopy. *Chem. Mat.* 2012, 24, 1107-1115.
16. Cabaniss, G. E.; Diamantis, A. A.; Murphy, W. R.; Linton, R. W.; Meyer, T. J., ELECTROCATALYSIS OF PROTON-COUPLED ELECTRON-TRANSFER REACTIONS AT GLASSY-CARBON ELECTRODES. *J. Am. Chem. Soc.* 1985, 107, 1845-1853.
17. Hofstein, S. R., PROTON AND SODIUM TRANSPORT IN SIO₂ FILMS. *IEEE Trans. Electron Devices* 1967, ED14, 749-+.
18. Seidel, H.; Csepregi, L.; Heuberger, A.; Baumgärtel, H., Anisotropic Etching of Crystalline Silicon in Alkaline Solutions: I. Orientation Dependence and Behavior of Passivation Layers. *J. Electrochem. Soc.* 1990, 137, 3612-3626.
19. C. J. Wen, R. Huggins, *J. Solid State Chemistry*, 1981, 37, pp 271-278.
20. B. Key, R. Bhattacharyya, M. Morcrette, V. Seznec, J-M. Tarascon, C. P. Grey, *J. Am. Chem. Soc.*, 2009, 131 (26), pp 9239–9249
21. B. Key, M. Morcrette, J-M. Tarascon, C. P. Grey, *J. Am. Chem. Soc.*, 2011, 133 (3), pp 503–512
22. *Multinuclear Solid-State Nuclear Magnetic Resonance of Inorganic Materials*, Volume 6, 1st Edition, Authors: Kenneth MacKenzie M.E. Smith
23. Q. Zhang, Y. Cui, E. Wang. *Modelling Simul. Mater. Sci. Eng.* 2013, 21, 074001S. Xun et al. "Improved Initial Performance of Si Nanoparticles by Surface Oxide Reduction for Lithium-Ion Battery Application", *Electrochemical and Solid-State Letters*, 2011, 14(5)
24. Zhang, L.; Liu, Y.; Key, B.; Trask, S. E.; Yang, Z.; Lu, W., Silicon Nanoparticles: Stability in Aqueous Slurries and the Optimization of the Oxide Layer Thickness for Optimal Electrochemical Performance. *ACS Appl. Mater. Interfaces* 2017, 9 (38), 32727-32736.
25. Aguiar, H.; Serra, J.; González, P.; León, B., Structural study of sol–gel silicate glasses by IR and Raman spectroscopies. *J. Non-Cryst. Solids* 2009, 355 (8), 475-480.
26. Vreugdenhil, A. J.; Balbyshev, V. N.; Donley, M. S., Nanostructured silicon sol-gel surface treatments for Al 2024-T3 protection. *Journal of Coatings Technology* 2001, 73 (915), 35-43.
27. Mu, J.; Liu, Y.; Zheng, S., Inorganic–organic interpenetrating polymer networks involving polyhedral oligomeric silsesquioxane and poly(ethylene oxide). *Polymer* 2007, 48 (5), 1176-1184.
28. Oliver, M. S.; Blohowiak, K. Y.; Dauskardt, R. H., Molecular structure and fracture properties of ZrOX/Epoxy silane hybrid films. *J. Sol-Gel Sci. Technol.* 2010, 55 (3), 360-368.
29. Higgins, T. M.; Park, S. H.; King, P. J.; Zhang, C.; McEvoy, N.; Berner, N. C.; Daly, D.; Shmeliov, A.; Khan, U.; Duesberg, G.; Nicolosi, V.; Coleman, J. N., A Commercial Conducting Polymer as Both Binder and Conductive Additive for Silicon Nanoparticle-Based Lithium-Ion Battery Negative Electrodes. *ACS Nano* 2016, 10 (3), 3702-3713.
30. Philippe, B.; Dedryvere, R.; Allouche, J.; Lindgren, F.; Gorgoi, M.; Rensmo, H.; Gonbeau, D.; Edström, K., Nanosilicon Electrodes for Lithium-Ion Batteries: Interfacial Mechanisms Studied by Hard and Soft X-ray Photoelectron Spectroscopy. *Chem. Mater.* 2012, 24 (6), 1107-1115.
31. Philippe, B.; Dedryvere, R.; Gorgoi, M.; Rensmo, H.; Gonbeau, D.; Edström, K., Role of the LiPF₆ Salt for the Long-Term Stability of Silicon Electrodes in Li-Ion Batteries – A Photoelectron Spectroscopy Study. *Chem. Mater.* 2013, 25 (3), 394-404.
32. Wu, M.; Xiao, X.; Vukmirovic, N.; Xun, S.; Das, P. K.; Song, X.; Olalde-Velasco, P.; Wang, D.; Weber, A. Z.; Wang, L. W.; Battaglia, V. S.; Yang, W.; Liu, G., Toward an Ideal Polymer Binder Design for High-Capacity Battery Anodes. *J. Am. Chem. Soc.* 2013, 135 (32), 12048-12056.
33. A. L. Michan, B. S. Parimalam, M. Leskes, R. N. Kerber, T. Yoon, C. P. Grey, and B. L. Lucht, *Chemistry of Materials*, 28 (22), 8149-8159 (2016)

34. Caleb Stetson, Taeho Yoon, Jaclyn Coyle, William Nemeth, Matt Young, Andrew Norman, Svitlana Pylypenko, Chunmei Ban, Chun-Sheng Jiang, Mowafak Al-Jassim, Anthony Burrell, submitted
35. Cao Cuong Nguyen, Taeho Yoon, Daniel M Seo, Pradeep Guduru, Brett L Lucht, ACS applied materials & interfaces 8 (19), 12211-12220
36. K. W. D. Kaveendi Chandrasiri, CC Nguyen, BS Parimalam, S Jurng, BL Lucht, Journal of The Electrochemical Society 165 (10), A1991-A1996 Aiken, C. P.; Xia, J.; Wang, D. Y. H.; Stevens, D. A.; Trussler, S.; Dahn, J. R., An Apparatus for the Study of In Situ Gas Evolution in Li-Ion Pouch Cells. *J. Electrochem. Soc.* **2014**, *161*, A1548-A1554.
37. Wang et al. “Enhanced electrochemical performance of lithium metasilicate-coated LiNiCoMnO₂ Ni-rich cathode for Li-ion batteries at high cutoff voltage”, *Electrochimica Acta*, 2016, 222, 806-819
38. Lee. et al., “High-performance silicon-based multicomponent battery anodes produced via synergistic coupling of multifunctional coating layers”, *Energy Environ. Sci.*, 2015, 8, 2075-2084
39. Gu, M.; Xiao, X. C.; Liu, G.; Thevuthasan, S.; Baer, D. R.; Zhang, J. G.; Liu, J.; Browning, N. D.; Wang, C. M., Mesoscale Origin of the Enhanced Cycling-Stability of the Si-Conductive Polymer Anode for Li-ion Batteries. *Sci Rep* **2014**, *4*, 7.
40. Shi, F. F.; Ross, P. N.; Zhao, H.; Liu, G.; Somorjai, G. A.; Komvopoulos, K., A Catalytic Path for Electrolyte Reduction in Lithium-Ion Cells Revealed by in Situ Attenuated Total Reflection-Fourier Transform Infrared Spectroscopy. *Journal of the American Chemical Society* **2015**, *137* (9), 3181-3184.
41. Park, S. J.; Zhao, H.; Ai, G.; Wang, C.; Song, X. Y.; Yuca, N.; Battaglia, V. S.; Yang, W. L.; Liu, G., Side-Chain Conducting and Phase-Separated Polymeric Binders for High-Performance Silicon Anodes in Lithium-Ion Batteries. *Journal of the American Chemical Society* **2015**, *137* (7), 2565-2571.
42. Zhao, H.; Park, S. J.; Shi, F. F.; Fu, Y. B.; Battaglia, V.; Ross, P. N.; Liu, G., Propylene Carbonate (PC)-Based Electrolytes with High Coulombic Efficiency for Lithium-Ion Batteries. *J. Electrochem. Soc.* **2014**, *161* (1), A194-A200.
43. B. Hu, I. A. Shkrob, S. Zhang, L. Zhang, J. Zhang, Y. Li, C. Liao, Z. Zhang, W. Lu and L. Zhang, *Journal of Power Sources*, 2018, 378, 671-676.
44. W. Porcher, S. Chazelle, A. Boulineau, N. Mariage, J. P. Alper, T. Van Rompaey, J.-S. Bridel and C. Haon, *Journal of The Electrochemical Society*, 2017, 164, A3633-A3640.
45. Z.-J. Han, K. Yamagiwa, N. Yabuuchi, J.-Y. Son, Y.-T. Cui, H. Oji, A. Kogure, T. Harada, S. Ishikawa, Y. Aoki and S. Komaba, *Physical Chemistry Chemical Physics*, 2015, 17, 3783-3795.
46. L. Zhang, Y. Liu, B. Key, S. E. Trask, Z. Yang and W. Lu, *ACS Applied Materials & Interfaces*, 2017, 9, 32727-32736.
47. W. M. Dose, V. A. Maroni, M. J. Piernas-Muñoz, S. E. Trask, I. Bloom, and C. S. Johnson “Assessment of Li-Inventory in cycled Si-Graphite anodes using LiFePO₄ as a diagnostic cathode”, , *J. Electrochem. Soc.*, (2018), **165**, A2389-A2396.
48. W. M. Dose, M. J. Piernas-Munoz, V. A. Maroni, S. E. Trask, I. Bloom and C. S. Johnson “Capacity fade in high energy silicon-graphite electrodes for lithium-ion batteries”, , *Chemical Communications*, (2018), **54**, 3586-3589.
49. W. M. Dose, J. Blauwkamp, P. Senguttuvan, C. S. Johnson “Liquid ammonia chemical lithiation: an approach for high energy and high voltage Si-graphite | Li_{1+x}Ni_{0.5}Mn_{1.5}O₄ Li-ion batteries”, Submitted (2018).